Configuration and validation of an oceanic physical and biogeochemical model to investigate coastal eutrophication in the Southern California Bight

Fayçal Kessouri[1], Karen McLaughlin[1], Martha Sutula [1], Daniele Bianchi[2], Minna Ho[1], James C McWilliams [2], Lionel Renault[2,3], Jeroen Molemaker[2], Curtis Deutsch[4], Anita Leinweber[2]

[1]Southern California Coastal Water Research Project, Costa Mesa, CA [2]Department of Atmospheric and Oceanic Sciences, University of California Los Angeles, CA [3]Laboratoire d'Études en Géophysique et Océanographie Spatiale, Toulouse, France [4]School of Oceanography, University of Washington, WA

Key Points:

- The model reproduces the gradients of physical and biogeochemical properties that can be traced to the influence of coastal inputs.
- The model reproduces nutrient enrichment via subsurface wastewater outfall plumes and riverine runoff.
- The model has been developed to disentangle natural variability, climate change, and local anthropogenic forcing.

Corresponding author: F. Kessouri and K. McLaughlin, `faycalk@sccwrp.org` ; `karenm@sccwrp.org`

Abstract

The Southern California Bight (SCB), an eastern boundary upwelling system, is impacted by global warming, acidification and oxygen loss, and receives anthropogenic nutrients from a coastal population of 20 million people. We describe the configuration, forcing, and validation of a realistic, submesoscale resolving ocean model as a tool to investigate coastal eutrophication. This modeling system represents an important achievement because it strikes a balance of capturing the forcing by U.S. Pacific Coast-wide phenomena, while representing the bathymetric features and submesoscale circulation that affect the transport of nutrients from natural and human sources. Moreover, the model allows to run simulations at timescales that approach the interannual frequencies of ocean variability, making the grand challenge of disentangling natural variability, climate change, and local anthropogenic forcing a tractable task in the near-term. The model simulation is evaluated against a broad suite of observational data throughout the SCB, showing realistic depiction of the mean state and its variability with satellite and *in situ* measurements of state variables and biogeochemical rates. The simulation reproduces the main structure of the seasonal upwelling front, the mean current patterns, the dispersion of wastewater plumes, as well as their seasonal variability. Furthermore, it reproduces the mean distributions of key biogeochemical and ecosystem properties and their variability. Biogeochemical rates reproduced by the model, such as primary production and nitrification, are also consistent with measured rates. Results of this validation exercise demonstrate the utility of fine-scale resolution modeling in support of management decisions on local anthropogenic nutrient discharges to coastal zones.

Plain Language Summary

We applied and validated an ocean numerical model to investigate the effects of land-based and atmospheric nutrient loading on coastal eutrophication and its effects on carbon, nitrogen and oxygen cycles of the Southern California Bight, an upwelling-dominated marine embayment on the U.S. West Coast. The model is capable of high resolution, multi-year hindcast simulations, which enable investigations to disentangle natural variability, climate change, and local human pressures that accelerate land-based and atmospheric nutrient loads. The model performance assessment illustrates that it faithfully reproduces monitored ocean properties related to algal blooms, oxygen and water acidity, among others, that can be traced to land-based and atmospheric inputs of nutrients and carbon from human activities. The model performance assessment helps to constrain uncertainties in predictions to support ongoing conversations on approaches to reduce the effects of climate change, including considerations of management of local nutrient and carbon inputs.

1 Introduction

Human-driven eutrophication has resulted in profound impacts to coastal ecosystems around the world. These impacts are arguably the best studied in estuaries and enclosed bays (e.g. Chesapeake Bay; Cerco and Cole (1993); Boesch et al. (2001)) and semi-enclosed seas such as the Baltic Sea (Savchuk & Wulff, 2007; Cederwall & Elmgren, 1990), the Mediterranean Sea (Arhonditsis et al., 2000), and the Gulf of Mexico (Justić et al., 2005; Laurent et al., 2018). To date, few investigations of coastal eutrophication have occurred in Eastern Boundary Upwelling systems (EBUS). While strong upwelling and vigorous surface currents would generally limit the extent to which coastal eutrophication could occur (Fennel & Testa, 2019), such investigations have also been limited by coupled physical biogeochemical numerical modeling approaches that can adequately resolve fine-resolution bathymetry and the complexities of submesoscale circulation (McWilliams, 2016; Dauhajre et al., 2019), while simulating a sufficient duration (several years) to distinguish oceanic versus terrestrial forcing. These submesoscale circulation features, including fine scale eddies and filaments < 5 km in horizontal resolution, strongly control the magnitude and variability of nearshore

upwelling and associated nutrient transport. Thus, high resolution, submesoscale-resolving numerical models are a necessary prerequisite for mechanistic modeling studies and source attribution of oceanic versus terrestrial drivers of coastal eutrophication in EBUS. Inadequate modeling system and lack of numerical model validation have been identified as significant barriers to effective, evidence-based solutions to coastal eutrophication (Boesch, 2019).

All the necessary ingredients are present to motivate a numerical modeling investigation of the role of coastal eutrophication in driving ocean acidification and oxygen loss in the Southern California Bight (SCB), a large marine open embayment found in the California Current System (CCS) on the U.S. Pacific Coast. First, the SCB is a biologically-productive region, and thus of high economic and ecological importance. Seasonal upwelling of nutrient-rich deep water maintains high rates of biological productivity over broad scales. At the same time, upwelling draws water masses that are naturally low in dissolved oxygen, pH, and carbonate saturation state (Ω_{Ar}) onto the shelf and into the photic zone (Sutton et al., 2017). Second, the SCB has one of the most spatially comprehensive and longest-running coastal observational systems in the world. Several physical and biogeochemical variables are sampled regularly and extensively, creating an ideal setting for model-data comparisons. Third, the SCB is home to one of the most densely populated coastal regions in North America, where the discharges of primary or secondary treated wastewater from a population of 20 million people are released to the coastal zone via ocean outfalls, along with the urban and agricultural runoff from 75 rivers. These nutrient sources rival natural upwelling in magnitude (Howard et al., 2014), roughly doubling available nitrogen to nearshore coastal waters. Intensifying ocean acidification, oxygen loss and harmful algal blooms have motivated California policy makers to consider reducing anthropogenic nutrients as a climate change mitigation strategy (Ocean Protection Council, 2018), but wastewater treatment plant upgrades and methods to increase control or reduce non-point sources would cost billions. A numerical modeling approach is needed to disentangle the effects of natural upwelling and climate change from anthropogenic nutrient loading from land-based and atmospheric sources.

To support such investigations, the regional oceanic model system (ROMS, Shchepetkin and McWilliams (2005)) coupled to the biogeochemical elemental cycling model (BEC, Moore et al. (2004)) has been recently adapted for the CCS (Renault, McWilliams, et al., 2020; Deutsch et al., 2020). A downscaled model domain was established, scaling from a 4 km horizontal resolution configuration spanning the entire CCS, to a 1 km resolution grid covering the much of the California coast (latitude $< 40.25°$N), to a 0.3 km grid in the Southern California Bight (SCB), where investigations of local anthropogenic inputs were focused. Modeling experiments investigating submesoscale transport (captured at model resolutions $\leq$ 1 km) have demonstrated an up to ten-fold increase in the magnitude of instantaneous vertical N fluxes (Kessouri, Bianchi, et al., 2020) relative to mesoscale transport represented by a 4 km model (Section 2.2). Furthermore, a finer horizontal resolution of bathymetry improves the representation of coastal currents, submesoscale circulation, and coast-offshore connectivity (Dauhajre et al., 2019). For this reason, investigations of coastal eutrophication are simulated here at 0.3 km horizontal resolution. Simulations conducted with the 4 km ROMS-BEC model domain have been validated for regional-scale atmospheric forcing, physics, and biogeochemistry, including O_2, carbonate saturation state, primary productivity, and hydrographic parameters, demonstrating that the model captures broad patterns of critical properties in the CCS (Renault, McWilliams, et al., 2020; Deutsch et al., 2020). However, additional focused validation of nearshore, anthropogenically-enhanced gradients in nutrients, primary production, oxygen and pH in model simulations conducted at 0.3 km resolution are needed to gauge model utility to investigate the impacts of coastal eutrophication on ocean acidification and oxygen loss.

We employed this downscaled, submesoscale-resolving physical-biogeochemical model to investigate the effects of land-based and atmospheric nutrient inputs in driving coastal

eutrophication and ocean acidification and oxygen loss. The aim of this manuscript is to: 1) document the SCB ROMS-BEC model configuration, including the effects of land-based and atmospheric inputs of nutrients and organic carbon, intended to support investigations of coastal eutrophication, and 2) present a validation of SCB ROMS-BEC simulations against available observations, focusing on anthropogenically-enhanced gradients in nutrients, primary production, oxygen, and pH.

2 SCB coupled physical and biogeochemical model description, configuration and forcing

2.1 Model description

2.1.1 Ocean hydrodynamics

Ocean hydrodynamics is modeled with the Regional Oceanic Modeling System (ROMS) (Shchepetkin & McWilliams, 2005), a free-surface, terrain-following coordinate model with 3-D curvilinear coordinates that solves the primitive equations with split-explicit time steps. It contains state-of-art numerical algorithms that provide an accurate and stable representation of physical processes down to scales of tens of meters, and allows for offline downscaling of high-resolution sub-domains within larger domains. The offline downscaling is based on the Orlanski scheme for the baroclinic mode (Marchesiello et al., 2001) and a modified Flatcher scheme for the barotropic mode (Mason et al., 2010). Vertical mixing in the boundary layers is represented by a K-profile parameterization (W. G. Large et al., 1994). The U.S. West Coast hindcast model has been successfully run over two decades at 1 and 4 km horizontal resolution using high-resolution spatial and temporal atmospheric forcing that represent the effects of wind drop-off, the current feedback on the surface stress, and high-frequency wind fluctuations (Renault, Hall, & McWilliams, 2016a; Renault, Molemaker, McWilliams, et al., 2016). For this study, we further downscale to 0.3 km resolution to capture submesoscale processes, and run the model for 4 consecutive years between January 1997 and December 2000.

2.1.2 Biogeochemistry

Ocean biogeochemical modeling approaches can have a broad range of complexities, ranging from few functional groups (e.g. NPZD models, Fasham (1993)), to multiple biogeochemical cycles (e.g. C, N, O) and plankton functional groups. To provide a representation of biogeochemical cycles, ROMS is dynamically coupled to the Biogeochenical Elemental Cycling (BEC) model (Moore et al., 2004; Gruber, 2004; Gruber et al., 2011; Deutsch et al., 2020). A schematic of BEC is shown in Fig. 1(b). BEC is a multi-element (C, N, P, O, Fe, Si) and multiplankton model that includes three explicit phytoplankton functional groups (picoplankton, silicifying diatoms, N-fixing diazotrophs), one zooplankton group, and dissolved and sinking organic detritus. The impacts of calcifying phytoplankton (coccolithophores) on the carbon system is represented implicitly. Remineralization of sinking organic material follows the multi-phase mineral ballast parameterization of Armstrong et al. (2001).” and “Sedimentary processes have also been expanded. Particulate organic matter reaching the sediment is accumulated and slowly remineralized with a timescale of 330 days, to provide a buffer between particle deposition and nutrient release. Nitrogen loss to the sediment is parameterized according to the empirical diagenetic model for sediment denitrification of Middelburg et al. (1996). Water column denitrification is only active when oxygen concentrations fall below 5 mmol m^{-3}. Sedimentary release of Fe is based on the benthic chamber measurements of (Severmann et al., 2010) for the California-Oregon coast, and increases as bottom water oxygen concentrations decrease. Atmospheric dust deposition follows the parameterization by Mahowald et al. (2006) and provides an additional source of iron at the surface, although of minor importance compared to sedimentary iron release in the region (Deutsch et al., 2020). The ecosystem is linked to a carbon system module that tracks dissolved inorganic carbon (DIC) and alkalinity, and an air-sea gas exchange

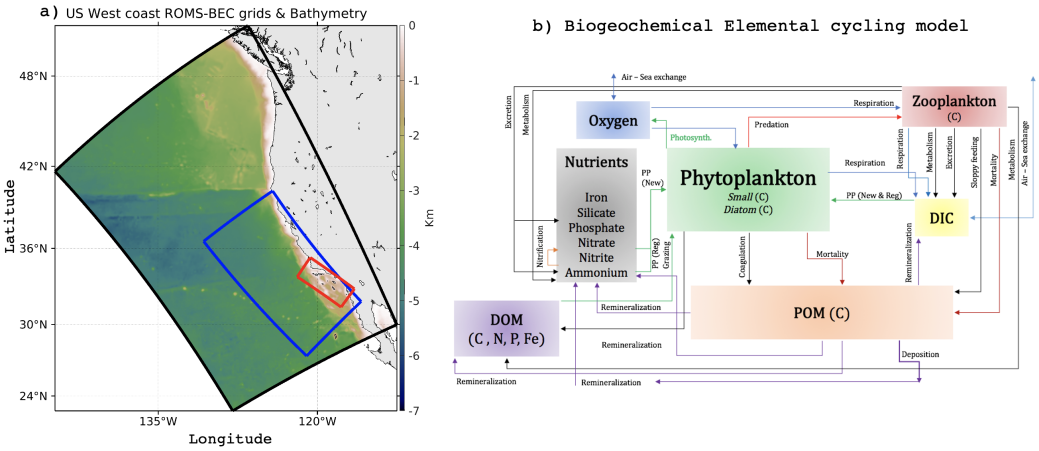

Figure 1: a) ROMS-BEC model configurations. dx = 4 km is the black box, dx = 1 km is the blue box, dx = 0.3 km is the red box. Background color contours show the topography from dx = 4 km. b) Schematic of the biogeochemical elemental cycling model. The schematic shows state variables (boxes) and biogeochemical rates and feedback (arrows).

module that allows realistic representation of dissolved gases (e.g. O_2, CO_2 and nitrous oxide), based on the formulation of Wanninkhof (1992).

2.1.3 Model configuration

The SCB model domain extends along a 450 km stretch of the coast, from Tijuana to Pismo Beach, and about 200 km offshore. This grid, shown in Fig. 1a), is composed of 1400 x 600 grid-points, with a nominal resolution of dx = 0.3 km. The grid has 60 σ-coordinate vertical levels using the stretching function described in Shchepetkin and McWilliams (2009), with the following stretching parameters: $\theta_s = 6$, $\theta_b = 3$, and $h_c = 250$ m. The model is run with a time step of 30 seconds, and output is saved as 1-day averages.

The oceanic forcing of the 0.3 km domain originates from multi-level offline downscaling. A 4 km simulation is initialized and forced at the open boundaries by a preexisting North-east Pacific-wide ROMS solution at 12 km resolution (Renault, McWilliams, et al., 2020), initialized and forced on the boundaries by the global model Mercator Glorys2V3 (http://www.myocean.eu), and is run for the period 1995-2010, after a spin-up of 2 years. A 1 km simulation is initialized and forced from the 4 km model, starting in October 1996 and ending in December 2007. The 0.3 km simulation is initialized and forced at its boundaries by the 1 km simulation starting from January 1997 and ending in December 2000. The bathymetry used in this configuration comes from the Southern California Coastal Oceanic Observation System (SCCOOS) 3 Arc-Second Coastal Relief Model Development (90 m horizontal resolution).

The oceanic model is forced by hourly outputs from the atmospheric uncoupled Weather Research and Forecast model (WRF06; Skamarock and Klemp (2008)). Using bulk formulae (W. B. Large, 2006), WRF06 provides heat, surface evaporation, momentum and atmospheric data and is run at 6 km resolution over a domain similar to the 4 km (Fig. 1 and used for Renault, Hall, and McWilliams (2016b)), and includes a wind-current coupling parameterization necessary to attain more realistic simulations of the oceanic eddy kinetic energy (EKE) and circulation (Renault, Molemaker, McWilliams, et al., 2016; Renault, Masson, et al., 2020).

Model simulations were conducted from 1997-2000, a period chosen to capture the effects of all three phases of the El Niño–Southern Oscillation (ENSO); it also captures the beginning of the "modern" state of point source management in the SCB, where several large Publicly Owned Treatment Plants (POTW) were in transition from primary to secondary treatment. (We will refer to submarine point sources outfalls from the treatment plants as "POTW" hereafter.)

2.2 Importance of submesoscale circulation

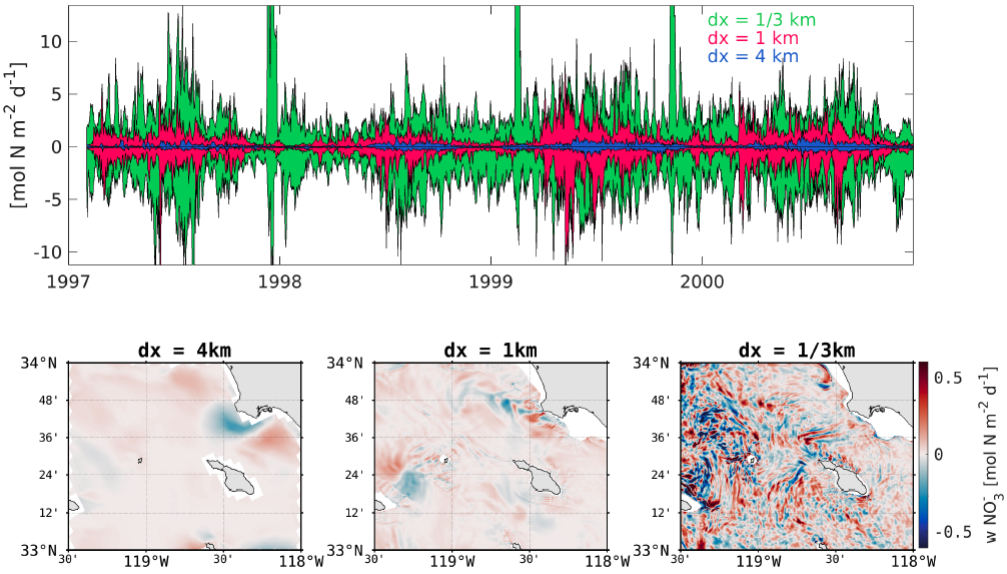

Figure 2: (Upper panel) Timeseries (1997-2001) of the vertical eddy flux of nitrate at 40 m depth calculated as follow: $\overline{wN} = \overline{w}\,\overline{N} + \overline{w'N'}$, where the overbar represents a monthly average, and the prime the deviation from this average, for region covering the entire Southern California Bight. The minimum and maximum values (i.e. the envelope) of the flux are shown in blue for the 4 km solution, in red for the 1 km solution and in green for the 1/3 km. (Lower panel) Snapshot of the vertical flux of nitrate in spring at 40 m off the coast of Palos Verdes that shows higher magnitudes and enhanced variability as resolution increases.

Downscaling to dx = 0.3 km allows the model to represent ocean circulation that includes baroclinic and barotrophic eddies and turbulence generated at the submesoscale (Capet, Campos, & Paiva, 2008). Resolving submesoscale eddies dramatically increases the variability of vertical fluxes of biogeochemical tracers and other material properties, eventually allowing a more accurate representation of chemical and biological constituents. Figure 2(upper panel) shows the temporal variability and horizontal distribution of vertical eddy fluxes of nitrate at 40 m from 3 different resolutions with the ROMS model (see section 2.1.3). Submesoscale dynamics increase instantaneous fluxes by more than one order of magnitude, with more frequent and vigorous fine-scale structures (Fig. 2(bottom panels)) when increasing the resolution from 4 km to 1 km, and similarly another order of magnitude when increasing resolution from 1 km to 0.3 km. Intensification of vertical flux of nitrate at the euphotic depth has previously been shown in idealized models (Mahadevan, 2016; Lévy et al., 2012) and in realistic simulations in the central California upwelling system (Kessouri, Bianchi, et al., 2020), but has never been modeled in the SCB at this resolution. Submesoscale eddies have been associated with increased productivity in the

oligotrophic ocean (Mahadevan, 2016) and decreased productivity in the upwelling region (Kessouri, Bianchi, et al., 2020). Our submesoscale-resolving simulation at dx = 0.3 km is an opportunity to quantify the balances of nitrogen, dissolved oxygen, carbon and productivity using a more realistic representation of the physical circulation, as well as a representation of urban anthropogenic inputs to the ocean.

Inclusion of submesoscale dynamics energizes frontogenesis by mesoscale straining and mixed layer instabilities (Capet, Klein, et al., 2008; Capet, Campos, & Paiva, 2008; Capet, McWilliams, et al., 2008). Oceanic fronts are a driver of significant nutrient supply to the upper ocean. They have also been recognised as areas of enhanced biomass in many regions of the global ocean (Woodson & Litvin, 2015), as well as important locations for fisheries (e.g. (Galarza et al., 2009)). In our set of simulations, we show that the increased number of fronts and submesoscale instabilities promote intense variability of nitrate transport as shown in figure 2, as well as increased heterogeneity at the subsurface chlorophyll *a* maximum. However, surface phytoplankton biomass is only intensified if the timescale of the enrichment is sufficiently long and maintained in these small scale features. Modeling at this scale allows for a more accurate simulation of biogeochemical tracers and rates, as described in subsequent sections.

2.3 Terrestrial and atmospheric forcing of freshwater, nutrients and carbon

Model simulations were forced with a monthly time series of spatially-explicit inputs (Fig. 3, upper), including freshwater flow, nitrogen, phosphorus, silica, iron, and organic carbon representing natural and anthropogenic sources (Sutula et al., 2021b). These data include POTW ocean outfalls and riverine discharges (1997-2017) and spatially-explicit modeled estimates of atmospheric deposition. POTW effluent data were compiled from permit monitoring databases and communication with sanitary agencies. Monthly time series of surface water runoff from 75 rivers are derived from model simulations and monitoring data (Sutula et al., 2021b). Direct atmospheric deposition is derived from the Community Multi-scale Air Quality (CMAQ) model (Byun et al., 2006), and follows the implementation of Deutsch et al. (2020). In this paper, we discuss in detail the formulation of the river and wastewater outfall inputs.

2.4 Configuration of river and wastewater outfall forcing in the model

Ocean outfalls and coastal rivers are modeled as mass sources into the ocean (Fig. 3, upper). To accomplish this, we add explicit volume fluxes to the otherwise divergence-free flow in the ocean. The inclusion of these fluxes makes it possible to account for associated sources of tracers, while satisfying conservation laws. Specifically, our approach allows for the proper influx of fresh water in the ocean, without resorting to a 'virtual salt' flux, which is a common approach in larger scale ocean models (Kang et al., 2017). Since we explicitly include known volume fluxes for both rivers and outfall pipes, specification of tracer concentration is sufficient to correctly model the source terms. The tracer evolution equations that are used in ROMS are implemented by using control volumes (Shchepetkin & McWilliams, 2005) where for each tracer concentration $C = C(x, y, z, t)$,

$$\frac{\partial \iiint C \, dV}{\partial \mathrm{t}} = \iint u_n C \, dA. \tag{1}$$

where $V = V(x, y, z, t)$ is the volume of the entire domain, u_n is the normal velocity into the volume and $A = A(x, y)$ is the total area of grid cells source is being input. Additionally, we enforce mass conservation which implies;

$$\frac{\partial \mathrm{V}}{\partial \mathrm{t}} = \iint u_n \, dA. \tag{2}$$

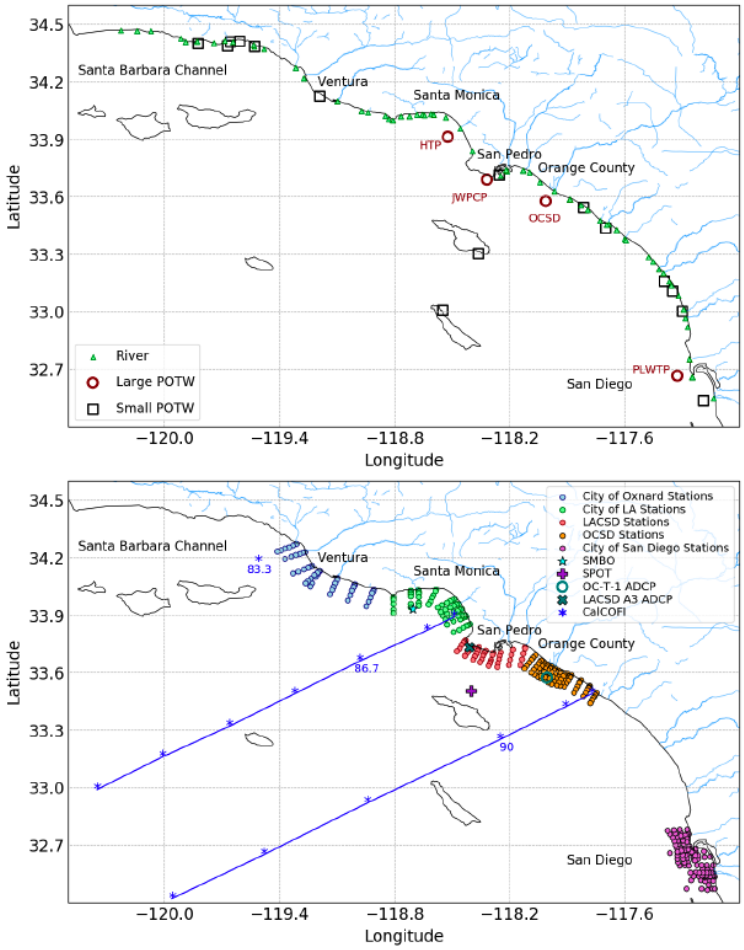

Figure 3: (Upper panel) Location of rivers and POTW outfalls along the SCB. (Lower panel) Location of monitoring stations used for the validation, including POTW quarterly monitoring surveys, CalCOFI seasonal observations, showing the line numbers, Santa Monica Bay Observatory (SMBO), and San Pedro Oceanographic Timeseries (SPOT), mooring.

In absence of rivers and outfalls, the flow is volume conservative, and the integral on the right hand side of Equation 2 is zero. Using Equations 1 and 2, it is easy to see that the mean concentration of a tracer can be lowered if the average concentration of the flux entering the control volume is less than the mean concentration in that volume. In this manner, fresh water rivers will lower the salinity of the water in which they enter. All 75 rivers and 23 POTW pipes that are considered in this study are implemented in this manner.

Each individual source is based on the following equation:

$$S(x, y, z, t) = \frac{W(x, y, z)\, Q_s(t)\, C_s(t)}{V_s} \tag{3}$$

With:
$S(x, y, z, t)$: volume source of contaminant (mmol m^{-3} s^{-1}).
$W(x, y, z)$: non-dimensional shape function (with values between 0 and 1).
$Q_s(t)$: water volume flux from the source (m^3 s^{-1}).
$C_s(t)$: concentration of the tracer C in the source water (mmol m^{-3}).
V_s: effective volume of the source (m^3).

For each source, $Q_s(t)$ and $C_s(t)$ are prescribed as time series. The shape function $W(x, y, z)$ distributes the tracer spatially and in the water column, representing non-resolved mixing and dilution effects. Its values represent the relative intensity of the *in situ* tracer injection, with values between 0 and 1. Tracer concentration C is distributed in the water column as $C(x, y, z, t) = W(x, y, z)C_s(t)$ The effective 3D volume of the source is calculated from the shape function $W(x, y, z)$ as:

$$V_s = \iiint W(x, y, z)\, dV \tag{4}$$

where the integral is over the model domain. For convenience, we assume that $W(x, y, z)$ can be separated into a horizontal shape function $A(x, y)$, multiplied by a vertical shape function $H(z)$ (both non-dimensional and with values between 0 and 1), such that:

$$V_s = \iint A(x, y)\, dx\, dy \int H(z) dz = A_s\, H_s \tag{5}$$

Here, A_s represents the effective source surface area (m^2), and H_s the effective source thickness (m). The functions $A(x, y)$ and $H(z)$ are defined differently for POTW and rivers. They are assumed to be fixed in time; a time-dependent generalization (for example to mimic variations in the depth of the POTW buoyant plume) is straightforward. For POTW inputs, at each main diffuser, the horizontal distribution $A(x, y)$ of the source is shown in Fig. S1. This method of weighting the plume in different cells allows the effluent to be properly diluted vertically and horizontally at this resolution and prevents the model from developing numerical instabilities.

Each large treatment plant has specialized outfall configurations that are taken into account for representation in the model (Fig. S1). The flow is divided in two at Hyperion Treatment Plant (HTP) located 6km off Marina Del Rey (Santa Monica Bay) (Fig. S1A) and Point Loma Wastewater Treatment Plant (PLWTP) in San Diego coast (Fig. S1D) to account for their Y-shaped diffuser, partitioning 50% of the flow to each diffuser. Orange County Sanitation District (OCSD) located 6km off Huntington Beach (Fig. S1C) has one flow through its L-shaped diffuser. Joint Water Pollution Control Plant (JWPCP) in Palos Verdes shelf (Los Angeles) (Fig. S1B) has three diffusers, the Y-shape northern typically discharges 17.5% of the flow for each leg of the Y-diffuser, and the southern L-shape diffuser discharges 65% of the flow. The vertical profile of the POTW sources is defined by a Gaussian function centered at a height z above the bottom (h_b), to mimic a buoyant plume, so that $H(z)$ is given by:

$$H(z) = e^{-z^2/d_s^2} \tag{6}$$

Where $z = -h_b + h_s$, with
h_b: bottom depth (m).
h_s: depth of the buoyant plume above the bottom (m).
d_s: vertical scale of the POTW plume (m).
We further assume $h_s = 20$ m and $d_s = 10$ m, as in Uchiyama et al. (2014).

We distribute the SCB rivers on one horizontal grid point (0.3 km wide), where we assume $A(x, y) = 1$, and similarly distribute the source vertically, with the Gaussian function centered at the surface. h_s here is simply the water column depth to put the maximum input at the surface. Because in ROMS the thickness of vertical grid cells varies in time, to ensure tracer conservation the calculation of the input source volume V_s must be done at each time step, even in the case of a time-independent source shape function $W(x, y, z)$. Effectively, only $H_s = H(z)$ needs to be recalculated at each time step.

3 Model performance assessment approach

The conceptual approach for model performance assessment is comprised of three components, addressing different aspects of skill assessment: 1) statistical comparison of model output to observational data for state variables by region and season; 2) comparison of model output to observational data for biogeochemical rates; 3) evaluation of model behavior compared to expected biogeochemical dynamics for coastal zones. Comparison of model output to observational data by region and season is designed to document model skill at reproducing the statistics (e.g., mean values and variability) of ocean physical and biogeochemical parameters at the spatio-temporal scales more relevant for evaluating human impacts on the coastal environment. Comparison of model output to observational data for biogeochemical rates assures that model is capturing the appropriate transformations in nutrients and carbon that structure the ecosystem response to eutrophication. Finally, the evaluation of model behavior compared to the expected physical and biogeochemical dynamics for coastal zones is a more qualitative evaluation of model performance to document that the model broadly reproduces oceanographic phenomena in a way that reflects our understanding of nearshore ocean environments.

3.1 Description of Observational Datasets

3.1.1 Ship-Based Ocean Monitoring

The SCB is home to a suite of long-running monitoring programs that make it one of the best observed coastal ecosystems in the world (3, lower). Among them, the California Cooperative Oceanic Fisheries Investigations (CalCOFI) program (McClatchie, 2016), initiated in the 1950s, samples the SCB quarterly each year, collecting hydrographic and biogeochemical measurements in coordination with the Southern California Coastal Ocean Observing System (SCCOOS). These observations are augmented nearshore by quarterly surveys of nearshore water column and benthic parameters conducted collaboratively since 1990 by POTW agencies as a part of their regulatory monitoring requirements (Howard et al., 2014; McLaughlin et al., 2018; Booth et al., 2014; Nezlin et al., 2018). These programs provide good temporal and geographical coverage of both the offshore (CalCOFI) and nearshore (POTW) areas, coinciding with the model period, and include publicly available water quality data for targeted sites measured quarterly. We validated model output against observed temperature, dissolved oxygen, nitrate, ammonium, chlorophyll, carbon-system parameters (pH and aragonite saturation state), primary production, and nitrification.

In situ measurements have inherent uncertainty, due to a combination of measurement sensitivity and sampling frequency and intensity, making them an imperfect "truth" with which to compare to model output. However, this uncertainty is not the same for all parameters. Both temperature and dissolved oxygen are collected using high resolution probes, though the two programs used in this study incorporate slightly different calibration pro-

tocols for dissolved oxygen, lending greater confidence to data-model comparisons for these datasets. Chlorophyll is measured on discrete bottle samples in the CalCOFI program, a high quality measurement, but inferred from *in situ* fluorescence measurements in the POTW monitoring program, adding uncertainty to these measurements. Nitrate and ammonium concentrations are measured on discrete bottle samples for both programs, but the detection limits are more sensitive in the CalCOFI program. Furthermore, nutrients are not measured with the same sampling density in POTW monitoring programs as sensor data. Similarly, primary production is measured at a subset of locations in the CalCOFI program and as a short-term special study in Southern California Bight Regional Marine Monitoring Program (Bight Program). Details on measurements and sample collection protocols for the CalCOFI program can be found on their website (https://calcofi.org ; McClatchie (2016)) and for the POTW monitoring programs in Howard et al. (2014). We also use selected nutrient observations from the Santa Monica Bay Observatory (SMBO) mooring located in the Santa Monica Bay (Leinweber et al., 2009). Figure 3 shows a map of all monitoring stations used in this study. The repository of data can be found in Kessouri, McLaughlin, et al. (2020).

3.1.2 High Frequency Radar and Acoustic Doppler Current Profilers

High Frequency Radar (HF) data from the database of the University of California, San Diego (https://hfrnet-tds.ucsd.edu/thredds/catalog.html) provide surface currents along the west coast of the United States, including the SCB. Seasonally averaged data from 2012-2020 were used to analyze trends of surface currents in the Bight compared to the model. Acoustic Doppler Current Profilers (ADCP) provide current data in the water column. ADCP measurement data from Orange County Sanitation District (OCSD) for the period June 1999 to June 2000 and Los Angeles County Sanitation District (LACSD) during November 2000 to June 2007 were used to validate vertical profiles of currents.

3.1.3 Remote sensing observations

Satellite ocean color measurements for chlorophyll were used to characterize horizontal gradients at finer scales and higher density than possible with the ship-based monitoring. We use monthly averaged surface chlorophyll concentration from the period 1997 to 2000 derived from the SeaWiFS sensor at 4 km spatial resolution. Large gaps in the dataset can occur because of dense cloud cover that occurs in late spring and early summer. The products of the Vertically Generalized Production Model (VGPM) net primary production algorithm (Behrenfeld & Falkowski, 1997) were also considered for this validation. Despite limitations, satellite data provide a valuable representation of the spatial distribution of chlorophyll, temperature, and primary production at seasonal scales over the region.

3.2 Performance Statistics

Our approach to a statistical assessment of agreement between model predictions versus observations reflect the fact that the hydrodynamic model, under the influence of realistic forcings (e.g. wind fields) and without data assimilation, develops its own intrinsic variability in circulation, e.g. submesoscale eddies (McWilliams, 2007). The resulting modeled state variables would not necessarily overlap with observations on a point-by-point basis, but would be comparable to observations when averaged over appropriate spatio-temporal scales. We assessed a suite of statistics and metrics, following the methodology of Allen et al. (2007), to assess how well the model reproduces the magnitude and gradients of selected state variables, whether the model agreement has an apparent bias, and how well the model reproduces natural variability. We calculated six metrics, defined in the following, where N is the total number of appropriate observational data, D represents each individual observational datum, $\overline{D}$ is the mean of the observational data, M is the model estimate representing an observation, and $\overline{M}$ is the mean of the model estimate. The metrics considered include:

The Pearson correlation coefficient, reflecting the degree of linear correlation between the observed and model variable, and the statistical significance (p-value) of this correlation:

$$r_{xy} = \frac{\sum_{n=1}^{N}(D_n - \overline{D})(M_n - \overline{M})}{\sqrt{\sum_{n=1}^{N}(D_n - \overline{D})^2}\sqrt{\sum_{n=1}^{N}(M_n - \overline{M})^2}}; \tag{7}$$

The Cost Function (CF), which gives a non-dimensional value indicative of the "goodness of fit" between two sets of data, quantifying the difference between model results and measurement data:

$$\mathrm{CF} = \frac{1}{N}\sum_{n=1}^{N}\frac{|D_n - M_n|}{\sigma_D} \tag{8}$$

where σ_D is the standard deviation of the observations;

The Percentage Bias (PB) (the sum of model error normalized by the data):

$$\mathrm{PB} = \frac{\sum(D - M)}{\sum D} * 100; \tag{9}$$

The Ratio of the Standard Deviations (RSD):

$$\mathrm{RSD} = \frac{\sigma_D}{\sigma_M} \tag{10}$$

where σ_M is the standard deviation of model outputs;

The Nash-Sutcliffe Model Efficiency (ME) (Nash & Sutcliffe, 1970), a measure of the ratio of the model error to the variability of the data:

$$\mathrm{ME} = 1 - \frac{\sum(D_n - M_n)^2}{\sum(D - \overline{D})}; \tag{11}$$

And the two-sample t-test, or Welch's t-test (Welch, 1947; Derrick et al., 2016):

$$H = (\overline{D} - \overline{M})/\sqrt{\frac{\sigma_D^2}{N} + \frac{\sigma_M^2}{N}}. \tag{12}$$

We score the model performance following Table 1 per the methodology of Allen et al. (2007).

Statistic	Excellent	Good	Reasonable	Poor
Cost Function (Moll & Radach, 2003)	<1	1-2	2-3	>3
Nash Sutcliff Model Efficiency (Nash & Sutcliffe, 1970)	>0.65	0.65-0.5	0.5-0.2	<0.2
Percentage Bias (Maréchal, 2004)	<|0.1|	|0.1-0.2|	|0.2-0.4|	>|0.4|
H (Welch, 1947)	0			1
Correlation Coefficient	1-0.9	0.9-0.8	0.8-0.6	<0.6
p-value	<0.05			>0.05
Ratio of Standard Deviations	1-0.9, 1-1.1	0.9-0.8, 1.1-1.2	0.8-0.6, 1.2-1.4	<0.6, >1.4

Table 1: Model performance

4 Model performance assessment findings

4.1 Ocean circulation

The SCB is situated at the confluence of water masses from the subarctic Pacific via the California Current, and from the eastern tropical North Pacific via the California Undercurrent, which all interact with the local topography, the coast, and the atmosphere to sustain variability in circulation on inter-annual, seasonal, and intraseasonal time scales (Dong et al., 2009; Bograd et al., 2015). The effects of this variability in circulation has profound consequences for coastal ocean biogeochemistry (Gruber et al., 2011; Bograd et al., 2015; Nagai et al., 2015; Nezlin et al., 2018), and is therefore critical that the model accurately simulates spatial and temporal variability in circulation patterns.

Figure 4 shows the hydrodynamic characteristics of the SCB in the model compared to data. In the northern SCB, the model shows similar qualitative and quantitative patterns for the horizontal circulation compared to HF data (Fig. 4(a)-(b)) and as seen in Dong et al. (2009). The circulation in the SCB is characterized by northward currents in the first 20 km of the coast and cyclonic circulation in the middle of the SCB that is stronger in summer and weaker in winter. The model successfully reproduces observed current patterns, with similar current magnitudes. The intensity of the northward coastal branch of the current is on average about 0.15-0.3 m s^{-1} in summer versus 0.05-0.15 m s^{-1} in winter. The offshore southward branch is generally about 0.3 m s^{-1} all year round (Fig. 4(a)-(b)). The dominant current in the coastal band (15 km from coast) of the SCB flows northward, and follows the topography along isobaths on the shelf (Fig. 4(g)-(h)).

The simulated June 1999-June 2000 variability of the current in depth is shown in the vertical profiles extracted off the coast of Palos Verdes and Orange county compared to the ADCP data at the same locations (Fig. 4(c)-(f)). The location of both of these profiles are a few kilometers from the contintental slope and therefore capture a suite of physical processes, including mesoscale and submesoscale eddies, fronts, jets, and internal tides (Capet, McWilliams, et al., 2008; Kim et al., 2011; Dong et al., 2009). The model generally reproduces the means and range of the variability shown in these close to shore horizontal currents, which demonstrates that ROMS at dx = 0.3 km resolution captures the submesoscale variability described in Section 2.2.

In the northern SCB, cyclonic vortices are generated inside the Santa Barbara Channel (Fig. 4(i)) when the northward current that flows along the Ventura coast meets the eastern side of the Channel Islands, with higher intensity in summer (Fig. 4(a) versus (b)) (Winant et al., 2003). Submesoscale eddies are particularly prominent in this region, in particular persistent cyclonic eddies that drive an upward doming of isopycnals (Fig. 4(j)) (McGillicuddy Jr, 2016), which supplies nutrients to the euphotic layer. The model correctly reproduces this vertical transport, described in Brzezinski and Washburn (2011), and the high concentrations of nitrate and other nutrients in the upper layers of the Santa Barbara Channel, as further detailed in Section 4.3.1.

In the central and southern SCB (latitude $< 34.7°$N), the model successfully captures flow regimes around the large POTW outfalls, indicating that it can appropriately represent the dispersal of wastewater plumes in these regions. In the Santa Monica and San Pedro Bays, topography drives the circulation of currents inside the Bays, converging back to the main current offshore (Fig. 4(g)-(h)). On top of the Hyperion and JWPCP outfalls (in the Santa Monica Bay and offshore of the Palos Verdes peninsula, respectively), the current is mostly south-eastward. Near the OCSD outfall, the current direction varies in winter between south-eastward and north-westward, but is primarily southward in summer (Fig. 4(a)-(b), (e)-(f)). At the PLWTP outfall, the current is narrow, with a dominant south-eastern direction, parallel to the coast, demonstrated by both model and HF radar data.

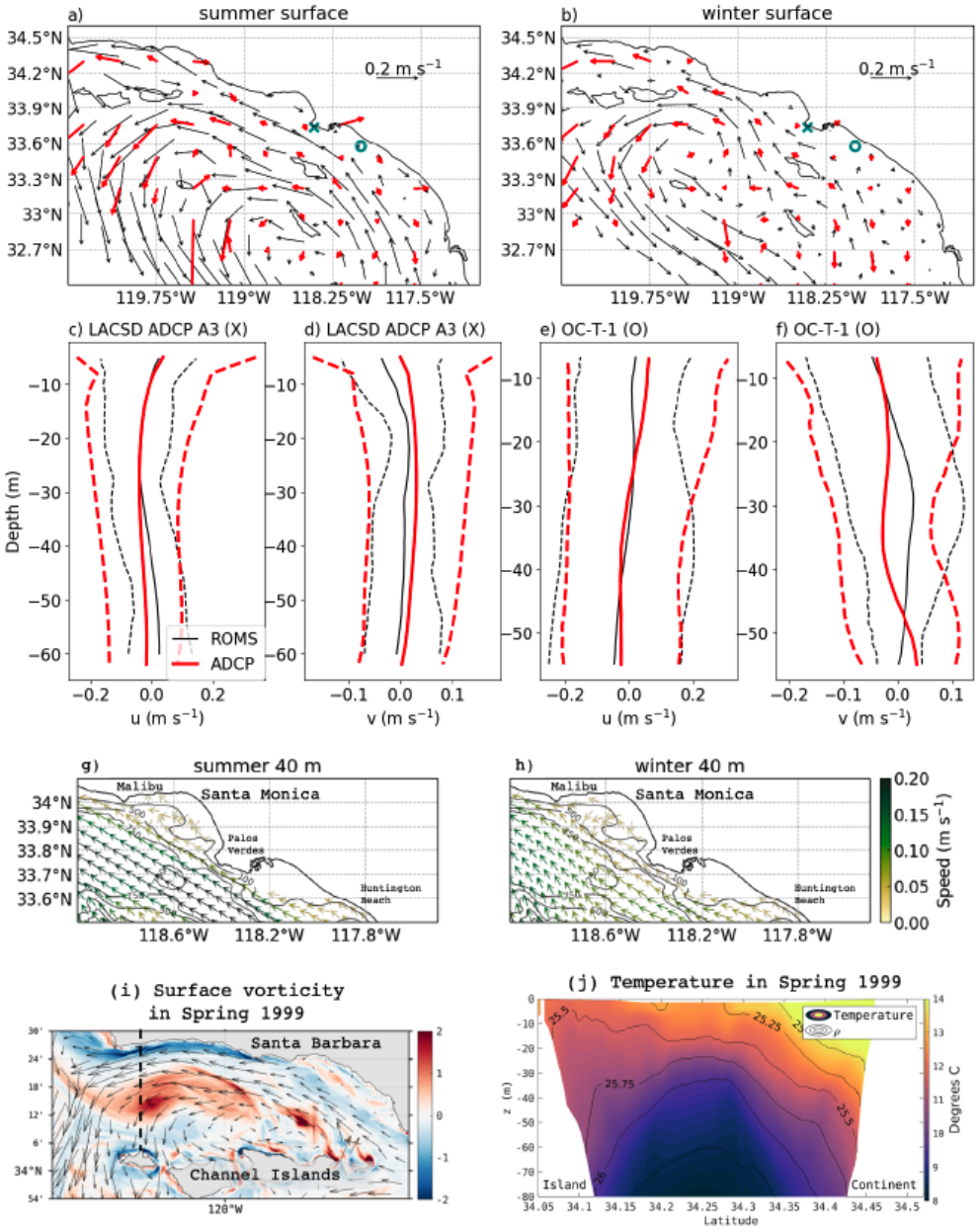

Figure 4: a) Mean surface currents in the Southern California Bight from HF data during 2012-2020 (thick red arrows) and model during 1999-2000 (black arrows) in summer and b) winter. c)-f) Vertical profiles of horizontal velocity components from ADCP instruments (thick red lines) and model (thinner black lines). The two dashed lines indicate the 5th and 95th percentile current values. c)-d) ADCP data come from the LACSD mooring A3 stationed at the teal 'X' in a)-b) and e)-f) come from the OCSD mooring OC-T-1 located at the teal 'O'. g) Mean model current direction and speed (colored) at 40 m depth with bathymetry contoured in summer and h) winter. i) Surface model vorticity normalized by f in spring in Santa Barbara Channel showing cyclonic eddies. j) Cross-section of temperature and density isopycnals as drawn by the dashed line in (i) from model to show eddy-driven uplifting of the isopycnals in the center of Santa Barbara Channel.

4.2 Vertical gradients and seasonal variability of temperature and mixed layer depth

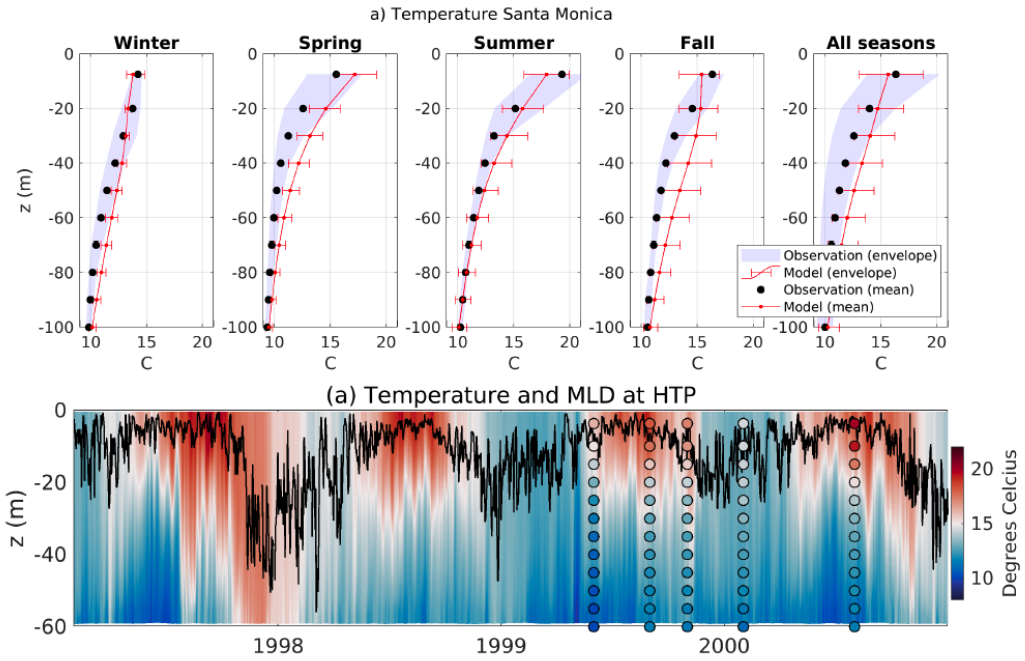

Figure 5: (a) Average seasonal profiles of temperature in the Santa Monica Bay. The red lines and red bars show the spatio-temporal mean and the variability from the model respectively. The black dots and the gray shading show the spatio-temporal mean and the variability from *in situ* data (City of LA stations), respectively. (b) Hovmöller diagram of temperature at the location of the Hyperion POTW outfall (HTP) in the Santa Monica Bay issued from the model. The black line shows the simulated time-series of mixed layer depth. The deepest mixing occurs during El Niño 1998 (>40 m). Colored dots are average concentrations from *in situ* measurements.

The model successfully reproduces the three-dimensional and seasonal variability of physical tracers, here exemplified by temperature. Temperature is the parameter in which we have the highest confidence in the observational record, because observations are abundant, and sensors are accurate and precise, regularly calibrated, and with negligible drifts. The greatest source of observational uncertainty is temporal under-sampling, but some sources of model bias may also be important (e.g., from atmospheric forcing, wind, or shortwave detailed in Renault, McWilliams, et al. (2020)). Quantitative statistical analysis indicates that model performance is '*excellent*' or '*good*' for nearly all metrics for all regions and seasons (see Table 2). The lowest performance of the model is characterized as '*reasonable*' for certain sub-regions (Palos Verdes, Orange County, and San Diego) in spring and fall (Palos Verdes only) (see Supporting Information Table S2). As noted above, this may be due to under-sampling during these months, which can be highly variable because the region is shifting between a well-mixed to a more stratified ocean regime. Detailed information on the other sub-regions and their statistical comparison can be found in the Supporting Information, Tables S1 to S4.

Following common practices (de Boyer Montégut et al., 2004), we define the mixed layer depth (MLD) as the depth at which temperature decreases from its surface value by more than 0.2°C. On average, the MLD deepens from the coast to offshore, and varies with season

(e.g. in Santa Monica Bay in Fig. 5b). The model successfully simulates the seasonal cycle of MLD along the coast. For example, the model recreates the observed seasonal deepening of the mixed layer in the Santa Monica Bay to depths greater than 16-20 m (the typical depth of the upper signature of the POTW plumes, see Section 4.3.2) nearly every winter (black line in the Fig. 5b).

Regular winter shows a homogeneous upper layer of $< 14°C$ temperature, and a mixed layer located at 18-20 m in the coastal region and 40-60 m offshore. The surface ocean is colder around the Channel Islands (SST$<$12°C) (see Fig. 19). In the open ocean, the model reproduces the de-stratification with deepening of the thermocline to about 70m and a MLD at about 40m (Fig. 6c and d). In summer, stratification is the strongest, reflecting an intense vertical temperature gradient, and the MLD (both in the model and in the observations) is found few meters below the surface (approximately 10 m). Temperature varies rapidly from more than 20°C at the surface in the southern domain (16-17°C in the northern domain) to less than 12°C at 50m depth over the entire SCB (see also Fig. 19). In the open ocean, the model succeeds in reproducing the stratification that brings the seasonal thermocline to 50m and the MLD to 15m (Fig. 6c) and e)).

The model reproduces interannual variability in MLD under the influence of El Niño-Southern Oscillation (ENSO, hereafter referred to as El Niño, i.e., the period from fall 1997 to spring 1998 in Fig. 5b), when the MLD reached 40 m. We show that during winter of El Niño year, the entire water column of the SCB is warmer than on average, and surface temperature is more homogeneous, varying between 15.5 and 17°C (Fig. 6a). In the open ocean, during El Niño, with warmer upper layer than regular winters, the model shows good performance in reproducing the deepening of the seasonal thermocline (>120 m) and of the MLD (>50 m) (e.g. offshore Santa Monica Bay in Fig. 6a and b). These patterns of variability in temperature are consistent with regional observations of El Niño in the SCB (Todd et al., 2011).

4.3 Dissolved Inorganic Nitrogen

4.3.1 Spatial patterns and seasonality of nitrate

Nitrate observations are only broadly available in the offshore CalCOFI dataset, so only large-scale regional patterns in nitrate concentration can be validated. There is a clear seasonality of nitrate, where surface concentrations are higher in spring and summer, and decrease in fall and winter (Fig. 7). The model reproduces the average seasonal patterns observed in the *in situ* nitrate data across multiple regions. The model also captures alongshore variability in coastal nitrate concentrations, reproducing values greater than 25 mmol N m^{-3} off Santa Barbara, 20 mmol N m^{-3} off Los Angeles, and 15 mmol N m^{-3} off San Diego.

The model also reproduces observed patterns in the depth of the nitracline (Mantyla et al., 2008; Nezlin et al., 2018), which tends to follow sloping density surfaces in the region. These patterns include: the high values at the euphotic depth limit (∼50m below the surface) along the Santa Barbara coast in spring; the doming of the nitracline in the center of the Santa Barbara Channel (Fig. 7b); the 20 to 30 m deep nitracline along the Los Angeles coast; and the deepening of the nitracline from about 30 m at the coast to more than 60 m offshore in San Diego. In the offshore region of the SCB, the model is consistent with observations showing high nitrate (>20 mmol N m^{-3}) around the Channel Islands (not shown) as compared to less than 5 mmol N m^{-3} farther offshore. This pattern is strongest in winter and summer, when the offshore regions are particularly oligotrophic (surface $NO_3^- < 1$ mmol m^{-3}) throughout the SCB.

Santa Monica: Temperature								
	H	Correlation Coefficient	p-value	Cost Function	Percentage Bias	Ratio of Standard Deviations	Nash-Sutcliffe Model Efficiency	Number of observations
Winter	0 E	0.96 E	7E-06 E	0.05 E	-0.04 E	1.10 G	0.81 E	716
Spring	0 E	0.98 E	8E-07 E	0.10 E	-0.10 G	0.78 R	0.51 G	716
Summer	0 E	0.97 E	9E-06 E	0.04 E	-0.02 E	1.07 E	0.93 E	712
Fall	0 E	0.89 G	3E-06 E	0.09 E	-0.08 E	0.98 E	0.51 G	718
All Seasons	0 E	0.95 E	3E-05 E	0.08 E	-0.07 E	1.02 E	0.73 E	2862

Table 2: Statistical comparison between *in situ* data and model outputs for temperature profile in Santa Monica Bay (City of LA stations). Letters next to numbers indicate model performance: E = Excellent, G = good, R = reasonable, P = Poor.

Santa Monica: Ammonium								
	H	Correlation Coefficient	p-value	Cost Function	Percentage Bias	Ratio of Standard Deviations	Nash-Sutcliffe Model Efficiency	Number of observations
Winter	0 E	0.94 E	0.06 P	0.54 E	0.24 R	1.86 P	0.68 E	20
Spring	0 E	0.85 G	0.14 P	0.58 E	-0.57 P	0.69 R	-0.61 P	21
Summer	0 E	0.58 P	0.42 P	0.72 E	0.19 G	1.76 P	0.29 R	21
Fall	0 E	0.91 E	0.09 P	0.42 E	0.07 E	1.47 P	0.80 E	21
All Seasons	0 E	0.81 G	0.10 P	0.36 E	-0.03 E	1.23 R	0.60 G	83

Table 3: Statistical comparison between *in situ* data and model outputs for ammonium profile in Santa Monica Bay.

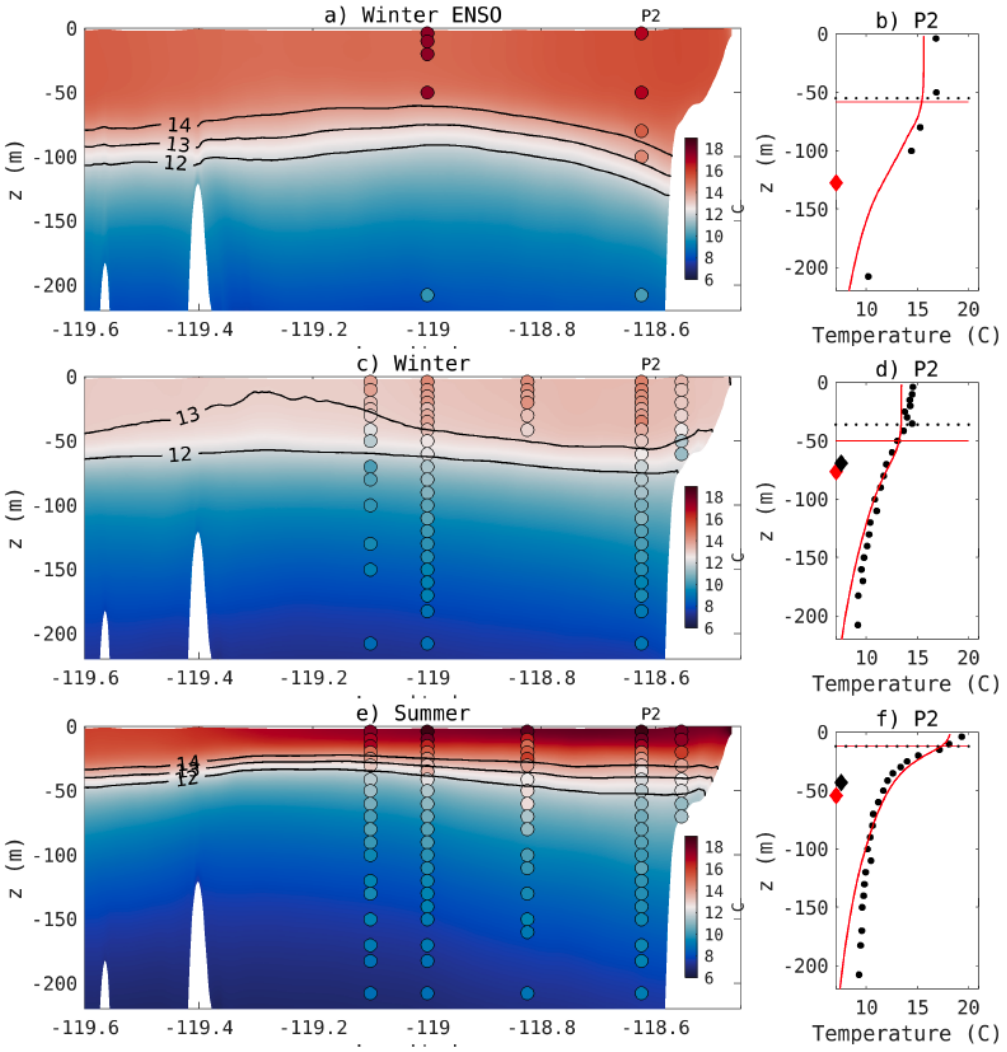

Figure 6: (a) Cross section of average temperature following line 86.7 from CalCOFI monitoring stations during an El Niño winter (12/1997 to February 1998). (b) Profile at station P2. Black dots are CalCOFI *in situ* data, red line is the simulated profile. The horizontal line is the MLD (black is CalCOFI, red is simulated). Diamonds (black is CalCOFI, red is simulated) is the depth of the maximum gradient to estimate the depth of the seasonal thermocline at 12°C. (c-d) are similar to (a-b) for average winter, and (e-f) are for average summer.

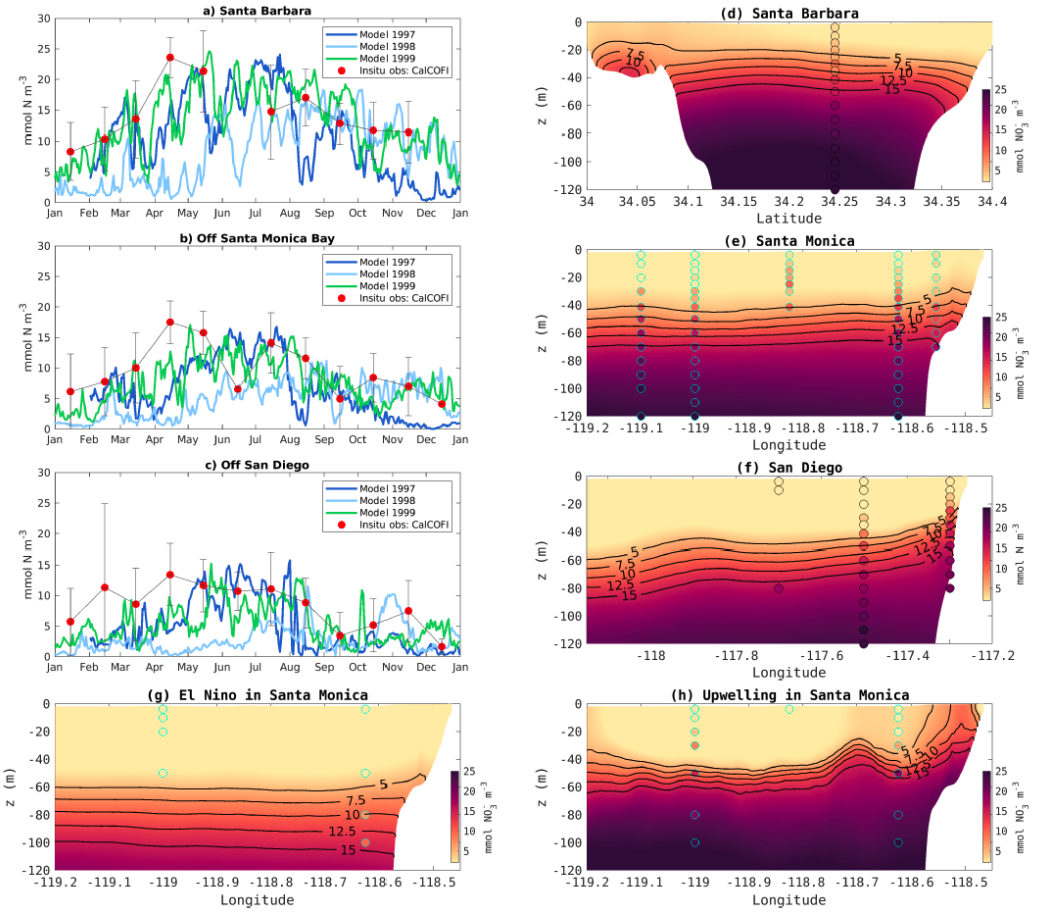

Figure 7: (a-c) Time series of nitrate concentration at 50 m depth in three different locations of the SCB: (a) is near the center of Santa Barbara Channel, (b) is offshore the Santa Monica Bay, and (c) is offshore San Diego. Model outputs are represented by the lines for three different years, with the dots showing mean values from *in situ* measurement from CalCOFI, and gray bars the standard deviation from the mean. The time-series show prominent interannual variability in addition to seasonal variability. While the years 1997 and 1999 show similar nitrate distributions, the El Niño period between the end of 1997 to 1998 is significantly different, showing nearly uniform concentrations between November 1997 through May 1998. This is caused by the deepening of the thermocline during El Niño, which depresses the nutricline. (d-f) Cross sections showing the average springtime nitrate concentration in (d) the Santa Barbara region (e) the SM region, and (f) the SD region. Background are model outputs and dots are CalCOFI *in situ* measurements. Model and *in situ* data agree on the vertical and seasonal patterns in the three regions. They highlight the main differences in these three regimes, consisting of a shallower nitracline in the Santa Barbara Channel, and a deeper nitracline in southern waters. (g-h) Comparison of nitrate concentrations during (g) winter El Niño (January-March 1998) and (h) during an upwelling event (the first week of May 1999) to illustrate the ability of the model (vs. *in situ* CalCOFI data) to simulate the vertical displacement of the nitracline during these specific events.

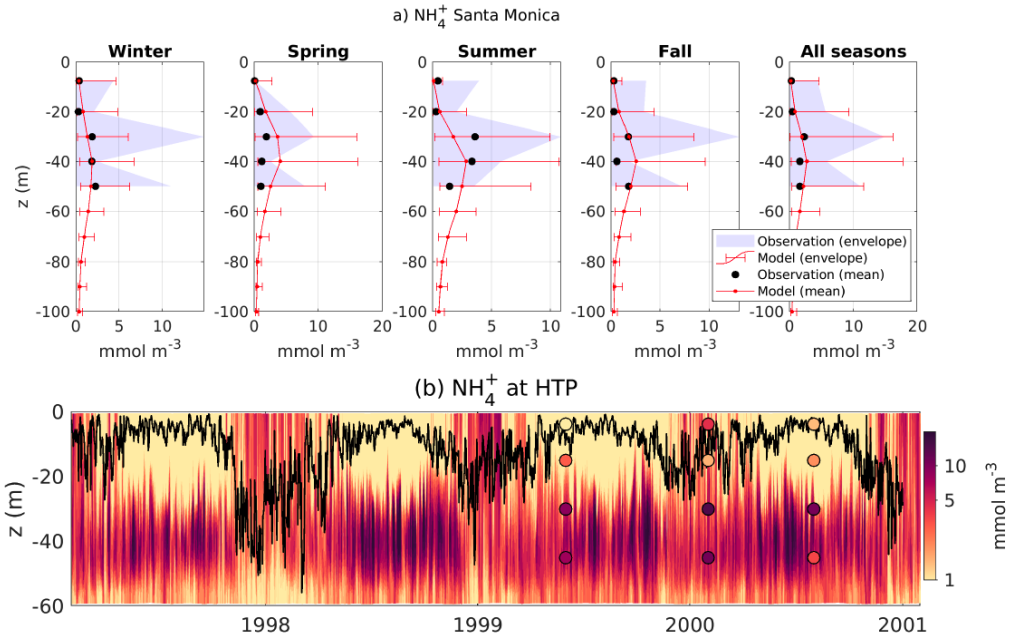

Figure 8: As for Fig. 5, but for ammonium concentration. These profiles are showing agreement on intensity, seasonality and shape of the vertical profile with exceptionally high concentrations at mid-depth.

4.3.2 Vertical gradients and seasonal variability of ammonium

Ammonium concentrations above a natural background concentration of 1 mmol N m^{-3} are indicative of POTW wastewater plumes. The model reproduces the observed average vertical profile of ammonium in the Santa Monica Bay, falling within the range of observed variability (Fig. 8a). Similar figures for other regions are shown in the Supporting Information (Fig. S6-Fig. S9). All regions show a similar maximum concentration between 30 to 45 m below the surface, in all seasons. The highest concentrations are seen in summer, when stratification is stronger, while lower concentrations in winter likely reflect increased dilution by seasonal mixing from the deepening of the mixed layer (Fig. 8b). Near ocean outfalls, both model and observations show mid-depth peaks of ammonium concentration, occasionally exceeding 10 mmol m^{-3}, which considerably overshadow values observed away from outfalls. In the model, these high ammonium concentrations are caused by wastewater plumes.

The main source of uncertainty in data-model comparisons is the limited spatial and temporal coverage of measurements. Ammonium is typically measured near ocean outfalls and is therefore biased towards high concentrations, but the dataset is highly variable. Methodological difficulties exist with the measurement of ammonium in seawater, and as such, we excluded non-detectable ammonium values in our analyses. Near the submarine outfalls, ammonium concentrations are likely extremely heterogeneous due to buoyant plume filaments, as observed in DiGiacomo et al. (2004) and in Warrick et al. (2007) in the Santa Monica Bay, as well as in other regions (e.g. Florida, in Marmorino et al. (2010)). These plume filaments are caused by horizontal advection and straining of the discharged effluent by currents. As a result, the under-sampling of ammonium may have led to poor statistical agreement between observations and model output. The model shows high to moderate agreement for the shape of the profile and the mean concentration (Table 3). However,

p-values for the correlations were not always significant. Similarly, there were often biases and low performance regarding variability statistics. This low model performance can be explained by the following two reasons: (1) spatial sampling is likely missing plume filaments, for example observational data points with high ammonium values that are capturing the plume are recorded next to very low or non-detectable values; and (2) the resolution of the model (0.3 km), as well as model averaging over the day, season, and depth range causes plume filaments to appear more uniformly spread near the outfalls. Because plume filaments are lost in this averaging, the model represents plumes as cloud-like distributions around outfalls; nevertheless, the average ammonium concentration of wastewater plumes is reasonably well represented. Detailed information on the other sub-regions and their statistical comparison can be found in the Supporting Information Tables S1 to S4.

4.3.3 Horizontal gradients of ammonium

Both *in situ* observations (dots in Fig. 9, Fig. 8a) and model output (background colours in Fig. 9 and red line in Fig. 8a) show high concentrations of ammonium in the subsurface layer below the thermocline (Fig. 9c), which we refer to as "high-ammonium plume". This high-ammonium plume can extend from Huntington Beach to South Ventura, encompassing three of the four major wastewater treatment plant outfalls in the SCB (See Section 2.4). Both model and observations show that the width and strength of the high-ammonium plume are greatest in summer compared to other seasons. The Santa Monica Bay Observatory mooring (SMBO, Leinweber et al. (2009)) located 17 km north-west of the submarine pipe Hyperion in Santa Monica Bay (Fig. 9g) frequently recorded concentrations higher than 2 mmol m^{-3}, and up to 4 mmol m^{-3} at mid-depth (Fig. 9e), consistent with the model (Fig. 9f). The depth of the maximum variability is at 40 m in the model, and slightly shallower in the SMBO data, possibly because of a mismatch in the time period (1997-2000 for the model, and 2004-2010 for the SMBO). During winter, the model indicates vertical mixing and dilution of the plume at the surface. Accordingly, ammonium concentrations decrease slightly at depth (Fig. 9a) and increase at the surface, reaching values up to 2-6 mmol m^{-3}, also consistent with observations around the outfall pipes (Fig. 8a).

4.3.4 Spatial patterns in rates of nitrogen transformation

Although we had no *in situ* nitrogen transformation rates with which to compare model output during the simulation period, several datasets exist for the region that can serve as a test for whether the model is simulating reasonable patterns in rates via the right mechanisms. We found that modeled rates do agree with observed nitrogen transformation rates. Nitrification rates, the sequential oxidation of NH_4^+ to NO_3^- via NO_2^-, have been observed to be higher within wastewater plumes in the SCB (McLaughlin et al., 2021), a pattern driven by high ammonium concentrations in the discharges (McLaughlin, Nezlin, et al., 2017). In both observations and the model, nitrification predominately occurs below the euphotic layer. Modeled vertically-integrated nitrification rates vary between 0.15 and 1.5 mmol N $m^{-2}d^{-1}$, consistent with observations within the SCB and in the California Current (Table 5). The model also reproduces higher nitrification rates within wastewater plumes (See Supporting Information Fig. S22). There is also good agreement between observed and modeled rates of nitrate and ammonium uptake by phytoplankton communities (McLaughlin et al., 2021) and (Kudela et al., 2017). Modeled nitrate uptake rates vary between 2 and 11 mmol N $m^{-2}d^{-1}$ and ammonium uptake rates vary between 6 and 51 mmol N $m^{-2}d^{-1}$ in the Los Angeles and Orange County coasts, consistent with observations in the SCB (Table 5).

4.4 Chlorophyll concentrations

In general, the model was found to reproduce vertical and horizontal gradients in chlorophyll concentration in different subregions (Fig. 12). The timing of blooms was consistent

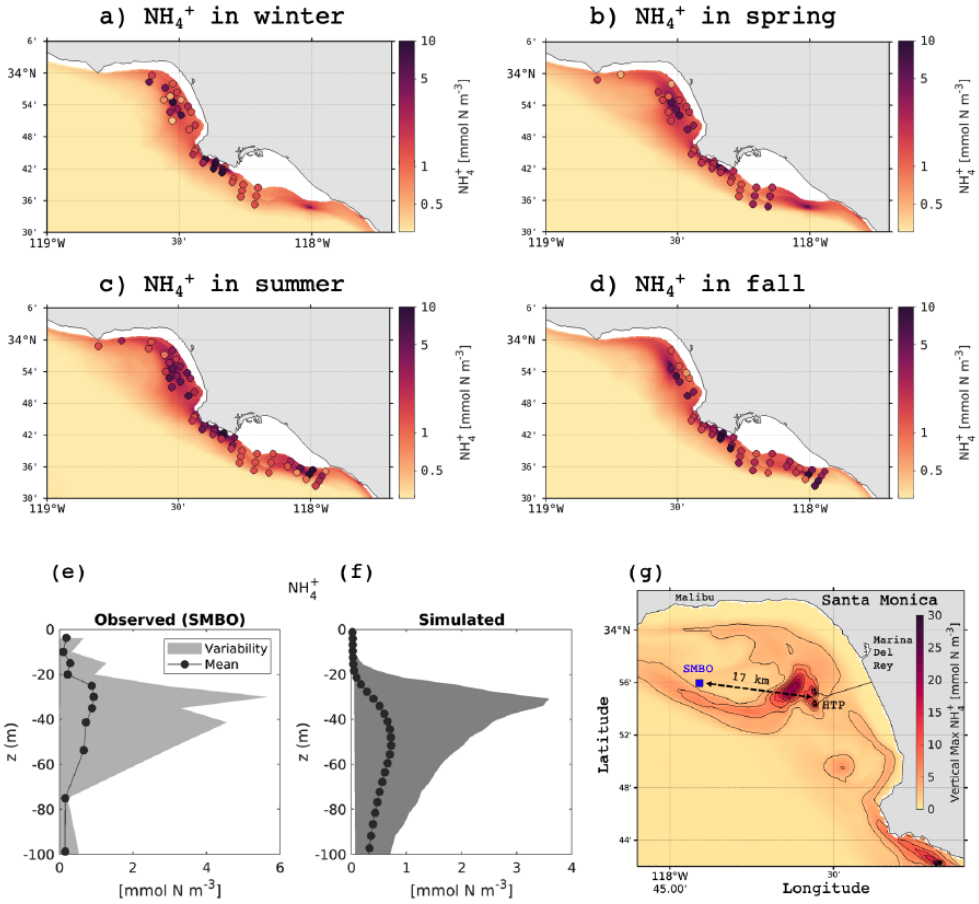

Figure 9: (a-d) Colors show seasonal average ammonium concentration between 30 and 45 m depth from the model, and dots from observations. High values highlight the movement and dispersion of subsurface wastewater plumes along the Orange and Los Angeles counties. The highest concentrations are located within a narrow coastal band of about 10 - 15 km width, and are carried along the topography by the mean currents. (e-f) show a statistical comparison of the vertical profiles of ammonium at the SMBO mooring and the same location in the model. The anthropogenic ammonium plume signature is apparent, albeit intermittently, 17 km away from the Hyperion outfall. (g) shows the simulated vertical maximum concentration of NH_4^+ averaged during a representative day to illustrate the dispersal of the effluent toward SMBO originating from the 2 diffusers of Hyperion Treatment Plant (HTP).

with changes in mixing and nutrient delivery in the SCB. We present three different subregions characterized by distinct hydrodynamic regimes: the Santa Barbara Channel, the Los Angeles coast, and San Diego coast.

There are several sources of uncertainty in the chlorophyll, primary production, phytoplankton growth, and grazing rates observational records. For chlorophyll, bottle measurements are accurate and precise, but measure a limited portion of the water column. Sensors are accurate and precise in their measurement of fluorescence and have a rapid response time, providing vertically resolved profiles; however, the algorithm to convert fluorescence to chlorophyll concentration is inaccurate for the SCB. As a result, a correction factor has been applied to Bight data which adds uncertainty to the observational dataset (Nezlin et al., 2018). Satellite measurements of chlorophyll are inferred from ocean color (Kahru et al., 2009). This method works well offshore, but breaks down nearshore where terrestrially-derived colored dissolved organic matter creates uncertainty in reported satellite chlorophyll estimates on the order of 100% or greater (Zheng & DiGiacomo, 2017). For primary production, the incubation method to derive the rates is sensitive and precise (Cullen, 2001), though measured rates are subject to bottle effects and there is some ambiguity as to whether the experiments measure net primary production or gross primary production (Regaudie-de Gioux et al., 2014). Phytoplankton growth and zooplankton grazing are also determined experimentally, and duplicate measurements indicate that these methods are not very precise, with differences between duplicates ranging from 80% to 200% (Landry et al., 2009; Li et al., 2011). For all three measurements, spatial and temporal under-sampling, particularly during seasons with high variability, adds uncertainty to the data-model comparison.

4.4.1 Horizontal gradients in chlorophyll

Despite the uncertainties outlined above, the model successfully simulates horizontal gradients in chlorophyll in the three subregions (Santa Barbara, Los Angeles and San Diego). The model captures the early, wide-spread spring bloom in the Santa Barbara Channel, which occurs as a combination of a coastal bloom driven by spring upwelling, followed by a bloom in the central and southwestern regions of the Channel (near the islands) in spring and summer (Fig. 10). The latter is driven by the strengthening of the cyclonic circulation in the Channel, which transports nutrients to the upper layers, and is regularly observed in the region (Brzezinski & Washburn, 2011). The model captures the strong seasonality in chlorophyll, wherein concentrations change from near zero in winter to up to 8 mg Chl m^{-3} in spring. Of the three regions, the blooms off Santa Barbara extends further into late summer and fall, where the average concentration is approximately 1-2 mg Chl m^{-3}, a pattern replicated in both model and observations .

In the Los Angeles subregion, the model predicts broad patterns in chlorophyll concentrations, including a persistent bloom in the San Pedro Bay, consistent with observations (Nezlin et al., 2012), and validated by comparison with remote sensing (Fig. 11). Both satellite-derived and modeled chlorophyll show concentrations in the San Pedro Bay consistently higher than 3 mg Chl m^{-3} year-round, often extending into the Santa Monica Bay. The model also reproduces the strong offshore gradients in chlorophyll, where across less than 15 km offshore surface concentrations are reduced 3 to 4 fold ($<$1 mg Chl m^{-3}) further decreasing towards the open ocean. The model also reproduces the timing and magnitude of the blooms in the Santa Monica and San Pedro Bays. The difference in timing of maximum chlorophyll concentrations between the Santa Monica and San Pedro Bays likely reflects differences in nutrient supply. Nutrients, in particular ammonium, are available near the surface during winter (see Section 4.3.2), reflecting more vigorous mixing of the wastewater plume and land-based nutrient supply by rivers (in particular in the San Pedro Bay) during winter storms (Lyon & Stein, 2009). Storms and winter mixing events have been connected to phytoplankton blooms in the region (Nezlin et al., 2012; Mantyla et al., 2008). Further offshore in the Los Angeles region, the model recreates the weak seasonality of surface chlorophyll, with higher concentrations during winter and spring, and lower concentrations

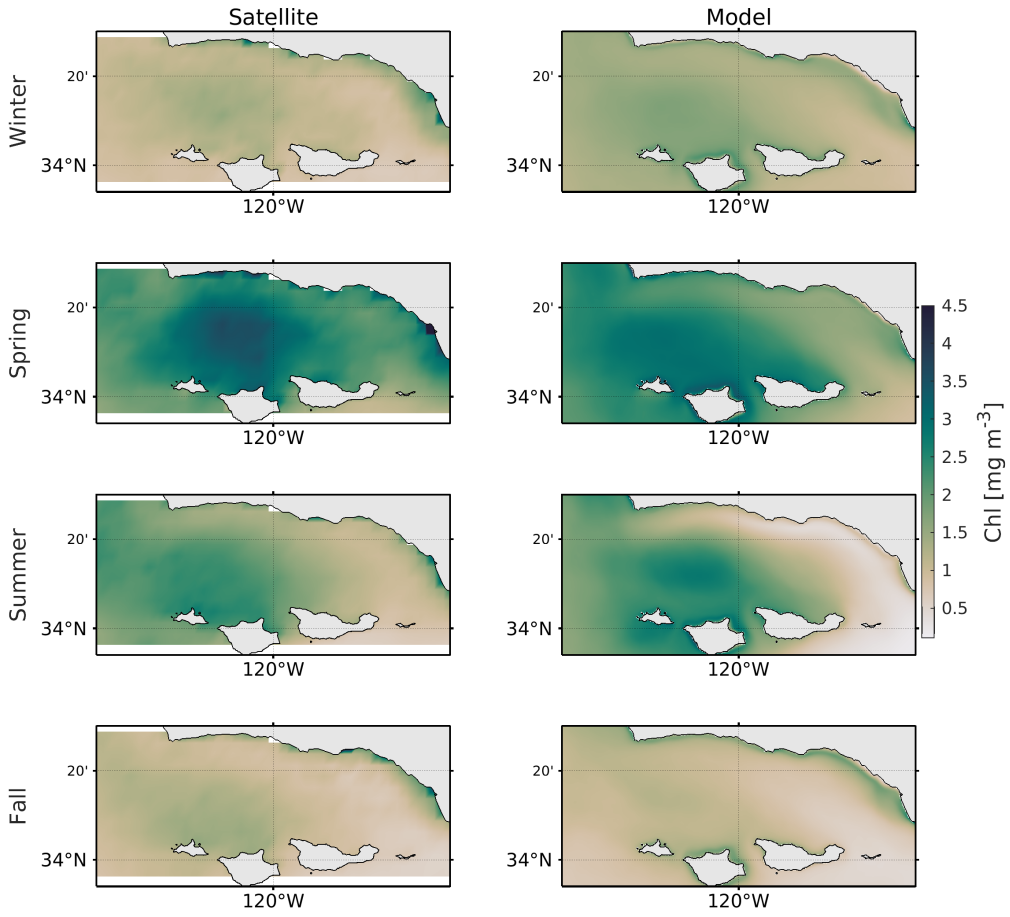

Figure 10: Comparison of seasonally-averaged surface chlorophyll between SeaWiFS remote sensing data (left panels) and the model (right panels) in the Santa Barbara Channel, where an important seasonal bloom is observed.

in summer and fall. In the offshore region of the Santa Monica Bay, the seasonal cycle is marked by the increase of surface phytoplankton between March and May as shown in Fig. 12b. Mean chlorophyll values reach up to 3 to 4 mg Chl m^{-3} in April and May, although concentrations below 2 mg Chl m^{-3} are more common, consistent with observations over the same period.

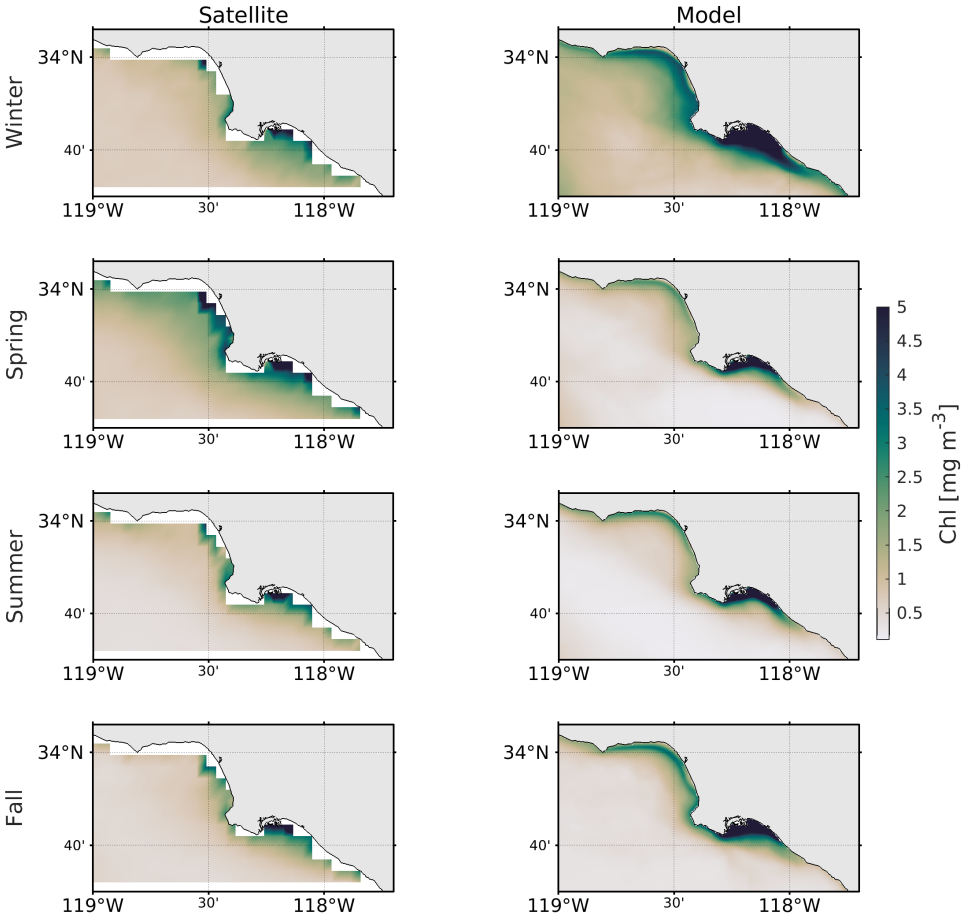

Figure 11: Comparison of seasonally-averaged surface chlorophyll between SeaWiFS remote sensing data (left panels) and the model (right panels) for years 1998-2000 in the Santa Monica and San Pedro Bays, where major POTW outfalls are found. The figure highlights the persistent coastal phytoplankton bloom, and the sharp inshore-offshore gradients.

Offshore of the San Diego coast, the model recreates a slight increase in surface chlorophyll in March; however, concentrations are generally below 1 mg Chl m^{-3} year-round (Fig 12(c)). The oligotrophic conditions of the southern Bight (Nezlin et al., 2012; Mantyla et al., 2008) have been attributed to a deeper nitracline, which in turns supports a deep chlorophyll maximum layer (Mantyla et al., 2008). This feature is well represented in the model, which reproduces relatively high concentrations of chlorophyll in subsurface layers (generally between 20 and 90 m depth in the region).

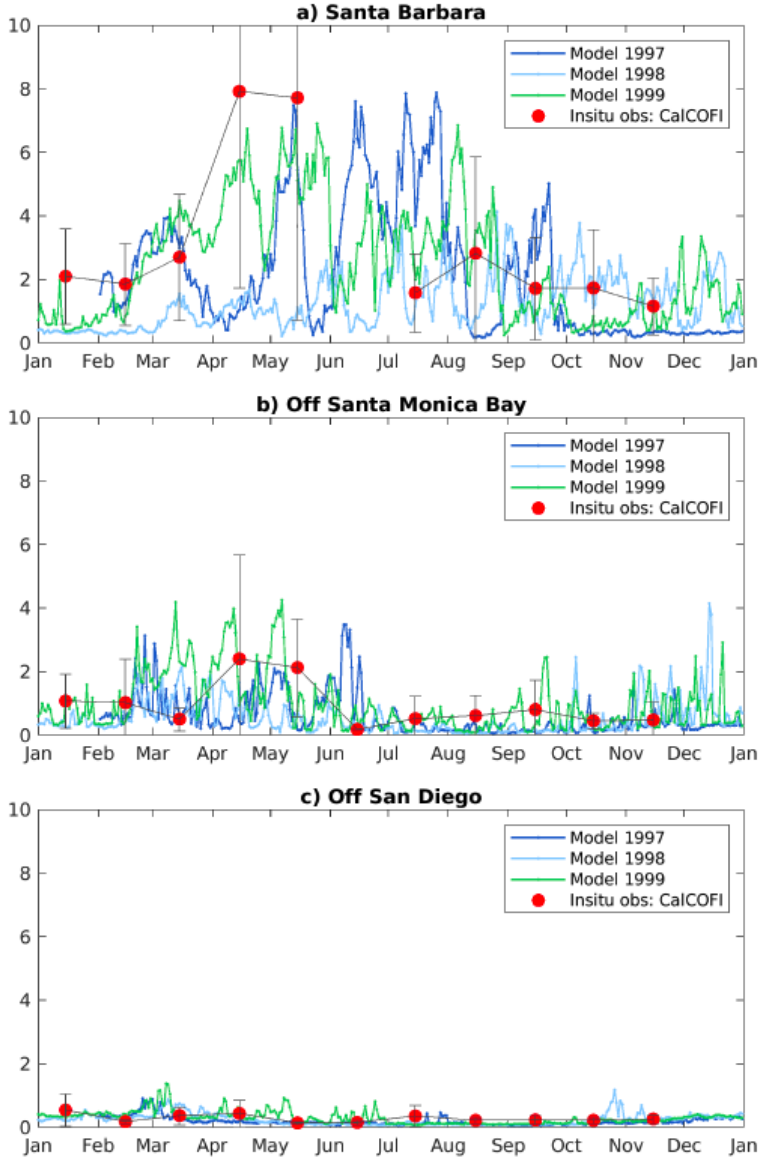

Figure 12: Comparison of surface chlorophyll concentration between different years of model output, and a climatology from CalCOFI *in situ* data. (a) is near the center of Santa Barbara Channel, (b) is offshore the Santa Monica Bay, and (c) is offshore San Diego. The model reproduces different productivity regimes across the Southern California Bight, with highly productive waters in the northern region, where average concentrations greater than 3 mg m^{-3} are observed for more than half of the year, and oligotrophic southern regions, where average surface concentrations rarely exceed 1 mg m^{-3}.

4.4.2 Vertical gradients and seasonal variability of chlorophyll

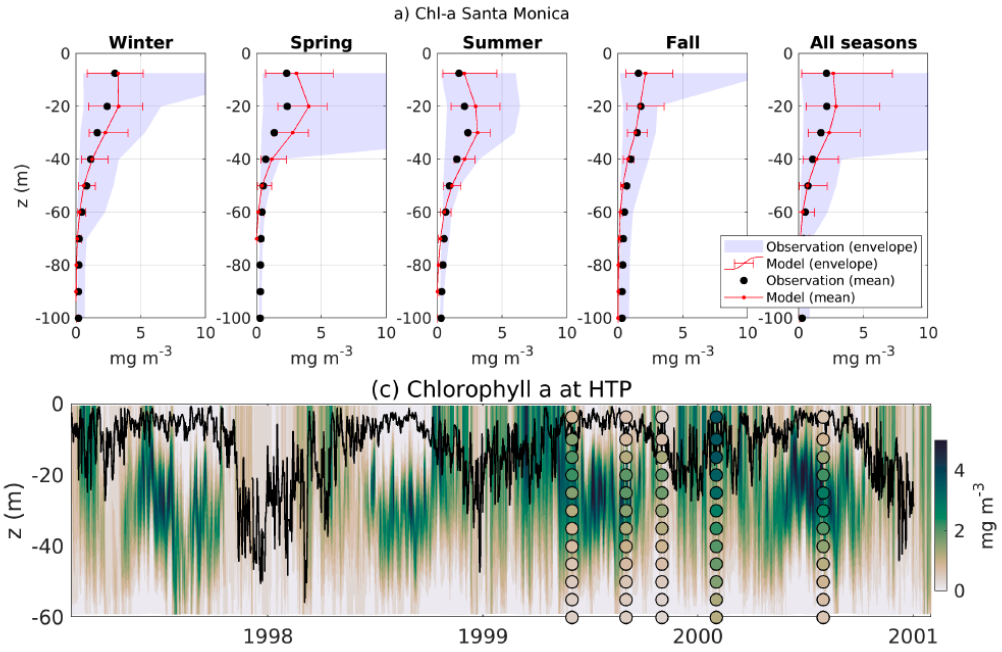

Figure 13: As for Fig. 5, but for chlorophyll concentration. Vertical profiles show a good agreement between simulated and *in situ* data, and display the formation of a subsurface chlorophyll maximum in summer, and a surface maximum in winter and spring. Concentrations in winter vary up to +5 mg Chl m^{-3}. Note the very low concentrations during 1998 El Niño in the entire water column.

The goodness-of-fit statistical metrics (correlation coefficient and cost function) for chlorophyll are generally *excellent* or *good* for most seasons for all sub-regions (Table 4). We were most concerned with performance for these metrics because the remaining statistics may be affected by the aforementioned uncertainties due to the fluorometry calibration. The observational measurements should be internally consistent (if not accurate), so the shapes of profiles should be "correct" even if the magnitude is off due to poor calibration, and the model was able to replicate these shapes accurately. Despite calibration issues, the model reproduced chlorophyll reasonably well for the northern Bight sub-regions of Santa Monica Bay (Fig. 13) and Ventura/Oxnard (SI Fig. S11). Similar figures for other regions are shown in the Supporting Information (Fig. S10-Fig. S13). All show that the model is reproducing the magnitude and general shape of observed profiles. However, the model did not capture the variability for most regions (except for Palos Verdes), generally scoring *reasonable* or *poor* in the ratio of standard deviations for most seasons, particularly spring. This is likely a result of the spatial and temporal averaging. Chlorophyll is highly variable in space and time and under-sampling in either of these dimensions will adversely affect variability estimates for a region and season. Therefore, reasonable performance for these metrics was not unexpected. This suggests that the model may provide a conservative estimate of phytoplankton biomass in the southern Bight, while reproducing accurate spatial and temporal patterns in that biomass.

In addition to transporting nutrients from depth, upwelling 'seeds' surface waters with subsurface water masses dominated by selected phytoplankton species, stimulating surface blooms near the coast (Seegers et al., 2015). The model successfully reproduces this process,

wherein the subsurface chlorophyll maximum shoals and intensifies in spring, forced by the vertical movement of the thermocline driven by upwelling. This seasonal dynamics occurs across the domain in the model.

Offshore, in the more oligotrophic portion of the SCB, the model predicts that more than 60% of the maximum concentration of phytoplankton biomass remains below the surface year-round, constantly fed by subsurface nutrients injections. This is consistent with observations of a deep chlorophyll maximum throughout the region (Nezlin et al., 2018; Mantyla et al., 2008; Seegers et al., 2015), and with observations at the San Pedro Oceanic Time-Series (SPOT) located between the Palos Verdes Peninsula and Catalina Island (Fig. 3, lower panel). At SPOT, a region weakly influenced by anthropogenic nutrients inputs at the surface, the model realistically simulates the seasonal cycle of chlorophyll. While ammonium does not exceed typical "natural" values of $\sim$1 mmol m^{-3} below the surface, chlorophyll concentrations regularly reach more than 2 mg m^{-3} between 20 and 40 m in summer, in agreement with *in situ* measurement (Teel et al., 2018; Beman et al., 2011). (Additional figures to support the analysis are reported in the Supporting Information, Fig. S23.)

However, in regions more heavily influenced by anthropogenic nutrients, such as the Santa Monica Bay, the chlorophyll maximum progressively deepens from the surface in winter to about 25 to 30 m depth in spring and summer, with chlorophyll concentrations exceeding 5 mg Chl m^{-3} (Fig. 13a). This subsurface chlorophyll maximum is maintained for four to five months (Fig. 13b) before the stratification is weakened by winter mixing.

4.4.3 Primary production

Validation of the rates of primary production, phytoplankton growth and zooplankton grazing (Table 5) provides an independent check on mechanisms responsible for chlorophyll as a state variable. The spatial and temporal frequency of these data, garnered from CalCOFI observations and literature values, is low. The most data as well as the most standardized methodologies are available for primary production. However, many of the primary production measurements used in this validation do not temporally coincide with the model period. Despite these uncertainties, the model generally reproduces expected large-scale patterns and seasonal variability in primary production.

This large scale variability was also mentioned in Deutsch et al. (2020). Model and data both show lower productivity in winter (Fig. 14a,c) and higher in spring (Fig. 14b,d), when the primary production is high along the coastal band, in the northern Bight around the Channel Islands (Fig. 14d), consistent with observations (Fig. 14b). This is also consistent with the so-called "green ribbon" of high-chlorophyll observed along the coast throughout the SCB (Lucas et al., 2011). The model reasonably reproduces the seasonal cycle of primary production in each of the subregions.

Phytoplankton are generally limited by a combination of nutrients and light, the latter of which is only limiting at depth in the SCB (Deutsch et al., 2020).

In winter, nitrogen is high at the surface in the northern SCB, and thus is not limiting. In the southern SCB, light and nitrogen are co-limiting due to stronger stratification, leading to oligotrophic conditions. In spring and through the summer, nitrogen is limiting nearly everywhere except in the Santa Barbara Channel and near the Channel Islands, where upwelling and submesoscale eddies maintain high nutrients at the surface.

The scatter plots in Fig. 14e-f show a comparison of the simulated primary production between the *in situ* CalCOFI data and that derived from remote sensing (empirically adjusting the Behrenfeld-Falkowski Vertically Generalized Production Model [VGPM]). The model shows a correlation coefficient of about 0.6 with CalCOFI, similarly to that reported by Kahru et al. (2009) when comparing the VGPM product with CalCOFI. The model

Santa Monica: chlorophyll								
	H	Correlation Coefficient	p-value	Cost Function	Percentage Bias	Ratio of Standard Deviations	Nash-Sutcliffe Model Efficiency	Number of observations
Winter	0 E	0.99 E	9E-06 E	0.48 E	0.09 E	0.91 E	0.94 E	714
Spring	0 E	0.93 E	9E-05 E	0.90 E	-0.42 P	0.52 P	-0.49 P	716
Summer	0 E	0.99 E	1E-08 E	0.58 E	-0.07 E	0.60 R	0.47 R	712
Fall	0 E	0.99 E	8E-08 E	0.48 E	0.16 G	0.75 R	0.76 E	718
All Seasons	0 E	0.99 E	4E-08 E	0.50 E	-0.01 E	0.73 R	0.80 E	2860

Table 4: Statistical comparison between *in situ* data and model outputs for chlorophyll profile in Santa Monica Bay.

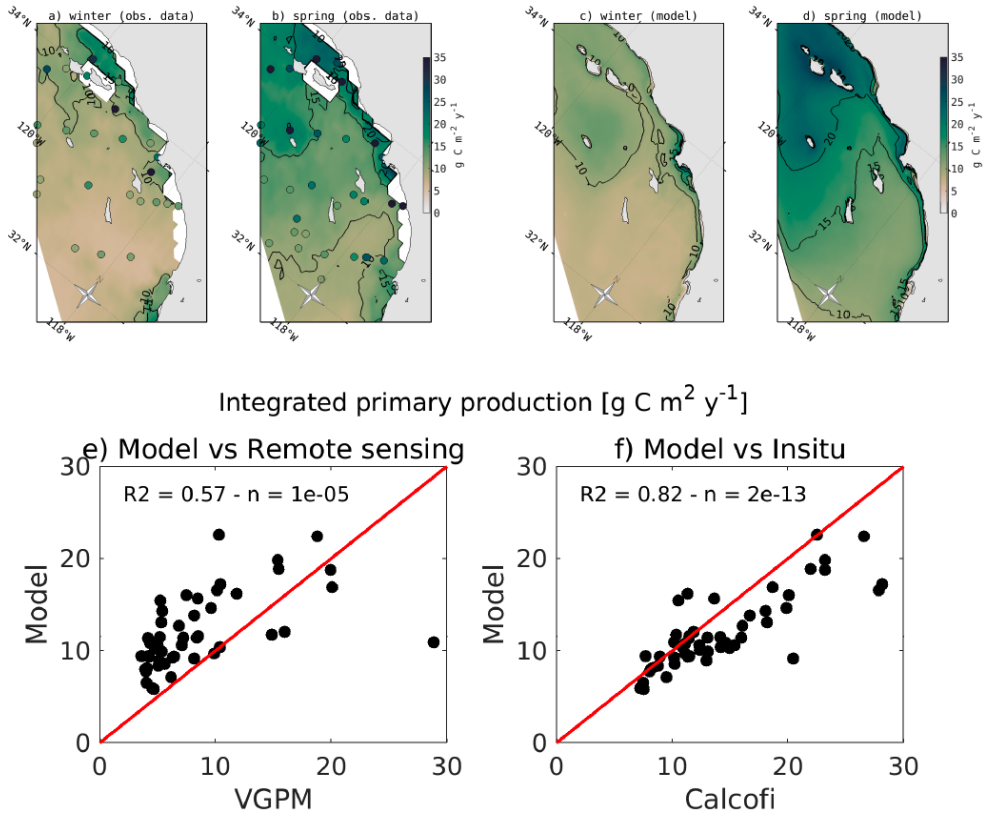

Figure 14: (a)-(b) Maps of vertically integreated Vertically Generalized Production Model (VGPM) net primary production and CalCOFI *in situ* measurements plotted as dots for (a) winter (January and February) and (b) spring (April to June). (c)-(d) Maps of vertically integrated primary production from the model, in (c) winter and (d) spring. Note the higher values for CalCOFI *in situ* measurements as compared to the satellite estimate, in better agreement with the model.

shows a stronger correlation with VGPM data, with a correlation coefficient of the order of 0.8.

Finally, while slightly outside our model domain and simulation period, the modeled phytoplankton growth and zooplankton grazing rates were within the same order of magnitude as the measured rates from the California Current Long Term Ecological Research project (CC-LTER, see Landry et al. (2009), and Table 5) in the northern portion of the Bight.

	Bight 13	Literature	Model
Primary production (g C m^{-2} y^{-1})	47.4, 1037.4		250, 1660
Nitrification (mmol m^{-3} d^{-1})	0, 0.225	0.02, 0.08	0.001, 0.27
NO_3^- Uptake Rate (mmol N mg Chl^{-1} d^{-1})	0.005, 2.16		0.03, 0.15
NH_4^+ Uptake Rate (mmol N mg Chl^{-1} d^{-1})	0.10, 8.30		0.08, 0.15
Total Phytoplankton Growth μ (d^{-1})		0.05, 0.8	0.3, 0.4
Grazing (d^{-1})		0.02, 0.5	0.3, 1.5

Table 5: Comparison of biogeochemical rates between published literature and model. Values are minimum and maximum. Literature values come from Landry et al. (2009); Li et al. (2011). Bight 13 is extracted from (McLaughlin et al., 2021) study.

4.5 Carbonate system and oxygen parameters

The model predicts changes in dissolved oxygen and carbon-system parameters related to photosynthesis and respiration, as well as horizontal transport and vertical mixing. As described in section 4.4.1, the coasts of Los Angeles and Santa Barbara are hot-spots of intensified plankton activity, and both systems are impacted by high variability and small-scale eddy circulation. In the upper layers, photosynthesis increases both dissolved oxygen and pH (Figs. 16 and 18), consistent with observations in these regions. The Santa Monica Bay shows the highest oxygen production rates (60 mmol m^{-2} d^{-1}), followed by the Santa Barbara coast (57 mmol m^{-2} d^{-1}), while rates in the Orange County and San Diego coasts are nearly two times lower. Oxygen and carbon are further replenished at the surface by air-sea gas exchange with the atmosphere. Export of newly-fixed organic carbon leads in both regions to high remineralization rates that consume oxygen and release carbon dioxide at depth. We simulate similar high organic matter export (around 30 mmol m^{-2} d^{-1}) in the Santa Barbara and Los Angeles coasts (see Supporting Information: Fig. S24).

The reliability of these predictions can be tested by validation of dissolved oxygen and carbonate system parameters. There are several sources of uncertainty in the dissolved oxygen, pH, and aragonite saturation state observational records, which affect data-model comparisons. For dissolved oxygen, sensors are relatively accurate and precise and have a rapid response time ($<$ 1s) when generating vertically resolved profiles. Repeated field measurement accuracy for CTD dissolved oxygen sensors was reported to be approximately 8 mmol m^{-3} (Coppola et al., 2013). The pH observational record is particularly fraught with uncertainty. An evaluation of pH sensor data in the SCB indicated that, while sensor pH measurements were well correlated with discrete bottle samples collected at the same depth, there was a clear bias in pH, with sensor measurements under-predicting bottle measurements and high variability in the differences between paired bottle and sensor measurements (ΔpH ranging from +/- 0.5) (McLaughlin, Dickson, et al., 2017). The aragonite saturation state is estimated using an algorithm developed for the region (Juranek et al., 2011) for both *in situ* observations and model output, because complete measurements of carbon-system parameters required to calculate Ω_{Ar} are missing. For all three variables, spatial and tem-

poral under-sampling, particularly during seasons with high variability, adds uncertainty to the data-model comparison.

4.5.1 Vertical gradients and seasonal variability of dissolved oxygen

The model reproduces observed seasonal and spatial patterns in dissolved oxygen concentration (Fig. 15), accurately simulating magnitude, vertical and horizontal gradients, and variability. Quantitative statistical analysis (see Table 6) indicated that the model performance was '*excellent*' or '*good*' for nearly all metrics for all regions and seasons. The lowest performance of the model was characterized as '*poor*' for two sub-regions for the Nash-Sutcliff Model Efficiency during Spring, and '*reasonable*' for some metrics in some sub-regions, which may be related to under-sampling during seasons with high variability, as described above. Similar to temperature, we tested whether the variability in spring may be impacting the performance statistics by extracting random profiles for the region (not shown, expressed with large error-bars in the spring season plots in Fig. 16), which show how dissolved oxygen on a single arbitrary day can more closely align with the observations. This supports the hypothesis that observational uncertainty is behind the lack of observational agreement with the model. Model performance was lowest in the Orange County and San Diego subregions, where model predictions tended to overestimate dissolved oxygen, consistent with the chlorophyll under-prediction, a likely consequence of the lack of cross-border inputs from Mexican waters.

The model also reproduces the seasonality in dissolved oxygen in all subregions (Fig. 16), characterized by large meridional and vertical variability. Near the Channel Islands, dissolved oxygen varies at 50 m by up to 140 mmol O_2 m^{-3} between the highest winter values and the lowest summer values, reflecting the dynamics of upwelling, productivity, and air-sea gas-exchange. Offshore the coasts of Santa Monica and San Diego, the variability between winter and summer is of the order of 80-90 mmol O_2 m^{-3}. Surface concentrations are everywhere above 240 mmol O_2 m^{-3} year-round, consistent with observations. The highest summer concentrations are observed at the depth of the deep chlorophyll maximum, reflecting photosynthesis, while decreasing at depth to below 150 mmol O_2 m^{-3}. These patterns are generally consistent with observations in the same regions.

During the 1998 El Niño event, the model shows a net decrease of dissolved oxygen near the surface, and a net increase below it. During this period, the entire upper layer (0-80 m) is characterized by a homogeneous oxygen concentration of about 240 mmol O_2 m^{-3} over almost the entire SCB (not shown). Only the San Pedro and Santa Monica Bays show higher concentrations, which we attribute to the local anthropogenic nutrient enrichment and subsequent blooms (see Fig. 19). This is consistent with observations of the 1998 El Niño event in California coastal waters (Chavez et al., 2002; Booth et al., 2014).

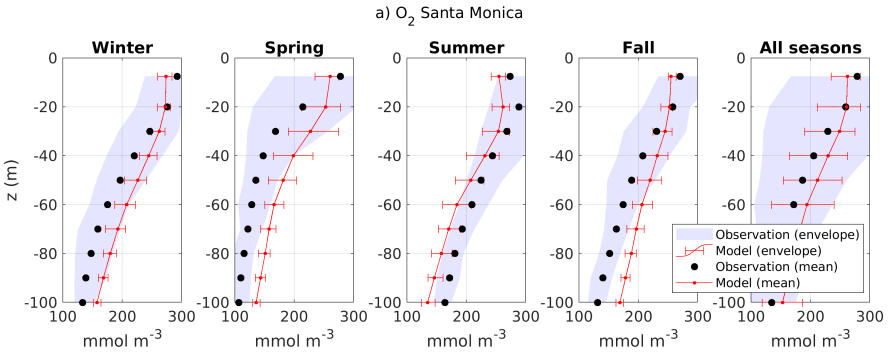

Figure 15: As for Fig. 5, but for oxygen concentration.

Santa Monica								
					Oxygen			
	H	Correlation Coefficient	p-value	Cost Function	Percentage Bias	Ratio of Standard Deviations	Nash-Sutcliffe Model Efficiency	Number of observations
Winter	0 E	0.97 E	9E-07 E	0.14 E	-0.09 E	1.20 G	0.77 E	716
Spring	0 E	0.91 E	3E-04 E	0.26 E	-0.23 R	1.03 E	0.37 R	702
Summer	0 E	0.99 E	2E-10 E	0.07 E	0.07 E	0.99 E	0.86 E	712
Fall	0 E	0.97 E	2E-06 E	0.19 E	-0.14 G	1.49 P	0.42 R	718
All Seasons	0 E	0.97 E	3E-06 E	0.14 E	-0.11 G	1.18 G	0.69 E	2848
					pH			
	H	Correlation Coefficient	p-value	Cost Function	Percentage Bias	Ratio of Standard Deviations	Nash-Sutcliffe Model Efficiency	Number of observations
Winter	0 E	0.99 E	2E-08 E	0.01 E	0.01 E	0.59 P	0.57 G	632
Spring	0 E	0.97 E	2E-06 E	0.02 E	-0.02 E	1.45 P	0.15 P	702
Summer	0 E	0.96 E	9E-06 E	0.01 E	0.01 E	1.01 E	0.85 E	712
Fall	0 E	0.97 E	3E-06 E	0.01 E	0.01 E	1.49 P	0.78 E	715
All Seasons	0 E	0.97 E	5E-06 E	0.01 E	-0.01 E	1.12 G	0.84 E	2761

Table 6: Statistical comparison between *in situ* data and model outputs for dissolved oxygen and pH profile in Santa Monica Bay.

4.5.2 Vertical gradients and seasonal variability of carbon-system parameters

Together with pH, the saturation state of aragonite (Ω_{Ar}) is often used as a metric to identify the potential impact of Ocean Acidification on marine calcifiers, because it is a measure of the availability of carbonate ions for calcium carbonate precipitation (Bednarsek et al., 2019). Ω_{Ar} shows similar vertical variability as dissolved oxygen (Juranek et al., 2009; Alin et al., 2012). Similar to oxygen loss, reduction in pH and Ω_{Ar} in the upper layers is generally caused by coastal upwelling or by local physical processes (Feely et al., 2018). We utilize sensor pH data sets to evaluate vertical profiles in the carbonate system. Because of the known uncertainty in pH measurements, we are most concerned with how well the model reproduced the shape of the profiles (i.e., goodness of fit estimates, as with chlorophyll). Sensor-derived pH profile measurements should be internally consistent within a data set (if the sensor is working properly and if pressure issues are minimal), providing some value to goodness of fit assessments. Given these constraints, the data-model comparisons for pH sensor data were generally '*excellent*' or '*good*' for all sub-regions and all seasons. Unsurprisingly, the model performance reproducing observational means and variability was generally '*reasonable*' or '*poor*' for most sub-regions and seasons, with some, if not most, of this disagreement due to difficulties in conducting a validation of the model with large uncertainties in sensor-derived pH profiles. Recently, the CalCOFI program has incorporated Ω_{Ar} into its sampling design. Although the data do not line up with the model period, they are useful for evaluating seasonal variability in the model . Generally, the model reproduces seasonal and vertical variability in Ω_{Ar}, with higher saturation states in the summer and fall, when waters are generally more stratified, and lower values in winter and spring, when upwelling brings undersaturated waters closer to the surface. Ω_{Ar} is also much lower and more highly variable at depth . These patterns are consistent with observations throughout the SCB (McLaughlin et al., 2018).

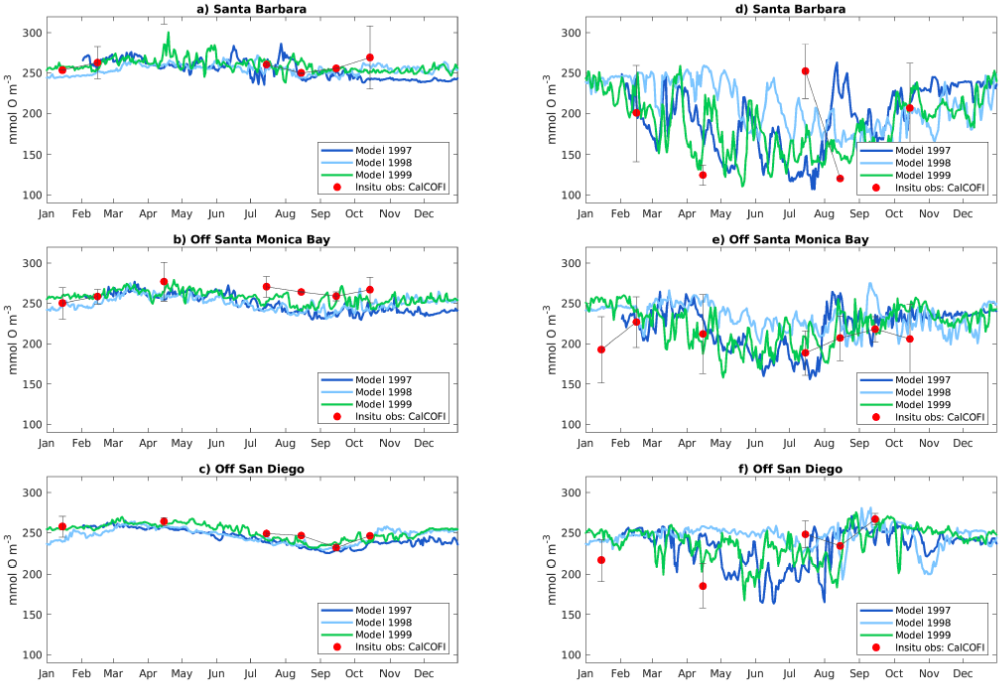

Figure 16: Comparison of dissolved oxygen concentration between different years of model output, and a climatology from CalCOFI *in situ* data. SB is near the center of Santa Barbara Channel, SM is offshore the Santa Monica Bay, and SD is offshore San Diego. Left panels show surface concentrations, right panels concentrations at 50 m depth.

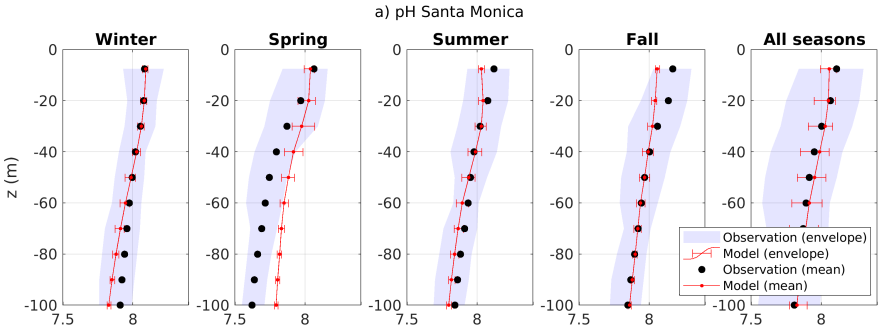

Figure 17: As for Fig. 5 but for dissolved pH.

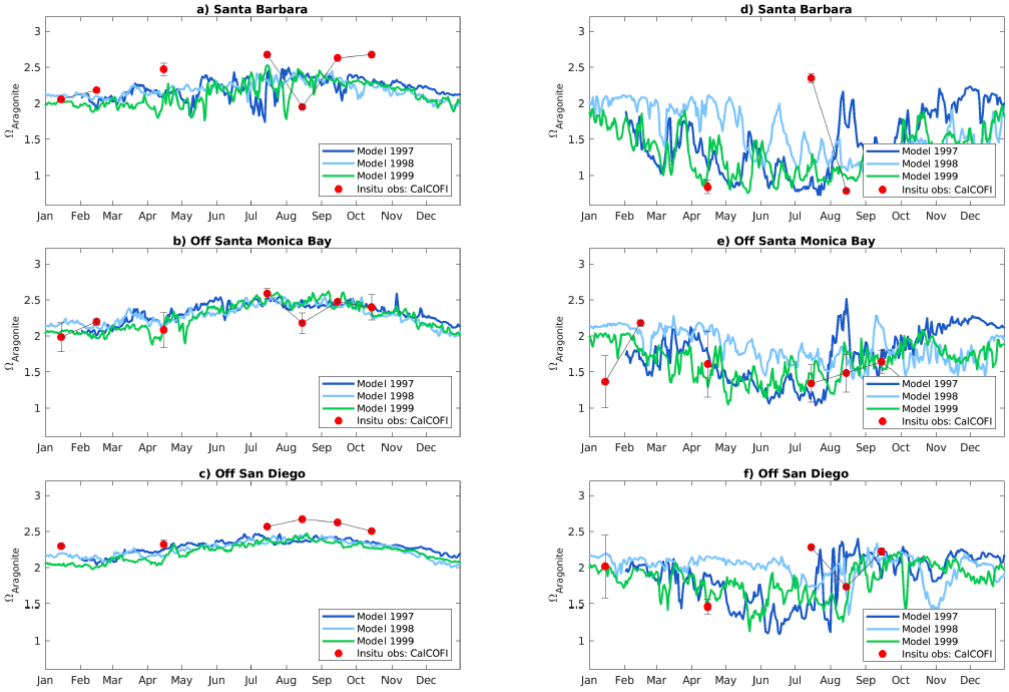

Figure 18: Comparison of the saturation state of aragonite between different years of model output, and a climatology from CalCOFI *in situ* data. SB is near the center of Santa Barbara Channel, SM is offshore the Santa Monica Bay, and SD is offshore San Diego. Left panels show surface values, right panels values at 50 m depth.

5 Summary

In this study, we demonstrated the readiness of a high-resolution, dynamically downscaled, physical-biogeochemical model to mechanistically investigate links between a comprehensive reconstruction of terrestrial and atmospheric nutrient inputs, coastal eutrophication, and biogeochemical change in the SCB coastal waters. This modeling platform is an important achievement because it strikes a balance of capturing the forcing of coastwide basin mesoscale phenomena, while capturing the combined effects of bathymetry and submesoscale eddies that intensify transport of nutrients and biological material. Moreover, this model allows to run hindcast simulations of primary production, ocean acidification and oxygen loss at timescales that can approach the multi-annual frequencies of intrinsic ocean variability, making the grand challenge of disentangling natural variability, climate change, and local anthropogenic forcing a tractable task in the near-term.

ROMS has a long history of validation and management acceptance through various applications in the CCS (e.g. Marchesiello et al. (2003); Capet et al. (2004); Capet, Colas, et al. (2008); Capet, Campos, and Paiva (2008); Capet, McWilliams, et al. (2008); Shchepetkin and McWilliams (2011); Renault, Molemaker, Gula, et al. (2016)). In contrast, experience with BEC within the SCB is more limited. Our validation study of coastal eutrophication gradients in the SCB nearshore complements the U.S. West Coast-wide study of (Deutsch et al., 2020) and strengthens confidence that the basic CCS BEC model formulation, forcing and parameterization is appropriate not only for coastwide analyses, but also for detailed local studies of coastal eutrophication in the highly urbanized SCB. The representation of physical processes such as vertical mixing and horizontal circulation was consistent across the model and measurements. The model reproduces the main structure of the climatological upwelling front and cross-shore isopycnal slopes, and the mean current patterns and associated temperature gradients. We also demonstrate good agreement between model simulations and the mean distributions and variability of key ecosystem metrics, including surface nutrients and productivity, and subsurface O_2 and carbonate saturation. The spatial patterns of primary production, phytoplankton growth rates, and zooplankton grazing are broadly consistent with measured rates. The distribution of primary production is governed by the trade-off between nutrient and light limitation, a balance that reproduces and explains the observed spatial variations in the depth of the deep chlorophyll maximum. Statistical measures of model agreement on biogeochemical state variables was excellent to good and the range of predicted biogeochemical rates on par with observations. Under the realistic flow fields produced by ROMS, the conformity of model predictions with a rich observational dataset is a strong demonstration of model validity for coastal eutrophication applications. We also demonstrated that the model responds with confidence to the variability caused by El Niño, modifying the vertical distribution of the physical and biogeochemical properties across the upper ocean of the entire Bight, as illustrated by the three-dimensional change in key ocean variables shown in Fig. 19.

While the broad agreement between the model and observations for a range of variables is encouraging, there remain aspects of the model that require further study and improvement. For example, phytoplankton diversity is limited in the model, preventing it from properly simulating events such as dinoflagellate-driven red tides, which occur over short periods on limited coastal scales in the spring. Despite the good performance of the model in reproducing total primary production and grazing rates, the model does not include multiple zooplankton functional groups, thus providing little information on the dynamics and transfer of energy of higher trophic levels. From a hydrodynamics point of view, with a horizontal resolution of 300m, the model does not directly resolve physical processes occurring at sales of tens of meters (Dauhajre et al., 2019), for example the dilution and entrainment of buoyant wastewater plumes, which is now parameterized, or the vertical and horizontal transport of tracers in the very nearshore surf zone.

Quantitative and qualitative results of confidence assessments are essential for informing management decisions, evaluating management strategies, and providing a basis for risk

analyses. The most successful management approaches are those that explicitly incorporate uncertainty (e.g. Taylor et al. (2000)). An assessment of model validation must consider the complex combination of model and observational uncertainties (Allen et al., 2007), including: 1) uncertainty/error in the model, with the inclusion of intrinsic variability; 2) uncertainty/error in measured data; 3) uncertainty from the difference in spatial scales of the model output relative to the measured data used in the comparison (specifically, comparing a 0.3 km grid cell to a discrete sampling station); and 4) uncertainty from the difference in temporal averaging of the model output relative to the measured data. For parameters in which we have high confidence in the observational record, i.e., temperature and dissolved oxygen, model performance statistics show excellent agreement for mean profiles, vertical and horizontal gradients, as well as seasonal variability. The model reproduces chlorophyll reasonably well, albeit with some biases, which can be in part attributed to a simplified representation of plankton diversity, measurement uncertainty, sparseness of *in situ* data, cloud cover and algorithm biases in satellite products. Variables such as pH and ammonium show lower agreement, likely due to measurement uncertainty and sampling bias, but general spatial and temporal patterns are correctly reproduced in the model.

Greater clarity is needed in the requirements for model performance and uncertainty to support decisions on management of SCB coastal water quality and eutrophication (Boesch, 2019). These requirements are likely to be driven largely by the approach that will be used to interpret a "significant impact" (e.g. existing water quality pH and dissolved oxygen criteria, or biologically relevant thresholds; (Weisberg et al., 2016)), as these have significant implications for required model precision and accuracy on different spatial and and temporal scales. Future efforts to constrain uncertainty could include sensitivity analyses and model ensemble comparisons of BEC with other biogeochemical models that feature increasingly complex representations of planktonic functional groups, benthic communities, and sediment-pelagic interactions. Finally, long-term investments are needed in coupled chemical-biological observations of phytoplankton and zooplankton diversity and community structure. These observations are critical to provide understanding of the evolution of lower trophic ecosystem structure with climate change, and their relationship with biogeochemical cycles linked to ocean acidification and oxygen loss (Sailley et al., 2013). Ultimately, the need to constrain uncertainty will likely scale with the economic import of management decisions under consideration, which could range from increased monitoring requirements to multi-billion dollar non-point source controls and wastewater treatment plant upgrades.

Acknowledgments

This research was supported by NOAA grants NA15NOS4780186 and NA18NOS4780174, California Ocean Protection Council grant C0100400, and NSF grants OCE-1419323 and OCE-1419450. Computational resources were provided by the Extreme Science and Engineering Discovery Environment (XSEDE) through allocation TG-OCE170017, and by the super-computer Hoffman2 at the University of California Los Angeles, at the Institute for Digital Research and Education (IDRE, UCLA). Code is available in (Kessouri, McWilliams, et al., 2020). Insitu observation data to generate the figures and statistics are available in (Kessouri, McLaughlin, et al., 2020). Local land-based and atmospheric data can be found in (Sutula et al., 2021a).

References

Alin, S. R., Feely, R. A., Dickson, A. G., Hernández-Ayón, J. M., Juranek, L. W., Ohman, M. D., & Goericke, R. (2012). Robust empirical relationships for estimating the carbonate system in the southern california current system and application to calcofi hydrographic cruise data (2005–2011). *Journal of Geophysical Research: Oceans*, *117*(C5).

Allen, J., Somerfield, P., & Gilbert, F. (2007). Quantifying uncertainty in high-resolution coupled hydrodynamic-ecosystem models. *Journal of Marine Systems*, *64*(1-4), 3–14.

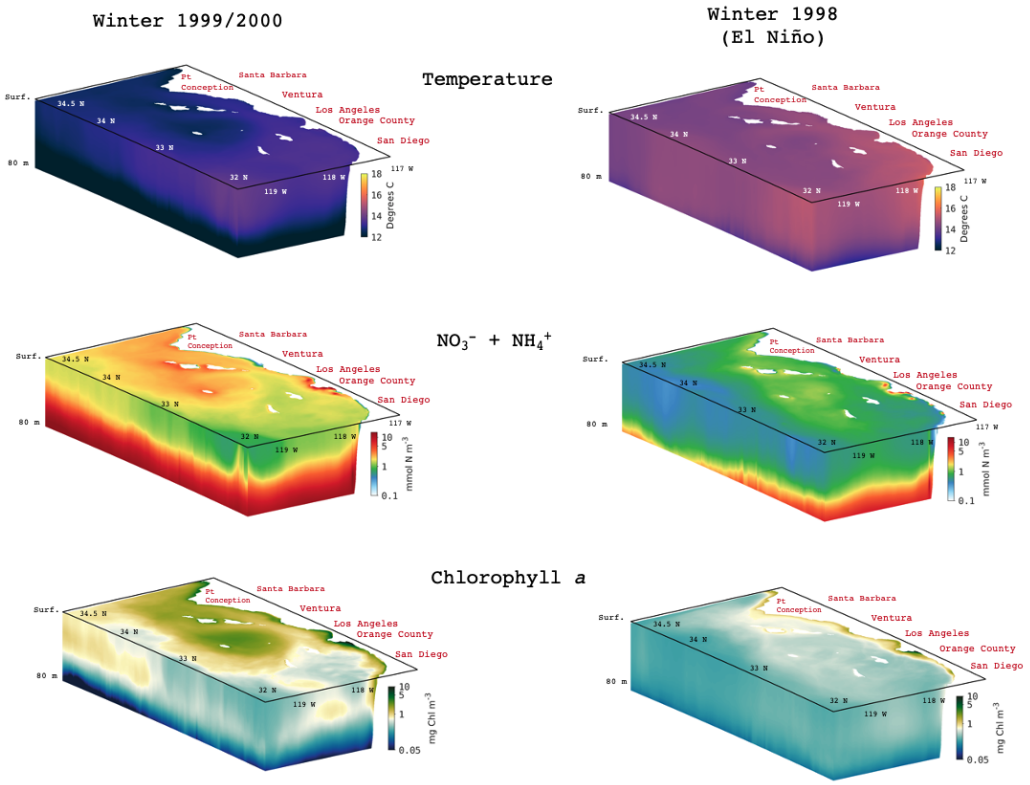

Figure 19: Three-dimensional illustration of temperature, DIN (NO_3^- + NH_4^+) and chlorophyll in the Southern California Bight. Panels show winter 1999 and 2000 (left panels), winter 1998 during El Niño period (right panels).

Arhonditsis, G., Tsirtsis, G., Angelidis, M., & Karydis, M. (2000). Quantification of the effects of nonpoint nutrient sources to coastal marine eutrophication: applications to a semi-enclosed gulf in the mediterranean sea. *Ecological Modelling*, *129*(2-3), 209–227.

Armstrong, R. A., Lee, C., Hedges, J. I., Honjo, S., & Wakeham, S. G. (2001). A new, mechanistic model for organic carbon fluxes in the ocean based on the quantitative association of poc with ballast minerals. *Deep Sea Research Part II: Topical Studies in Oceanography*, *49*(1-3), 219–236.

Bednarsek, N., Feely, R. A., Howes, E. L., Hunt, B., Kessouri, F., León, P., ... others (2019). Systematic review and meta-analysis towards synthesis of thresholds of ocean acidification impacts on calcifying pteropods and interactions with warming. *Frontiers in Marine Science*, *6*, 227.

Behrenfeld, M. J., & Falkowski, P. G. (1997). Photosynthetic rates derived from satellite-based chlorophyll concentration. *Limnology and Oceanography*, *42*(1), 1-20. Retrieved from `https://aslopubs.onlinelibrary.wiley.com/doi/abs/10.4319/lo.1997.42.1.0001` doi: https://doi.org/10.4319/lo.1997.42.1.0001

Beman, J. M., Steele, J. A., & Fuhrman, J. A. (2011). Co-occurrence patterns for abundant marine archaeal and bacterial lineages in the deep chlorophyll maximum of coastal california. *The ISME journal*, *5*(7), 1077–1085.

Boesch, D. F. (2019). Barriers and bridges in abating coastal eutrophication. *Frontiers in Marine Science*, *6*, 123.

Boesch, D. F., Brinsfield, R. B., & Magnien, R. E. (2001). Chesapeake bay eutrophication: Scientific understanding, ecosystem restoration, and challenges for agriculture. *Journal of Environmental Quality*, *30*(2), 303–320.

Bograd, S. J., Buil, M. P., Di Lorenzo, E., Castro, C. G., Schroeder, I. D., Goericke, R., ... Whitney, F. A. (2015). Changes in source waters to the southern california bight. *Deep Sea Research Part II: Topical Studies in Oceanography*, *112*, 42–52.

Booth, J., Woodson, C., Sutula, M., Micheli, F., Weisberg, S., Bograd, S., ... Crowder, L. (2014). Patterns and potential drivers of declining oxygen content along the southern california coast. *Limnology and Oceanography*, *59*(4), 1127–1138.

Brzezinski, M. A., & Washburn, L. (2011). Phytoplankton primary productivity in the santa barbara channel: Effects of wind-driven upwelling and mesoscale eddies. *Journal of Geophysical Research: Oceans*, *116*(C12).

Byun, D. W., Song, C.-K., Percell, P., Pleim, J., Otte, T., Young, J., & Mathur, R. (2006). Linkage between wrf/nmm and cmaq models. In *Presentation at 5th annual cmas conference, chapel hill, nc, available at: www. cmascenter. org* (pp. 16–18).

Capet, X., Campos, E., & Paiva, A. (2008). Submesoscale activity over the Argentinian shelf. *Geophysical Research Letters*, *35*(15).

Capet, X., Colas, F., McWilliams, J. C., Penven, P., & Marchesiello, P. (2008). Eddies in eastern boundary subtropical upwelling systems. *Ocean Modeling in an Eddying Regime, Geophys. Monogr. Ser*, *177*, 131–147.

Capet, X., Klein, P., Hua, B. L., Lapeyre, G., & McWilliams, J. C. (2008). Surface kinetic energy transfer in surface quasi-geostrophic flows. *Journal of Fluid Mechanics*, *604*, 165–174.

Capet, X., Marchesiello, P., & McWilliams, J. (2004). Upwelling response to coastal wind profiles. *Geophysical Research Letters*, *31*(13).

Capet, X., McWilliams, J. C., Molemaker, M. J., & Shchepetkin, A. (2008). Mesoscale to submesoscale transition in the California Current System. Part I: Flow structure, eddy flux, and observational tests. *Journal of Physical Oceanography*, *38*(1), 29–43.

Cederwall, H., & Elmgren, R. (1990). Biological effects of eutrophication in the baltic sea, particularly the coastal zone. *Ambio. Stockholm*, *19*(3), 109–112.

Cerco, C. F., & Cole, T. (1993). Three-dimensional eutrophication model of chesapeake bay. *Journal of Environmental Engineering*, *119*(6), 1006–1025.

Chavez, F., Pennington, J., Castro, C., Ryan, J., Michisaki, R., Schlining, B., ... Collins, C. (2002). Biological and chemical consequences of the 1997–1998 el niño in central california waters. *Progress in Oceanography*, *54*(1-4), 205–232.

Coppola, L., Salvetat, F., Delauney, L., BSH, D. M., Karstensen, J., & Thierry, V. (2013). White paper on dissolved oxygen measurements: scientific needs and sensors accuracy. *Jerico Project*.

Cullen, J. (2001). *Primary production methods.* London, UK: Academic Press.

Dauhajre, D. P., McWilliams, J. C., & Renault, L. (2019). Nearshore lagrangian connectivity: Submesoscale influence and resolution sensitivity. *Journal of Geophysical Research: Oceans*, *124*(7), 5180–5204.

de Boyer Montégut, C., Madec, G., Fischer, A. S., Lazar, A., & Iudicone, D. (2004). Mixed layer depth over the global ocean: An examination of profile data and a profile-based climatology. *Journal of Geophysical Research: Oceans*, *109*(C12).

Derrick, B., Toher, D., & White, P. (2016). Why Welch's test is Type I error robust. *QUANTITATIVE METHODS FOR PSYCHOLOGY*, *12*(1), 30-38. doi: {10.20982/tqmp.12.1.p030}

Deutsch, C. A., Frenzel, H., McWilliams, J. C., Renault, L., Kessouri, F., Howard, E. M., ... Yang, S. (2020). Biogeochemical variability in the california current system. *bioRxiv*.

DiGiacomo, P. M., Washburn, L., Holt, B., & Jones, B. H. (2004). Coastal pollution hazards in southern california observed by sar imagery: stormwater plumes, wastewater plumes, and natural hydrocarbon seeps. *Marine Pollution Bulletin*, *49*(11-12), 1013–1024.

Dong, C., Idica, E. Y., & McWilliams, J. C. (2009). Circulation and multiple-scale variability in the southern california bight. *Progress in Oceanography*, *82*(3), 168–190.

Fasham, M. J. (1993). Modelling the marine biota. In *The global carbon cycle* (pp. 457–504). Springer.

Feely, R. A., Okazaki, R. R., Cai, W.-J., Bednaršek, N., Alin, S. R., Byrne, R. H., & Fassbender, A. (2018). The combined effects of acidification and hypoxia on ph and aragonite saturation in the coastal waters of the california current ecosystem and the northern gulf of mexico. *Continental Shelf Research*, *152*, 50–60.

Fennel, K., & Testa, J. M. (2019). Biogeochemical controls on coastal hypoxia. *Annual Review of Marine Science*, *11*, 105–130.

Galarza, J. A., Carreras-Carbonell, J., Macpherson, E., Pascual, M., Roques, S., Turner, G. F., & Rico, C. (2009). The influence of oceanographic fronts and early-life-history traits on connectivity among littoral fish species. *Proceedings of the National Academy of Sciences*, *106*(5), 1473–1478.

Gruber, N. (2004). The dynamics of the marine nitrogen cycle and its influence on atmospheric co 2 variations. In *The ocean carbon cycle and climate* (pp. 97–148). Springer.

Gruber, N., Lachkar, Z., Frenzel, H., Marchesiello, P., Münnich, M., McWilliams, J. C., ... Plattner, G.-K. (2011). Eddy-induced reduction of biological production in eastern boundary upwelling systems. *Nature geoscience*, *4*(11), 787.

Howard, M. D., Sutula, M., Caron, D. A., Chao, Y., Farrara, J. D., Frenzel, H., ... Sengupta, A. (2014). Anthropogenic nutrient sources rival natural sources on small scales in the coastal waters of the southern california bight. *Limnology and Oceanography*, *59*(1), 285–297.

Juranek, L., Feely, R., Gilbert, D., Freeland, H., & Miller, L. (2011). Real-time estimation of ph and aragonite saturation state from argo profiling floats: Prospects for an autonomous carbon observing strategy. *Geophysical Research Letters*, *38*(17).

Juranek, L., Feely, R., Peterson, W., Alin, S., Hales, B., Lee, K., ... Peterson, J. (2009). A novel method for determination of aragonite saturation state on the continental shelf of central oregon using multi-parameter relationships with hydrographic data. *Geophysical Research Letters*, *36*(24).

Justić, D., Rabalais, N. N., & Turner, R. E. (2005). Coupling between climate variability and coastal eutrophication: evidence and outlook for the northern gulf of mexico. *Journal of Sea Research*, *54*(1), 25–35.

Kahru, M., Kudela, R., Manzano-Sarabia, M., & Mitchell, B. G. (2009). Trends in primary production in the california current detected with satellite data. *Journal of Geophysical Research: Oceans*, *114*(C2).

Kang, X., Zhang, R.-H., & Wang, G. (2017). Effects of different freshwater flux representations in an ocean general circulation model of the tropical pacific. *Science Bulletin*, *62*(5), 345 - 351. Retrieved from `http://www.sciencedirect.com/science/article/pii/S2095927317300932` doi: https://doi.org/10.1016/j.scib.2017.02.002

Kessouri, F., Bianchi, D., Renault, L., McWilliams, J. C., Frenzel, H., & Deutsch, C. A. (2020). Submesoscale currents modulate the seasonal cycle of nutrients and productivity in the california current system. *Global Biogeochemical Cycles*, *34*(10), e2020GB006578.

Kessouri, F., McLaughlin, K., Sutula, M., Ho, M., McWilliams, J., C, & Bianchi, D. (2020, August). *Collection of in situ monitoring data in the Southern California Bight 1950-2017 for model validation.* Zenodo. Retrieved from `https://doi.org/10.5281/zenodo.4536641` doi: 10.5281/zenodo.4536641

Kessouri, F., McWilliams, C. J., Deutsch, C., Renault, L., Frenzel, H., Bianchi, D., & Molemaker, J. (2020, August). *ROMS-BEC oceanic physical and biogeochemical model code for the Southern California Current System V2020.* Zenodo. Retrieved from `https://doi.org/10.5281/zenodo.3988618` doi: 10.5281/zenodo.3988618

Kim, S. Y., Terrill, E. J., Cornuelle, B. D., Jones, B., Washburn, L., Moline, M. A., ... Kosro, P. M. (2011). Mapping the u.s. west coast surface circulation: A multiyear analysis of high-frequency radar observations. *Journal of Geophysical Research: Oceans*, *116*(C3). Retrieved from `https://agupubs.onlinelibrary.wiley.com/doi/abs/10.1029/2010JC006669` doi: https://doi.org/10.1029/2010JC006669

Kudela, R. M., Howard, M. D., Hayashi, K., & Beck, C. (2017). Evaluation of uptake kinetics during a wastewater diversion into nearshore coastal waters in southern california. *Estuarine, Coastal and Shelf Science*, *186*, 237–249.

Landry, M. R., Ohman, M. D., Goericke, R., Stukel, M. R., & Tsyrklevich, K. (2009). Lagrangian studies of phytoplankton growth and grazing relationships in a coastal upwelling ecosystem off southern california. *Progress in Oceanography*, *83*(1-4), 208–216.

Large, W. B. (2006). Surface fluxes for practitioners of global ocean data assimilation. In *Ocean weather forecasting* (pp. 229–270). Springer.

Large, W. G., McWilliams, J. C., & Doney, S. C. (1994). Oceanic vertical mixing: A review and a model with a nonlocal boundary layer parameterization. *Reviews of Geophysics*, *32*(4), 363–403.

Laurent, A., Fennel, K., Ko, D. S., & Lehrter, J. (2018). Climate change projected to exacerbate impacts of coastal eutrophication in the northern gulf of mexico. *Journal of Geophysical Research: Oceans*, *123*(5), 3408–3426.

Leinweber, A., Gruber, N., Frenzel, H., Friederich, G., & Chavez, F. (2009). Diurnal carbon cycling in the surface ocean and lower atmosphere of santa monica bay, california. *Geophysical research letters*, *36*(8).

Lévy, M., Ferrari, R., Franks, P. J., Martin, A. P., & Rivière, P. (2012). Bringing physics to life at the submesoscale. *Geophysical Research Letters*, *39*(14).

Li, Q. P., Franks, P. J., & Landry, M. R. (2011). Microzooplankton grazing dynamics: parameterizing grazing models with dilution experiment data from the california current ecosystem. *Marine Ecology Progress Series*, *438*, 59–69.

Lucas, A. J., Dupont, C. L., Tai, V., Largier, J. L., Palenik, B., & Franks, P. J. (2011). The green ribbon: Multiscale physical control of phytoplankton productivity and community structure over a narrow continental shelf. *Limnology and Oceanography*, *56*(2), 611–626.

Lyon, G. S., & Stein, E. D. (2009). How effective has the clean water act been at reducing pollutant mass emissions to the southern california bight over the past 35 years? *Environmental monitoring and assessment*, *154*(1-4), 413.

Mahadevan, A. (2016). The impact of submesoscale physics on primary productivity of plankton. *Annual Review of Marine Science*, *8*, 161–184.

Mahowald, N. M., Yoshioka, M., Collins, W. D., Conley, A. J., Fillmore, D. W., & Coleman, D. B. (2006). Climate response and radiative forcing from mineral aerosols during the

last glacial maximum, pre-industrial, current and doubled-carbon dioxide climates. *Geophysical Research Letters*, *33*(20).

Mantyla, A. W., Bograd, S. J., & Venrick, E. L. (2008). Patterns and controls of chlorophyll-a and primary productivity cycles in the southern california bight. *Journal of Marine Systems*, *73*(1-2), 48–60.

Marchesiello, P., McWilliams, J. C., & Shchepetkin, A. (2001). Open boundary conditions for long-term integration of regional oceanic models. *Ocean modelling*, *3*(1-2), 1–20.

Marchesiello, P., McWilliams, J. C., & Shchepetkin, A. (2003). Equilibrium structure and dynamics of the california current system. *Journal of physical Oceanography*, *33*(4), 753–783.

Maréchal, D. (2004). A soil-based approach to rainfall-runoff modelling in ungauged catchments for england and wales.

Marmorino, G. O., Smith, G. B., Miller, W. D., & Bowles, J. (2010). Detection of a buoyant coastal wastewater discharge using airborne hyperspectral and infrared imagery. *Journal of Applied Remote Sensing*, *4*(1), 043502.

Mason, E., Molemaker, J., Shchepetkin, A. F., Colas, F., McWilliams, J. C., & Sangrà, P. (2010). Procedures for offline grid nesting in regional ocean models. *Ocean modelling*, *35*(1-2), 1–15.

McClatchie, S. (2016). *Regional fisheries oceanography of the california current system.* Springer.

McGillicuddy Jr, D. J. (2016). Mechanisms of physical-biological-biogeochemical interaction at the oceanic mesoscale.

McLaughlin, K., Dickson, A., Weisberg, S. B., Coale, K., Elrod, V., Hunter, C., ... others (2017). An evaluation of isfet sensors for coastal ph monitoring applications. *Regional Studies in Marine Science*, *12*, 11–18.

McLaughlin, K., Meredith, H., Robertson, G., Beck, C., Ho, M., Kessouri, F., ... Weisberg, S. (2021). Influence of anthropogenic nutrient inputs on rates of coastal ocean nitrogen and carbon cycling in the southern california bight, usa. *Earth and Space Science Open Archive (ESSOAr)*.

McLaughlin, K., Nezlin, N. P., Howard, M. D., Beck, C. D., Kudela, R. M., Mengel, M. J., & Robertson, G. L. (2017). Rapid nitrification of wastewater ammonium near coastal ocean outfalls, southern california, usa. *Estuarine, Coastal and Shelf Science*, *186*, 263–275.

McLaughlin, K., Nezlin, N. P., Weisberg, S. B., Dickson, A. G., Booth, J. A. T., Cash, C. L., ... others (2018). Seasonal patterns in aragonite saturation state on the southern california continental shelf. *Continental Shelf Research*, *167*, 77–86.

McWilliams, J. C. (2007). Irreducible imprecision in atmospheric and oceanic simulations. *Proceedings of the National Academy of Sciences*, *104*(21), 8709–8713.

McWilliams, J. C. (2016). Submesoscale currents in the ocean. *Proceedings of the Royal Society A: Mathematical, Physical and Engineering Sciences*, *472*(2189), 20160117.

Middelburg, J. J., Soetaert, K., Herman, P. M., & Heip, C. H. (1996). Denitrification in marine sediments: A model study. *Global Biogeochemical Cycles*, *10*(4), 661–673.

Moll, A., & Radach, G. (2003). Review of three-dimensional ecological modelling related to the north sea shelf system: Part 1: models and their results. *Progress in Oceanography*, *57*(2), 175–217.

Moore, J. K., Doney, S. C., & Lindsay, K. (2004). Upper ocean ecosystem dynamics and iron cycling in a global three-dimensional model. *Global Biogeochemical Cycles*, *18*(4).

Nagai, T., Gruber, N., Frenzel, H., Lachkar, Z., McWilliams, J. C., & Plattner, G.-K. (2015). Dominant role of eddies and filaments in the offshore transport of carbon and nutrients in the California Current System. *Journal of Geophysical Research: Oceans*, *120*(8), 5318–5341.

Nash, J., & Sutcliffe, J. (1970). River flow forecasting through conceptual models part i — a discussion of principles. *Journal of Hydrology*, *10*(3), 282 - 290. Retrieved from `http://www.sciencedirect.com/science/article/pii/0022169470902556` doi: https://doi.org/10.1016/0022-1694(70)90255-6

Nezlin, N. P., McLaughlin, K., Booth, J. A. T., Cash, C. L., Diehl, D. W., Davis, K. A., ... others (2018). Spatial and temporal patterns of chlorophyll concentration in the southern california bight. *Journal of Geophysical Research: Oceans*, *123*(1), 231–245.

Nezlin, N. P., Sutula, M. A., Stumpf, R. P., & Sengupta, A. (2012). Phytoplankton blooms detected by seawifs along the central and southern california coast. *Journal of Geophysical Research: Oceans*, *117*(C7).

Ocean Protection Council. (2018). *State of california ocean acidification action plan.* Retrieved from `https://www.opc.ca.gov/oa-action-plan/`

Regaudie-de Gioux, A., Lasternas, S., Agustí, S., & Duarte, C. M. (2014). Comparing marine primary production estimates through different methods and development of conversion equations. *Frontiers in Marine Science*, *1*, 19.

Renault, L., Hall, A., & McWilliams, J. C. (2016a). Orographic shaping of U.S. West Coast Wind Profiles During the Upwelling Season. *Climate Dynamics*, 1–17.

Renault, L., Hall, A., & McWilliams, J. C. (2016b). Orographic shaping of us west coast wind profiles during the upwelling season. *Climate Dynamics*, *46*(1-2), 273–289.

Renault, L., Masson, S., Arsouze, T., Madec, G., & McWilliams, J. C. (2020). Recipes for how to force oceanic model dynamics. *Journal of Advances in Modeling Earth Systems*, *12*(2), e2019MS001715.

Renault, L., McWilliams, J. C., Jousse, A., Deutsch, C., Frenzel, H., Kessouri, F., & Chen, R. (2020). The physical structure and behavior of the california current system. *bioRxiv*.

Renault, L., Molemaker, M. J., Gula, J., Masson, S., & McWilliams, J. C. (2016). Control and stabilization of the gulf stream by oceanic current interaction with the atmosphere. *Journal of Physical Oceanography*, *46*(11), 3439–3453.

Renault, L., Molemaker, M. J., McWilliams, J. C., Shchepetkin, A. F., Lemarié, F., Chelton, D., ... Hall, A. (2016). Modulation of wind work by oceanic current interaction with the atmosphere. *Journal of Physical Oceanography*, *46*(6), 1685–1704.

Sailley, S., Vogt, M., Doney, S., Aita, M., Bopp, L., Buitenhuis, E., ... Yamanaka, Y. (2013). Comparing food web structures and dynamics across a suite of global marine ecosystem models. *Ecological Modelling*, *261*, 43–57.

Savchuk, O. P., & Wulff, F. (2007). Modeling the baltic sea eutrophication in a decision support system. *AMBIO: A Journal of the Human Environment*, *36*(2), 141–148.

Seegers, B. N., Birch, J. M., Marin III, R., Scholin, C. A., Caron, D. A., Seubert, E. L., ... Jones, B. H. (2015). Subsurface seeding of surface harmful algal blooms observed through the integration of autonomous gliders, moored environmental sample processors, and satellite remote sensing in southern c alifornia. *Limnology and Oceanography*, *60*(3), 754–764.

Severmann, S., McManus, J., Berelson, W. M., & Hammond, D. E. (2010). The continental shelf benthic iron flux and its isotope composition. *Geochimica et Cosmochimica Acta*, *74*(14), 3984–4004.

Shchepetkin, A. F., & McWilliams, J. C. (2005). The regional oceanic modeling system (roms): a split-explicit, free-surface, topography-following-coordinate oceanic model. *Ocean modelling*, *9*(4), 347–404.

Shchepetkin, A. F., & McWilliams, J. C. (2009). Correction and commentary for "Ocean forecasting in terrain-following coordinates: Formulation and skill assessment of the regional ocean modeling system" by Haidvogel et al., J. Comp. Phys. 227, pp. 3595–3624. *Journal of Computational Physics*, *228*(24), 8985–9000.

Shchepetkin, A. F., & McWilliams, J. C. (2011). Accurate boussinesq oceanic modeling with a practical,"stiffened" equation of state. *Ocean Modelling*, *38*(1-2), 41–70.

Skamarock, W. C., & Klemp, J. B. (2008). A time-split nonhydrostatic atmospheric model for weather research and forecasting applications. *Journal of Computational Physics*, *227*(7), 3465–3485.

Sutton, A., Wanninkhof, R., Sabine, C., Feely, R., Cronin, M., & Weller, R. (2017). Variability and trends in surface seawater pco2 and co2 flux in the pacific ocean. *Geophysical Research Letters*, *44*(11), 5627–5636.

Sutula, M., Ho, M., Sengupta, A., Kessouri, F., McLaughlin, K., McCune, K., & Bianchi, D. (2021a, January). *A Baseline of Terrestrial Freshwater and Nitrogen Fluxes to the Southern California Bight, USA.* Zenodo. Retrieved from `https://doi.org/10.5281/zenodo.4448224` doi: 10.5281/zenodo.4448224

Sutula, M., Ho, M., Sengupta, A., Kessouri, F., McLaughlin, K., McCune, K., & Bianchi, D. (2021b). Dataset of terrestrial fluxes of freshwater, nutrients, carbon, and iron to the southern california bight, u.s.a. *Data in Brief*, 106802. Retrieved from `https://www.sciencedirect.com/science/article/pii/S235234092100086X` doi: https://doi.org/10.1016/j.dib.2021.106802

Taylor, B. L., Wade, P. R., De Master, D. P., & Barlow, J. (2000). Incorporating uncertainty into management models for marine mammals. *Conservation Biology*, *14*(5), 1243–1252.

Teel, E. N., Liu, X., Seegers, B. N., Ragan, M. A., Haskell, W. Z., Jones, B., & Levine, N. M. (2018). Contextualizing time-series data: quantification of short-term regional variability in the san pedro channel using high-resolution in situ glider data.

Todd, R. E., Rudnick, D. L., Davis, R. E., & Ohman, M. D. (2011). Underwater gliders reveal rapid arrival of el niño effects off california's coast. *Geophysical Research Letters*, *38*(3).

Uchiyama, Y., Idica, E. Y., McWilliams, J. C., & Stolzenbach, K. D. (2014). Wastewater effluent dispersal in southern california bays. *Continental Shelf Research*, *76*, 36–52.

Wanninkhof, R. (1992). Relationship between wind speed and gas exchange over the ocean. *Journal of Geophysical Research: Oceans*, *97*(C5), 7373–7382.

Warrick, J. A., DiGiacomo, P. M., Weisberg, S. B., Nezlin, N. P., Mengel, M., Jones, B. H., ... Farnsworth, K. L. (2007). River plume patterns and dynamics within the southern california bight. *Continental Shelf Research*, *27*(19), 2427–2448.

Weisberg, S. B., Bednaršek, N., Feely, R. A., Chan, F., Boehm, A. B., Sutula, M., ... Newton, J. A. (2016). Water quality criteria for an acidifying ocean: Challenges and opportunities for improvement. *Ocean & Coastal Management*, *126*, 31–41.

Welch, B. L. (1947, 01). THE GENERALIZATION OF 'STUDENT'S' PROBLEM WHEN SEVERAL DIFFERENT POPULATION VARLANCES ARE INVOLVED. *Biometrika*, *34*(1-2), 28-35. Retrieved from `https://doi.org/10.1093/biomet/34.1-2.28` doi: 10.1093/biomet/34.1-2.28

Winant, C., Dever, E. P., & Hendershott, M. (2003). Characteristic patterns of shelf circulation at the boundary between central and southern california. *Journal of Geophysical Research: Oceans*, *108*(C2).

Woodson, C. B., & Litvin, S. Y. (2015). Ocean fronts drive marine fishery production and biogeochemical cycling. *Proceedings of the National Academy of Sciences*, *112*(6), 1710–1715.

Zheng, G., & DiGiacomo, P. M. (2017). Uncertainties and applications of satellite-derived coastal water quality products. *Progress in oceanography*, *159*, 45–72.

Supporting Information for "Configuration and validation of an oceanic physical and biogeochemical model to investigate coastal eutrophication in the Southern California Bight"

Contents of this file

1. Tables S1 to S4
2. Figures S1 to S24

- Table S1: Statistical comparison of vertical profiles of temperature, dissolved oxygen, chlorophyll *a*, pH, and ammonium concentration at Ventura/Oxnard (City of Oxnard stations) monitoring region. Letters next to numbers indicate model performance: E = Excellent, G = very good, R = reasonable, P = Poor.
- Table S2: Same as Table S1 for Palos Verdes (LACSD stations) monitoring region.
- Table S3: Same as Table S1 for Orange County (OCSD stations) monitoring region.
- Table S4: Same as Table S1 for San Diego (City of San Diego stations) monitoring region.
- Figure S1: Spatial distribution of the point sources to simulate and to dilute the freshwater, nutrients and organic matter fluxes for the 4 majors POTW underwater outfalls locations. Color contours show bathymetry. Vertically integrated, the grid cells with the red dots discharge 4/9 of the respective flow at each diffuser, the grid cells with yellow dots north, south, east and west of the red dots discharge 1/9 of the discharge, and the yellow dots in the corners discharge 1/36 of the volume flux.
- Figure S2:Seasonal profiles of average temperature off of Palos Verdes. The red line andred bars are the spatial and temporal means and the variability from the model. The blackdots and the gray shade are the spatial and temporal mean and the variability fromin situdata (LACSD stations). These profiles are showing agreement on intensity, seasonality andshape of the vertical profile with exceptionally high concentrations at mid-depth.
- Figure S3:Same as Fig S2 for Oxnard/Ventura using City of Oxnard stations
- Figure S4:Same as Fig S2 for Orange County using OCSD stations
- Figure S5: Same as Fig S2 for San Diego using City of San Diego stations.
- Figure S6:Seasonal profiles of average ammonium concentration off of Palos Verdes. Thered line and red bars are the spatial and temporal means and the variability from the model.The black dots and the gray shade are the spatial and temporal mean and the variabilityfromin situdata (LACSD stations). These profiles are showing agreement on intensity,seasonality and shape of the vertical profile with exceptionally high concentrations at mid-depth.
- Figure S7:Same as Fig S6 for Oxnard/Ventura using City of Oxnard stations
- Figure S8:Same as Fig S6 for Orange County using OCSD stations.
- Figure S9:Same as Fig S6 for San Diego using City of San Diego stations.In situdataare missing but we wanted to report out the depth of maximum anthropogenic plume, incontrary to other subregion, in San Diego area, the plume rarely reaches 20 m.
- Figure S10:easonal profiles of average chlorophyllaconcentration off of Palos Verdes.The red line and red bars are the spatial and temporal means and the variability from themodel. The black dots and the gray shade are the spatial and temporal mean and thevariability fromin situdata (LACSD stations). These profiles are showing agreement onintensity, seasonality and shape of the vertical profile with exceptionally high concentrationsat mid-depth
- Figure S11:Same as Fig S10 for Oxnard/Ventura using City of Oxnard stations
- Figure S12:Same as Fig S10 for Orange County using OCSD stations

- Figure S13:Same as Fig S10 for San Diego using City of San Diego stations
- Figure S14:Seasonal profiles of average dissolved oxygen concentration off of Palos Verdes.The red line and red bars are the spatial and temporal means and the variability from themodel. The black dots and the gray shade are the spatial and temporal mean and thevariability fromin situdata (LACSD stations). These profiles are showing agreement onintensity, seasonality and shape of the vertical profile with exceptionally high concentrationsat mid-depth
- Figure S15:Same as Fig S14 for Oxnard/Ventura using City of Oxnard stations.
- Figure S16:Same as Fig S14 for Orange County using OCSD stations
- Figure S17:Same as Fig S14 for San Diego using City of San Diego stations.
- Figure S18:Seasonal profiles of average pH (seawater scale) off of Palos Verdes. The red lineand red bars are the spatial and temporal means and the variability from the model. Theblack dots and the gray shade are the spatial and temporal mean and the variability frominsitudata (LACSD stations). These profiles are showing agreement on intensity, seasonalityand shape of the vertical profile with exceptionally high concentrations at mid-depth.
- Figure S19:Same as Fig S18 for Oxnard/Ventura using City of Oxnard stations.
- Figure S20:Same as Fig S18 for Orange County using OCSD stations.
- Figure S21:Same as Fig S18 for San Diego using City of San Diego stations.
- Figure S22:Average nitrification rate in Santa Monica and San Pedro bays. This figureshows the high rates around the locations of the outfalls that results from the release of highconcentrations of ammonium below the thermocline
- Figure S23:(upper panel) Hovmöller of ammonium concentration at San Pedro Oceanic Time-series(SPOT) located mid-distance between Los Angeles coast and Catalina Island. (lower panel) idem as(b) for chlorophyllaconcentration. The Hovmöllers show 1) ammonium concentration offLos Angeles coast are not affected by anthropogenic loads. 2) Deep chlorophyllamaximumis trapped below at subsurface for 70
- Figure S24:Summer time 1997-2000 average carbon export at 40 m in the SCB. The mapshows hot-spots of intense carbon export in Santa Barbara and Los Angeles coasts.

Ventura/Oxnard								
Temperature								
	H	Correlation Coefficient	p-value	Cost Function	Percentage Bias	Ratio of Standard Deviations	Nash-Sutcliffe Model Efficiency	Number of observations
Winter	0 E	0.95 E	2E-05 E	0.06 E	-0.04 E	1.11 G	0.77 E	469
Spring	0 E	0.98 E	7E-07 E	0.09 E	-0.09 E	0.80 G	0.59 G	468
Summer	0 E	0.98 E	1E-06 E	0.04 E	-0.02 E	1.08 E	0.94 E	468
Fall	0 E	0.89 G	5E-04 E	0.09 E	-0.08 E	0.97 E	0.50 R	469
All Seasons	0 E	0.95 E	3E-05 E	0.08 E	-0.06 E	1.03 E	0.74 E	1874
Oxygen								
	H	Correlation Coefficient	p-value	Cost Function	Percentage Bias	Ratio of Standard Deviations	Nash-Sutcliffe Model Efficiency	Number of observations
Winter	0 E	0.98 E	1E-06 E	0.14 E	-0.09 E	1.20 R	0.77 E	469
Spring	0 E	0.92 E	1E-04 E	0.25 E	-0.21 R	1.06 E	0.47 R	454
Summer	0 E	0.99 E	1E-09 E	0.07 E	0.08 E	1.03 E	0.84 E	468
Fall	0 E	0.98 E	1E-06 E	0.19 E	-0.14 G	1.52 P	0.44 R	469
All Seasons	0 E	0.98 E	1E-06 E	0.14 E	-0.010 G	1.20 R	0.73 E	1860
Chlorophyll-a								
	H	Correlation Coefficient	p-value	Cost Function	Percentage Bias	Ratio of Standard Deviations	Nash-Sutcliffe Model Efficiency	Number of observations
Winter	0 E	0.99 E	1E-08 E	0.43 E	-0.06 E	0.90 E	0.96 E	469
Spring	0 E	0.97 E	3E-06 E	0.86 E	-0.42 P	0.51 P	-0.47 P	468
Summer	0 E	0.96 E	1E-05 E	0.59 E	-0.04 E	0.64 R	0.51 G	468
Fall	0 E	0.94 E	5E-05 E	0.53 E	0.20 R	0.71 R	0.50 R	469
All Seasons	0 E	0.99 E	9E-11 E	0.50 E	-0.01 E	0.71 R	0.79 E	1874
pH								
	H	Correlation Coefficient	p-value	Cost Function	Percentage Bias	Ratio of Standard Deviations	Nash-Sutcliffe Model Efficiency	Number of observations
Winter	0 E	0.99 E	2E-08 E	0.01 E	0.01 E	0.62 R	0.57 G	455
Spring	0 E	0.97 E	2E-07 E	0.01 E	-0.01 E	1.45 P	0.25 R	454
Summer	0 E	0.97 E	2E-06 E	0.01 E	0.01 E	1.06 E	0.84 E	468
Fall	0 E	0.98 E	6E-07 E	0.01 E	0.01 E	1.43 P	0.75 E	467
All Seasons	0 E	0.98 E	1E-06 E	0.01 E	-0.01 E	1.13 G	0.89 E	1844
Ammonia								
	H	Correlation Coefficient	p-value	Cost Function	Percentage Bias	Ratio of Standard Deviations	Nash-Sutcliffe Model Efficiency	Number of observations
Winter	0 E	0.86 G	0.34 P	0.53 E	0.24 R	1.56 P	0.58 G	11
Spring	0 E	0.99 E	0.02 E	1.40 G	-1.87 P	0.36 P	-10.52 P	12
Summer	0 E	0.92 E	0.25 P	2.59 R	0.28 R	1.62 P	0.67 E	12
Fall	0 E	0.92 E	0.26 P	4.42 P	-2.77 P	0.35 P	-10.48 P	12
All Seasons	0 E	0.89 G	0.04 E	0.77 E	-0.49 P	0.91 E	0.01 P	47

Table S1: Statistical comparison of vertical profiles of temperature, dissolved oxygen, chlorophyll *a*, pH, and ammonium concentration at Ventura/Oxnard (City of Oxnard stations) monitoring region. Letters next to numbers indicate model performance: E = Excellent, G = very good, R = reasonable, P = Poor.

Palos Verdes								
Temperature								
	H	Correlation Coefficient	p-value	Cost Function	Percentage Bias	Ratio of Standard Deviations	Nash-Sutcliffe Model Efficiency	Number of observations
Winter	0 E	0.95 E	2E-05 E	0.04 E	-0.01 E	1.13 G	0.87 E	469
Spring	0 E	0.94 E	6E-05 E	0.24 E	-0.11 G	0.75 R	0.19 P	466
Summer	0 E	0.98 E	7E-07 E	0.03 E	0.03 E	1.19 G	0.91 E	466
Fall	0 E	0.88 G	7E-04 E	0.11 E	-0.11 G	0.75 R	-0.27 P	468
All Seasons	0 E	0.94 E	5E-05 E	0.07 E	-0.06 E	0.98 E	0.74 E	1869
Oxygen								
	H	Correlation Coefficient	p-value	Cost Function	Percentage Bias	Ratio of Standard Deviations	Nash-Sutcliffe Model Efficiency	Number of observations
Winter	0 E	0.99 E	9E-09 E	0.03 E	0.02 E	1.05 E	0.94 E	469
Spring	0 E	0.83 G	3E-03 E	0.24 E	-0.22 R	0.87 G	0.01 P	466
Summer	0 E	0.97 E	2E-06 E	0.08 E	0.08 E	0.87 G	0.69 E	466
Fall	0 E	0.97 E	7E-04 E	0.08 E	-0.06 E	1.14 G	0.76 E	467
All Seasons	0 E	0.98 E	1E-06 E	0.06 E	-0.05 E	0.97 E	0.88 E	1868
Chlorophyll-a								
	H	Correlation Coefficient	p-value	Cost Function	Percentage Bias	Ratio of Standard Deviations	Nash-Sutcliffe Model Efficiency	Number of observations
Winter	0 E	0.75 R	0.01 E	0.70 E	0.25 R	0.83 G	0.19 P	469
Spring	0 E	0.83 G	2E-03 E	0.72 E	0.06 E	1.01 E	0.65 E	466
Summer	0 E	0.67 R	0.04 E	0.73 E	0.38 R	1.28 R	0.17 P	466
Fall	0 E	0.99 E	1E-10 E	0.48 E	0.25 R	1.01 E	0.91 E	468
All Seasons	0 E	0.95 E	2E-05 E	0.55 E	0.30 R	1.00 E	0.70 E	1869
pH								
	H	Correlation Coefficient	p-value	Cost Function	Percentage Bias	Ratio of Standard Deviations	Nash-Sutcliffe Model Efficiency	Number of observations
Winter	1 P	0.99 E	2E-07 E	0.03 E	-0.03 E	1.36 R	-2.96 P	469
Spring	0 E	0.84 G	2E-03 E	0.01 E	0.01 E	1.44 P	0.67 E	466
Summer	1 P	0.99 E	2E-09 E	0.03 E	0.03 E	1.62 P	-2.80 P	466
Fall	1 P	0.96 E	9E-06 E	0.02 E	0.02 E	1.54 P	-1.29 P	468
All Seasons	0 E	0.96 E	1E-05 E	0.01 E	0.01 E	1.50 P	0.73 E	1869
Ammonia								
	H	Correlation Coefficient	p-value	Cost Function	Percentage Bias	Ratio of Standard Deviations	Nash-Sutcliffe Model Efficiency	Number of observations
Winter	N/A	N/A	N/A	N/A	N/A	N/A	N/A	0
Spring	N/A	N/A	N/A	N/A	N/A	N/A	N/A	0
Summer	0 E	0.82 G	0.18 P	0.31 E	0.15 G	1.05 E	0.53 G	18
Fall	0 E	0.79 R	0.21 P	0.30 E	0.32 R	1.38 R	-0.15 P	18
All Seasons	0 E	0.84 G	0.16 P	0.30 E	0.32 R	1.34 R	-0.01 P	36

Table S2: Same as Table S1 for Palos Verdes (LACSD stations) monitoring region.

Orange County								
Temperature								
	H	Correlation Coefficient	p-value	Cost Function	Percentage Bias	Ratio of Standard Deviations	Nash-Sutcliffe Model Efficiency	Number of observations
Winter	0 E	0.96 E	1E-05 E	0.05 E	-0.01 E	1.27 R	0.84 E	160
Spring	0 E	0.95 E	3E-05 E	0.11 E	-0.11 G	0.81 G	0.44 R	533
Summer	0 E	0.99 E	2E-08 E	0.02 E	-0.01 E	0.96 E	0.98 E	533
Fall	0 E	0.92 E	2E-04 E	0.08 E	-0.07 E	1.06 E	0.66 E	536
All Seasons	0 E	0.95 E	3E-05 E	0.07 E	-0.05 E	1.07 E	0.79 E	1762
Oxygen								
	H	Correlation Coefficient	p-value	Cost Function	Percentage Bias	Ratio of Standard Deviations	Nash-Sutcliffe Model Efficiency	Number of observations
Winter	0 E	0.98 E	1E-06 E	0.14 E	-0.12 G	1.03 E	0.67 E	150
Spring	0 E	0.90 E	4E-04 E	0.19 E	-0.16 G	0.96 E	0.51 G	533
Summer	0 E	0.99 E	5E-08 E	0.07 E	0.07 E	0.91 E	0.80 E	534
Fall	0 E	0.92 E	4E-07 E	0.09 E	-0.02 E	1.06 E	0.80 E	536
All Seasons	0 E	0.95 E	9E-06 E	0.09 E	-0.06 E	1.07 E	0.81 E	1753
Chlorophyll-a								
	H	Correlation Coefficient	p-value	Cost Function	Percentage Bias	Ratio of Standard Deviations	Nash-Sutcliffe Model Efficiency	Number of observations
Winter	0 E	0.98 E	8E-07 E	0.97 E	0.53 P	2.25 P	0.49 R	160
Spring	0 E	0.74 R	0.02 E	2.24 R	0.29 R	2.12 P	0.46 R	533
Summer	0 E	0.94 E	7E-05 E	0.57 E	-0.16 G	0.83 G	0.76 E	535
Fall	0 E	0.92 E	1E-04 E	0.55 E	0.41 P	1.32 R	0.62 G	536
All Seasons	0 E	0.91 E	3E-04 E	0.47 E	0.33 R	1.80 P	0.63 G	1764
pH								
	H	Correlation Coefficient	p-value	Cost Function	Percentage Bias	Ratio of Standard Deviations	Nash-Sutcliffe Model Efficiency	Number of observations
Winter	0 E	0.98 E	1E-06 E	0.01 E	0 E	1.26 R	0.88 E	160
Spring	0 E	0.79 R	0.01 E	0.01 E	-0.01 E	1.32 R	0.28 R	533
Summer	1 P	0.96 E	2E-05 E	0.02 E	0.02 E	1.32 R	-1.13 P	534
Fall	1 P	0.98 E	1E-06 E	0.03 E	-0.03 E	2.02 P	-2.62 P	536
All Seasons	0 E	0.93 E	9E-05 E	0.01 E	-0.01 E	1.43 P	0.51 G	1763
Ammonia								
	H	Correlation Coefficient	p-value	Cost Function	Percentage Bias	Ratio of Standard Deviations	Nash-Sutcliffe Model Efficiency	Number of observations
Winter	N/A	N/A	N/A	N/A	N/A	N/A	N/A	0
Spring	N/A	N/A	N/A	N/A	N/A	N/A	N/A	0
Summer	1 P	0.97 E	0.14 P	0.86 E	0.83 P	3.89 P	-2.38 P	48
Fall	0 E	0.71 R	0.50 P	0.43 E	0.37 R	0.44 P	-8.71 P	48
All Seasons	1 P	0.76 R	0.14 P	0.62 E	0.63 P	2.36 P	-1.67 P	96

Table S3: Same as Table S1 for Orange County (OCSD stations) monitoring region.

San Diego								
Temperature								
	H	Correlation Coefficient	p-value	Cost Function	Percentage Bias	Ratio of Standard Deviations	Nash-Sutcliffe Model Efficiency	Number of observations
Winter	0 E	0.98 E	3E-08 E	0.02 E	-0.01 E	0.92 E	0.95 E	875
Spring	0 E	0.93 E	1E-05 E	0.09 E	-0.09 E	0.77 R	0.30 R	870
Summer	0 E	0.98 E	5E-08 E	0.04 E	-0.01 E	0.99 E	0.94 E	872
Fall	0 E	0.92 E	3E-05 E	0.08 E	-0.08 E	0.79 R	0.29 R	752
All Seasons	0 E	0.98 E	4E-07 E	0.05 E	-0.05 E	0.83 G	0.70 E	3369
Oxygen								
	H	Correlation Coefficient	p-value	Cost Function	Percentage Bias	Ratio of Standard Deviations	Nash-Sutcliffe Model Efficiency	Number of observations
Winter	0 E	0.96 E	1E-06 E	0.11 E	-0.09 E	1.05 E	0.74 E	875
Spring	1 P	0.87 G	3E-04 E	0.33 E	-0.32 R	0.87 G	-0.45 P	870
Summer	0 E	0.99 E	5E-12 E	0.27 E	-0.20 R	1.47 P	0.51 G	872
Fall	0 E	0.92 E	3E-05 E	0.22 E	-0.16 G	1.59 P	0.37 R	752
All Seasons	0 E	0.97 E	4E-07 E	0.18 E	-0.16 G	1.18 G	0.55 G	3369
Chlorophyll-a								
	H	Correlation Coefficient	p-value	Cost Function	Percentage Bias	Ratio of Standard Deviations	Nash-Sutcliffe Model Efficiency	Number of observations
Winter	0 E	0.99 E	6E-09 E	0.51 E	0.60 P	2.59 P	0.39 R	868
Spring	0 E	0.94 E	4E-06 E	0.84 E	0.36 R	1.59 P	0.73 E	866
Summer	0 E	0.99 E	6E-09 E	0.27 E	0.18 G	1.28 R	0.90 E	870
Fall	0 E	0.89 G	2E-04 E	0.35 E	0.43 P	2.05 P	0.50 R	728
All Seasons	0 E	0.98 E	9E-09 E	0.57 E	0.39 R	1.66 P	0.70 E	3332
pH								
	H	Correlation Coefficient	p-value	Cost Function	Percentage Bias	Ratio of Standard Deviations	Nash-Sutcliffe Model Efficiency	Number of observations
Winter	0 E	0.99 E	5E-09 E	0.01 E	-0.01 E	1.07 E	0.49 R	875
Spring	1 P	0.91 E	5E-05 E	0.02 E	-0.02 E	1.41 P	-0.96 P	872
Summer	1 P	0.99 E	1E-09 E	0.02 E	-0.02 E	2.32 P	-0.07 P	844
Fall	1 P	0.98 E	2E-04 E	0.01 E	-0.01 E	1.77 P	-0.14 P	752
All Seasons	1 P	0.98 E	6E-08 E	0.02 E	-0.02 E	1.59 P	-0.18 P	3343
Ammonia								
	H	Correlation Coefficient	p-value	Cost Function	Percentage Bias	Ratio of Standard Deviations	Nash-Sutcliffe Model Efficiency	Number of observations
Winter	N/A	N/A	N/A	N/A	N/A	N/A	N/A	0
Spring	N/A	N/A	N/A	N/A	N/A	N/A	N/A	0
Summer	N/A	N/A	N/A	N/A	N/A	N/A	N/A	0
Fall	N/A	N/A	N/A	N/A	N/A	N/A	N/A	0
All Seasons	N/A	N/A	N/A	N/A	N/A	N/A	N/A	0

Table S4: Same as Table S1 for San Diego (City of San Diego stations) monitoring region.

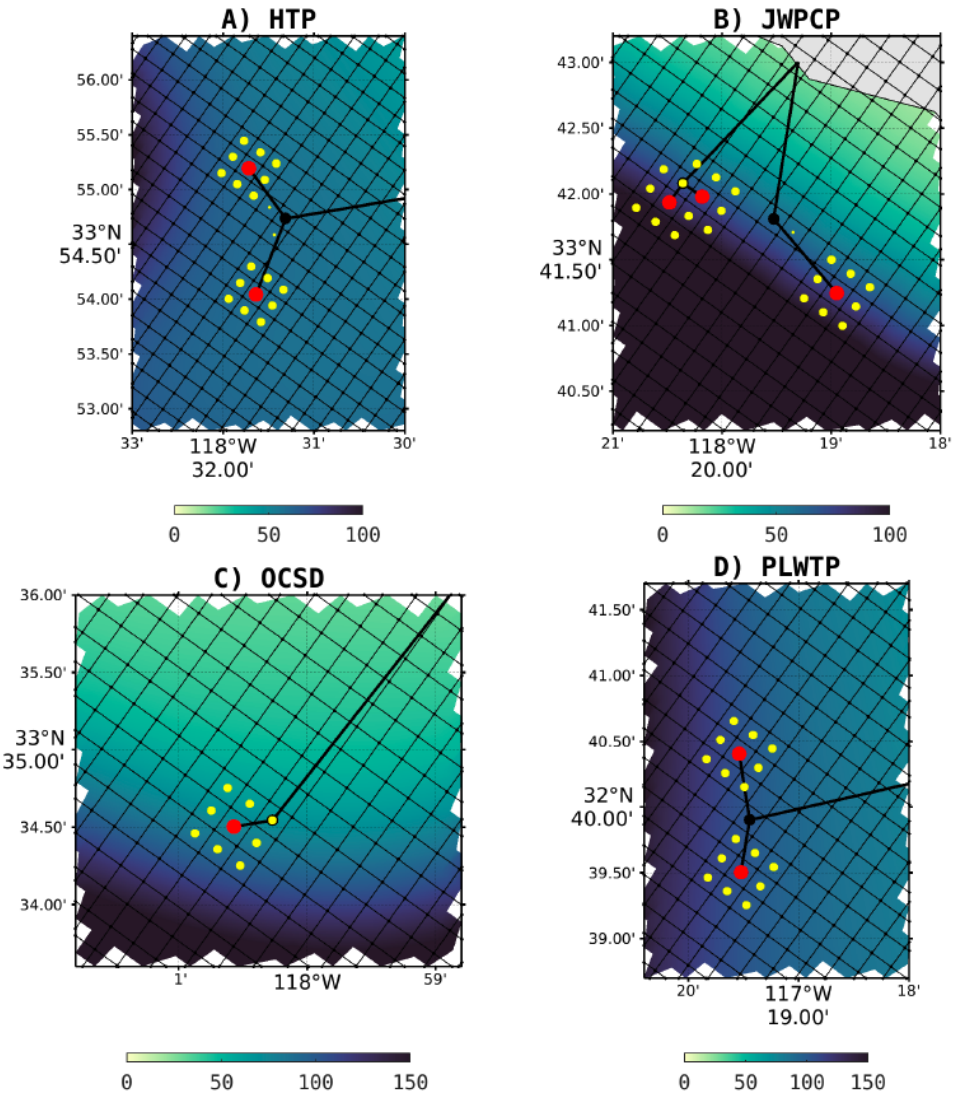

Figure S1: Spatial distribution of the point sources to simulate and to dilute the freshwater, nutrients and organic matter fluxes for the 4 majors POTW underwater outfalls locations. Color scale is bathymetry. Vertically integrated, the grid cells with the red dots discharge 4/9 of the respective flow at each diffuser, the grid cells with yellow dots north, south, east and west of the red dots discharge 1/9 of the discharge, and the yellow dots in the corners discharge 1/36 of the volume flux.

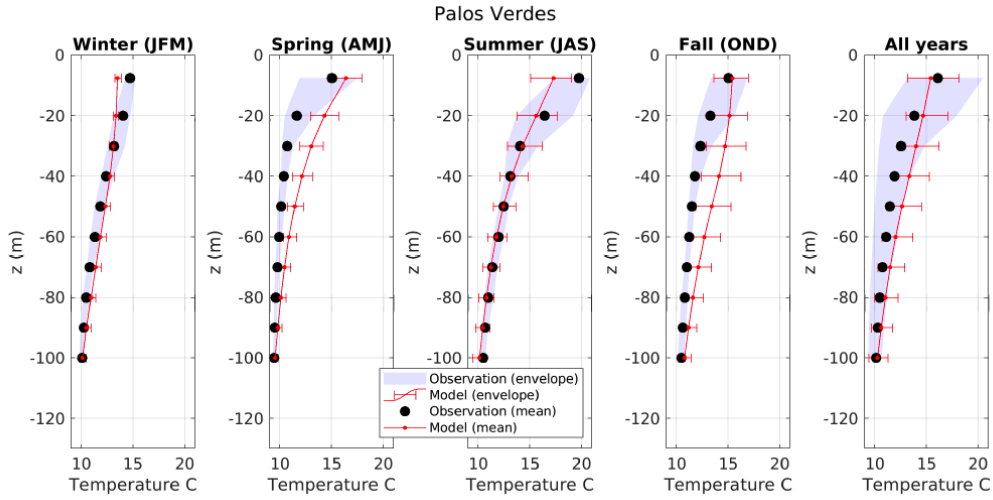

Figure S2: Seasonal profiles of average temperature off of Palos Verdes. The red line and red bars are the spatial and temporal means and the variability from the model. The black dots and the gray shade are the spatial and temporal mean and the variability from *in situ* data (LACSD stations). These profiles are showing agreement on intensity, seasonality and shape of the vertical profile with exceptionally high concentrations at mid-depth.

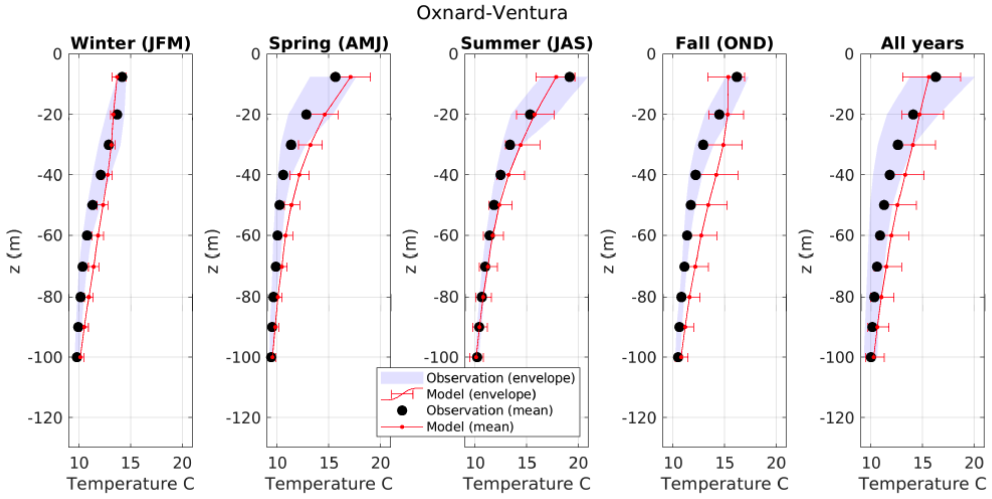

Figure S3: Same as Fig S2 for Oxnard/Ventura using City of Oxnard stations.

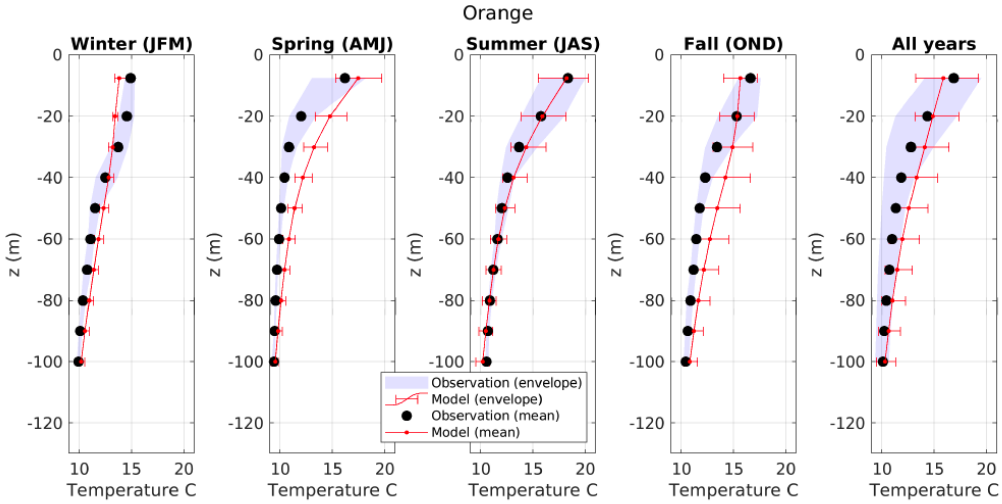

Figure S4: Same as Fig S2 for Orange County using OCSD stations.

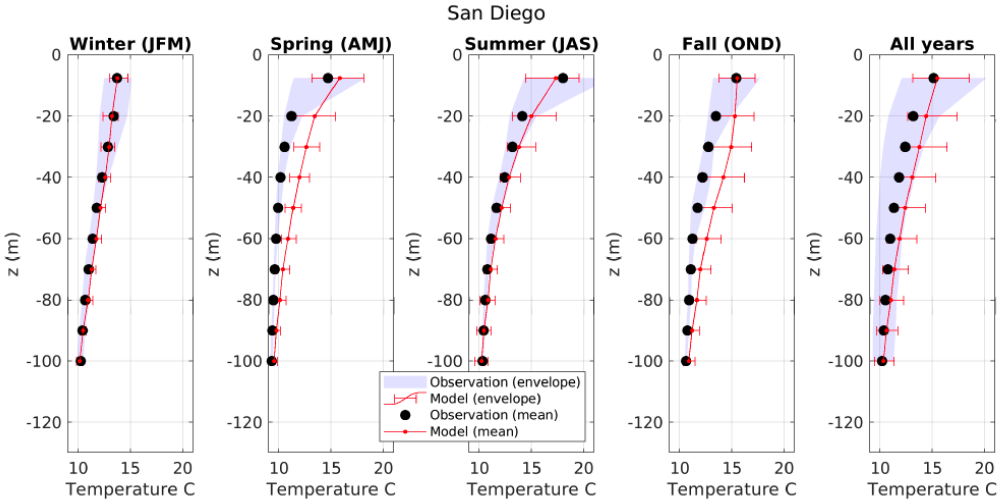

Figure S5: Same as Fig S2 for San Diego using City of San Diego stations.

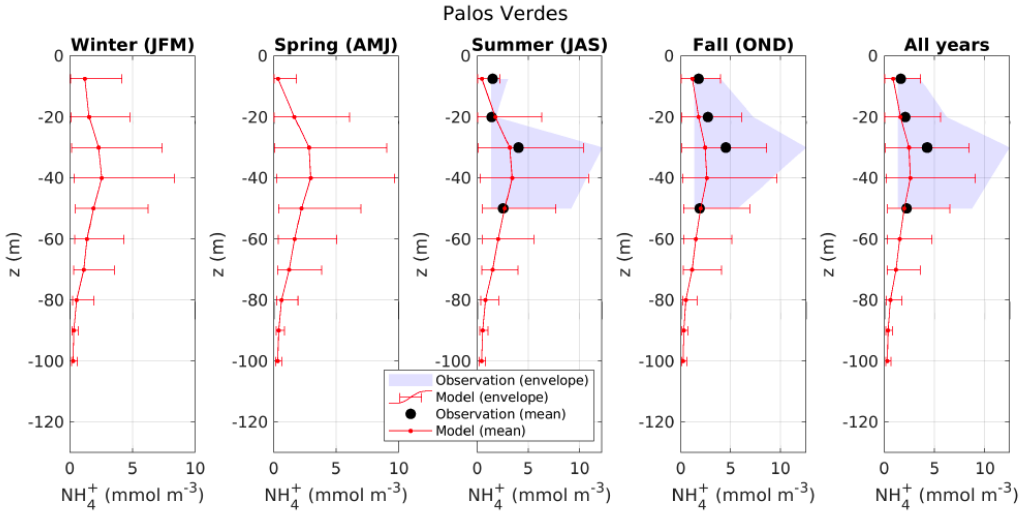

Figure S6: Seasonal profiles of average ammonium concentration off of Palos Verdes. The red line and red bars are the spatial and temporal means and the variability from the model. The black dots and the gray shade are the spatial and temporal mean and the variability from *in situ* data (LACSD stations). These profiles are showing agreement on intensity, seasonality and shape of the vertical profile with exceptionally high concentrations at mid-depth.

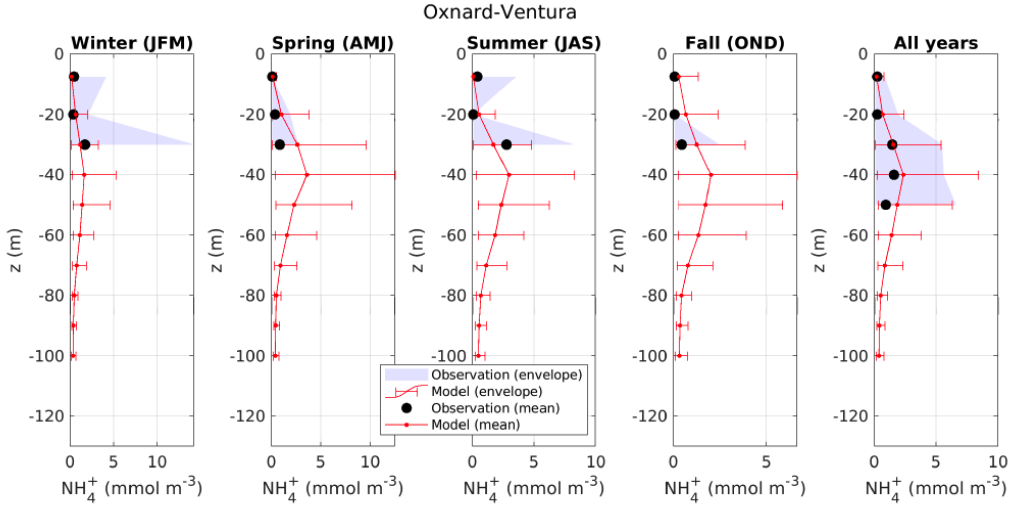

Figure S7: Same as Fig S6 for Oxnard/Ventura using City of Oxnard stations

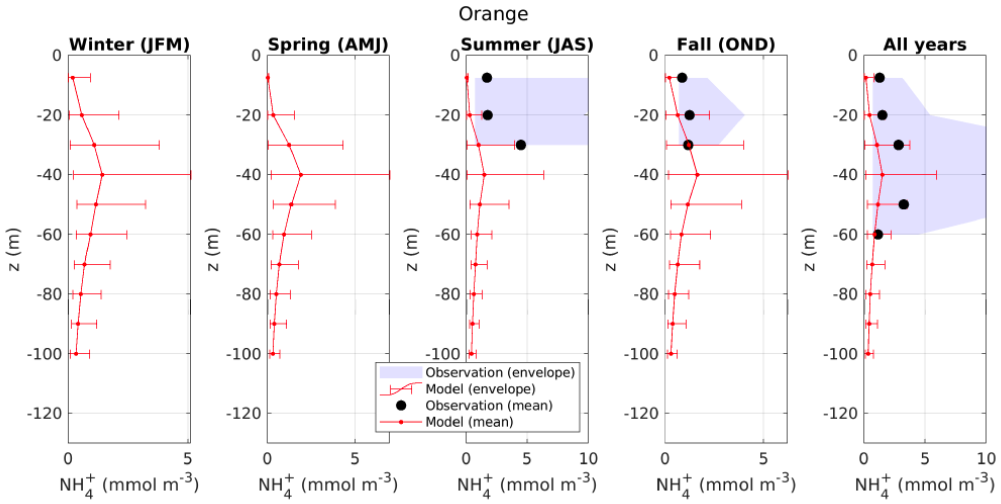

Figure S8: Same as Fig S6 for Orange County using OCSD stations.

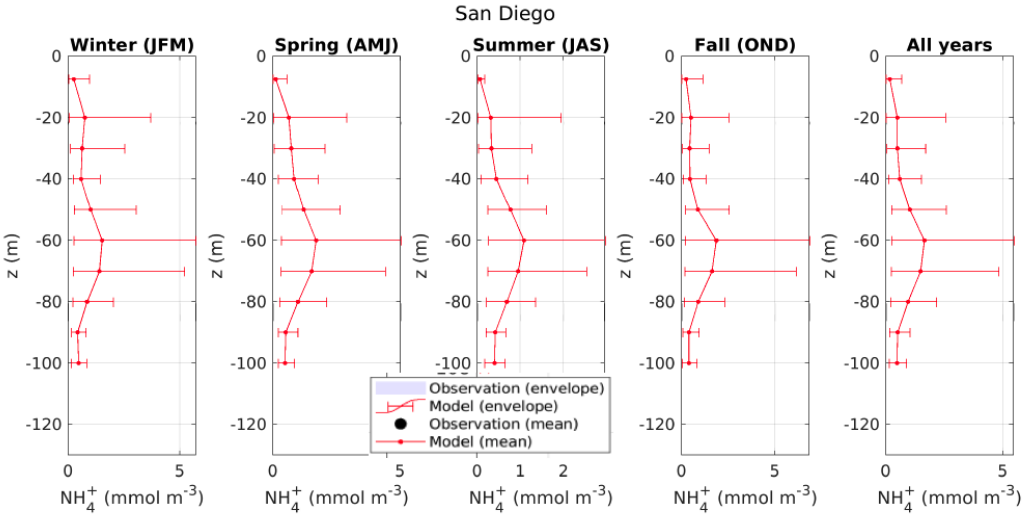

Figure S9: Same as Fig S6 for San Diego using City of San Diego stations. *In situ* data are missing but we wanted to report out the depth of maximum anthropogenic plume, in contrary to other subregion, in San Diego area, the plume rarely reaches 20 m.

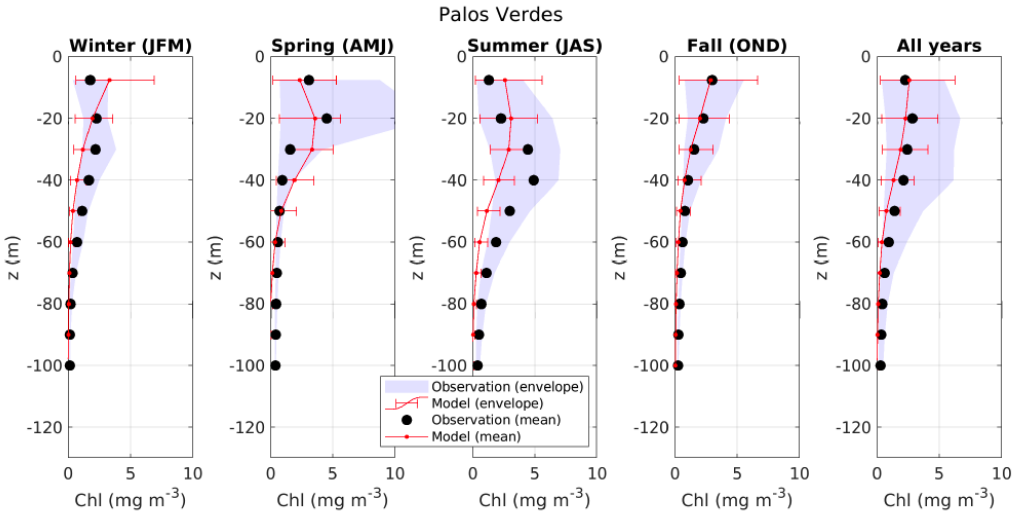

Figure S10: Seasonal profiles of average chlorophyll *a* concentration off of Palos Verdes. The red line and red bars are the spatial and temporal means and the variability from the model. The black dots and the gray shade are the spatial and temporal mean and the variability from *in situ* data (LACSD stations). These profiles are showing agreement on intensity, seasonality and shape of the vertical profile with exceptionally high concentrations at mid-depth.

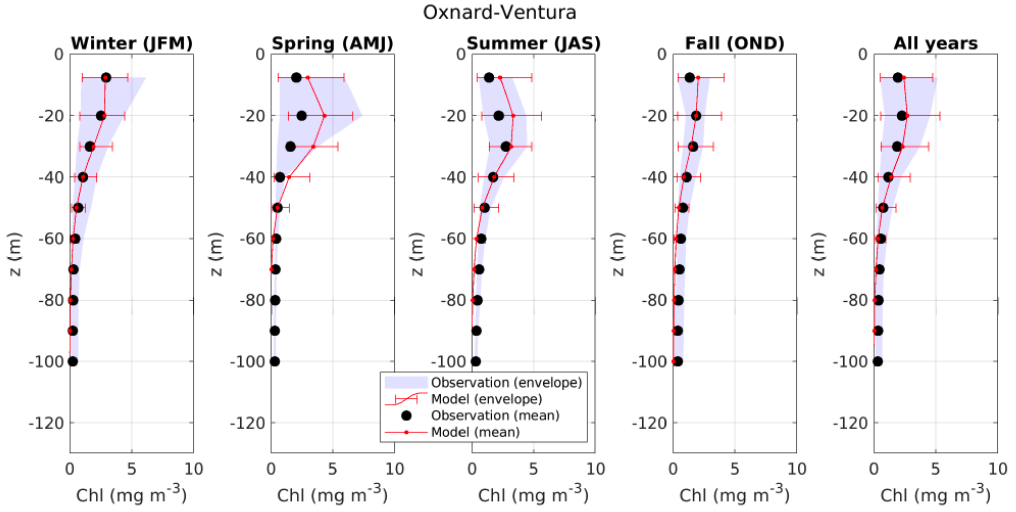

Figure S11: Same as Fig S10 for Oxnard/Ventura using City of Oxnard stations.

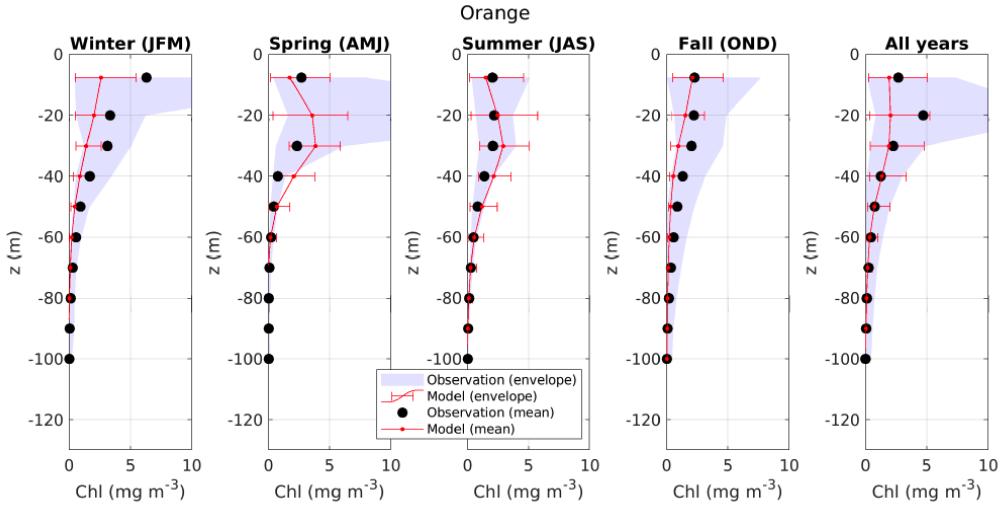

Figure S12: Same as Fig S10 for Orange County using OCSD stations.

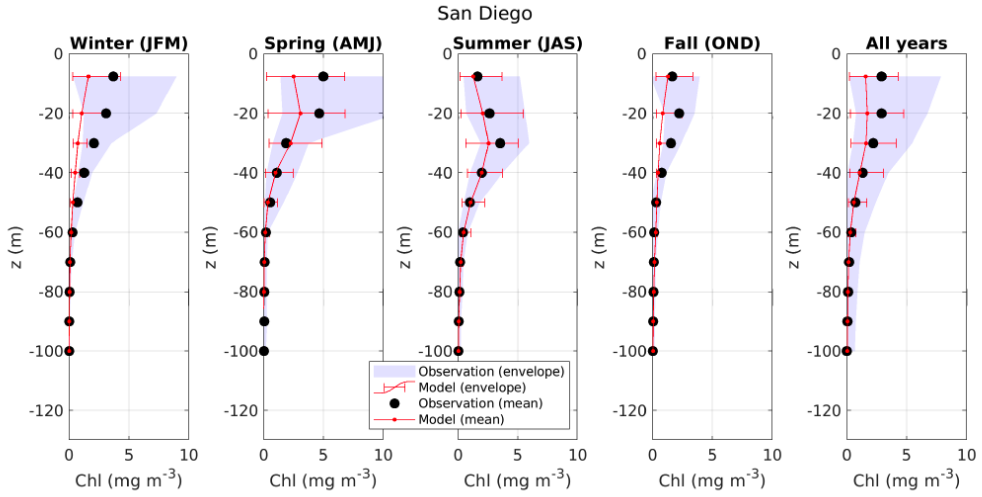

Figure S13: Same as Fig S10 for San Diego using City of San Diego stations.

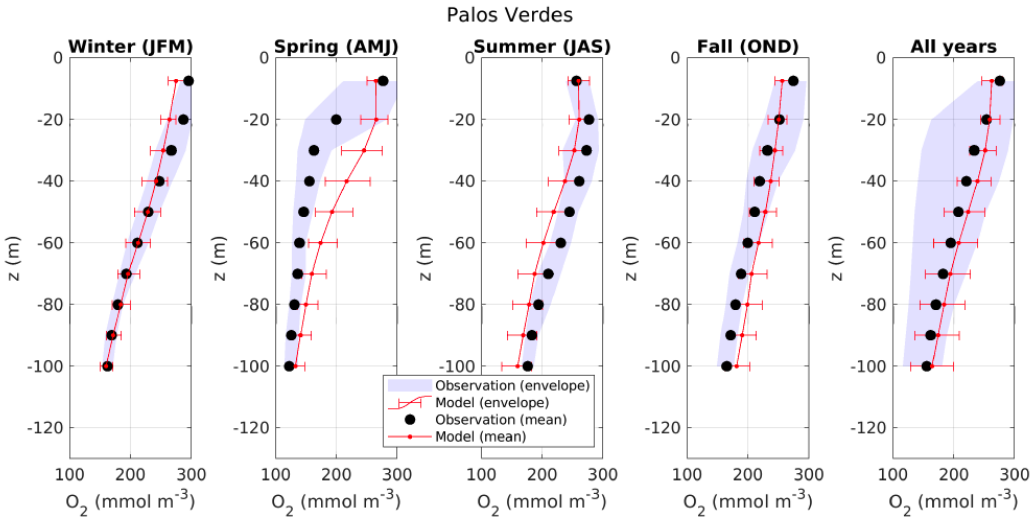

Figure S14: Seasonal profiles of average dissolved oxygen concentration off of Palos Verdes. The red line and red bars are the spatial and temporal means and the variability from the model. The black dots and the gray shade are the spatial and temporal mean and the variability from *in situ* data (LACSD stations). These profiles are showing agreement on intensity, seasonality and shape of the vertical profile with exceptionally high concentrations at mid-depth.

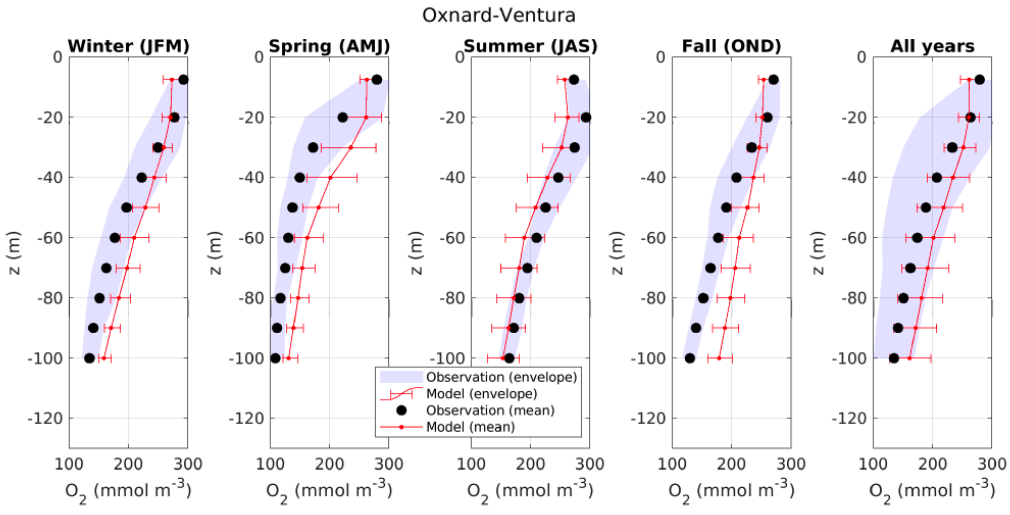

Figure S15: Same as Fig S14 for Oxnard/Ventura using City of Oxnard stations.

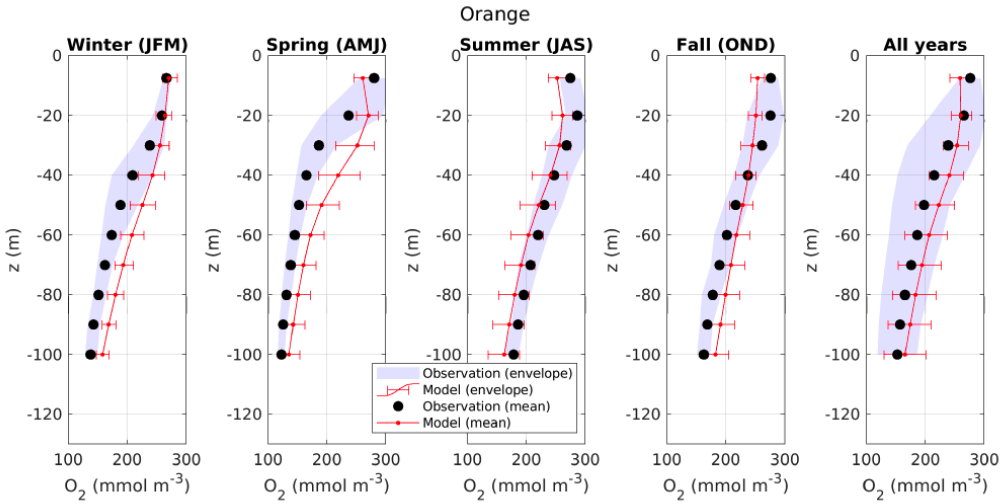

Figure S16: Same as Fig S14 for Orange County using OCSD stations.

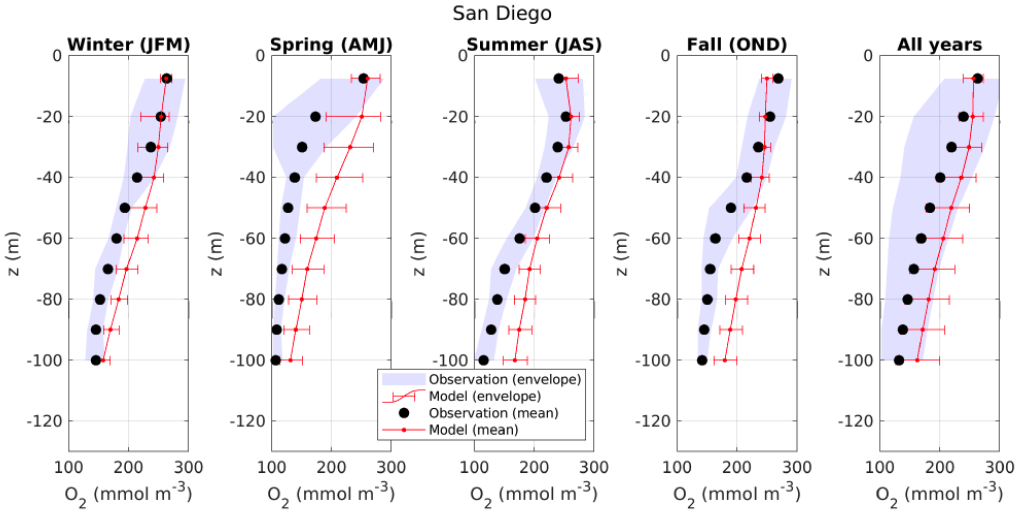

Figure S17: Same as Fig S14 for San Diego using City of San Diego stations.

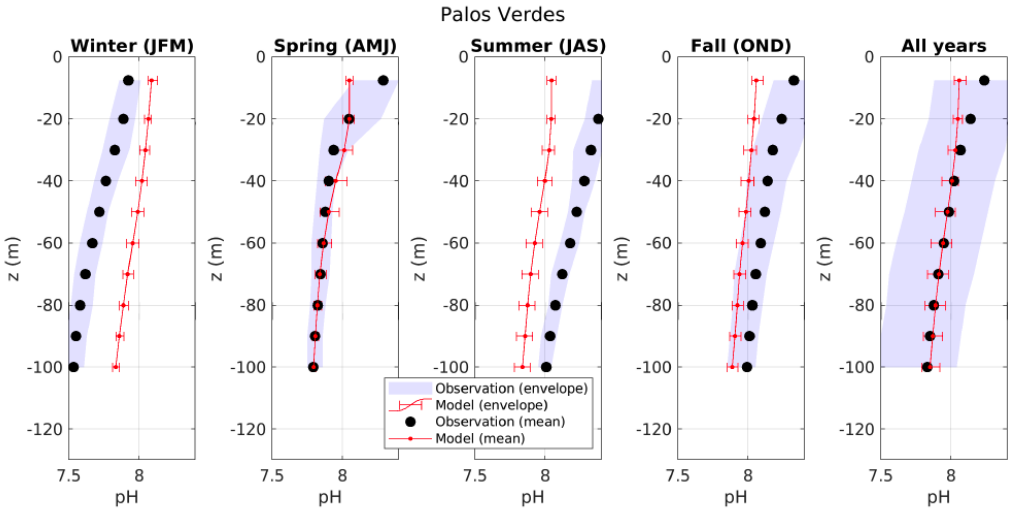

Figure S18: Seasonal profiles of average pH (seawater scale) off of Palos Verdes. The red line and red bars are the spatial and temporal means and the variability from the model. The black dots and the gray shade are the spatial and temporal mean and the variability from *in situ* data (LACSD stations). These profiles are showing agreement on intensity, seasonality and shape of the vertical profile with exceptionally high concentrations at mid-depth.

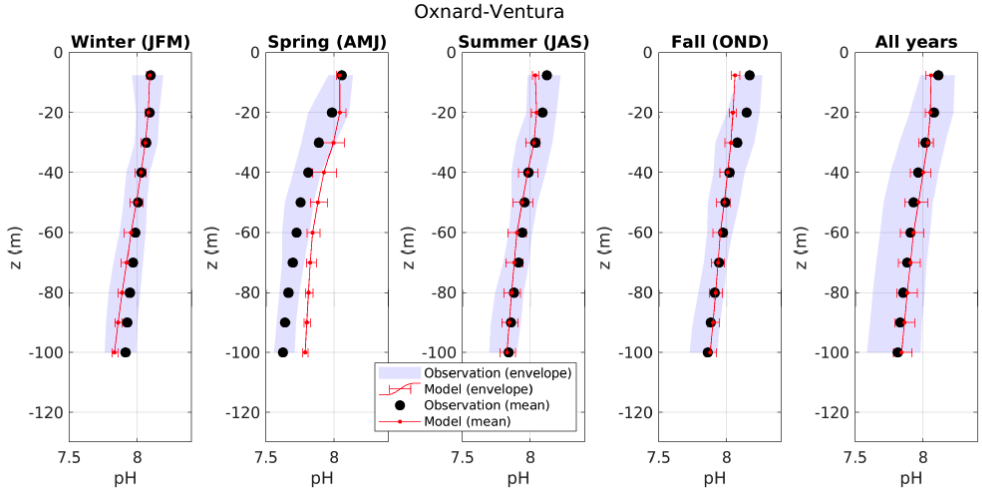

Figure S19: Same as Fig S18 for Oxnard/Ventura using City of Oxnard stations.

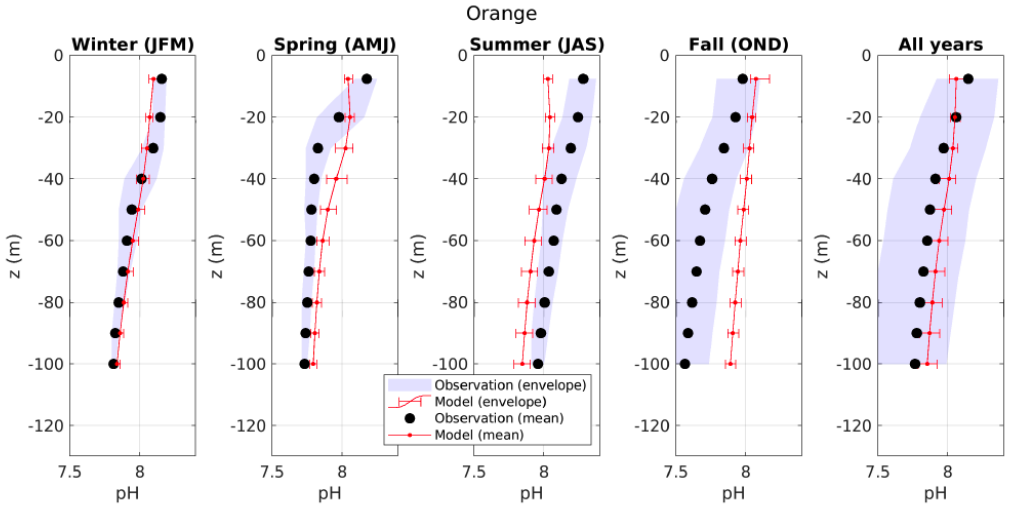

Figure S20: Same as Fig S18 for Orange County using OCSD stations.

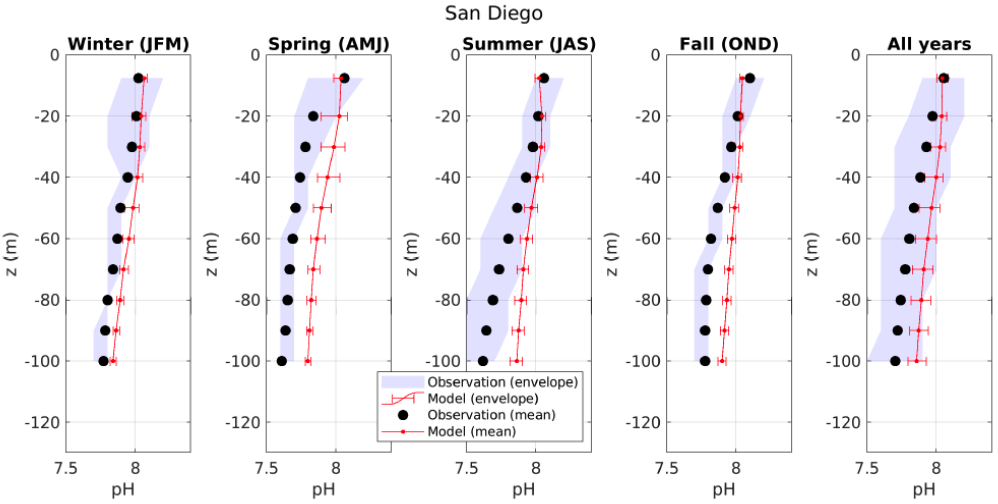

Figure S21: Same as Fig S18 for San Diego using City of San Diego stations.

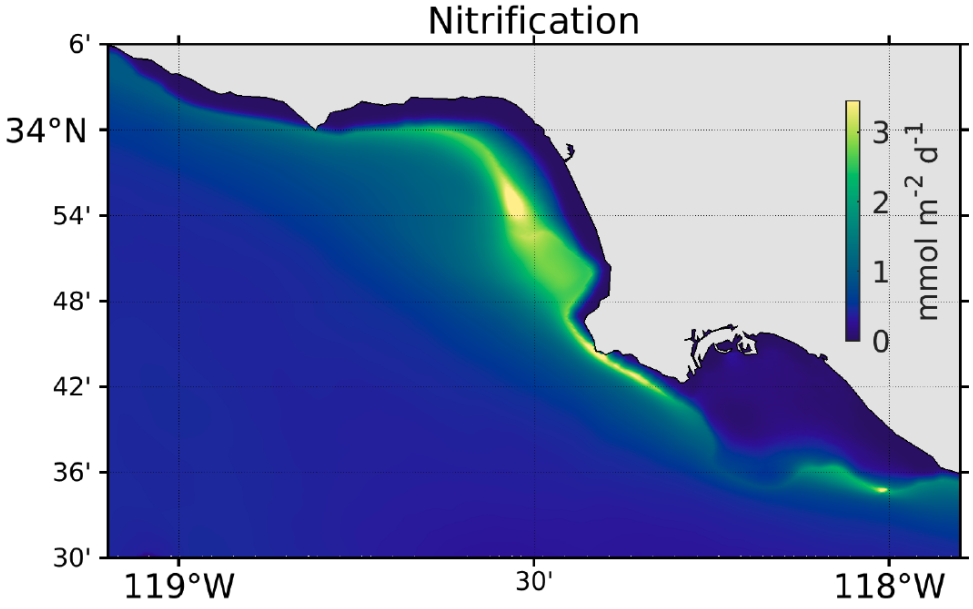

Figure S22: Average nitrification rate in Santa Monica and San Pedro bays. This figure shows the high rates around the locations of the outfalls that results from the release of high concentrations of ammonium below the thermocline.

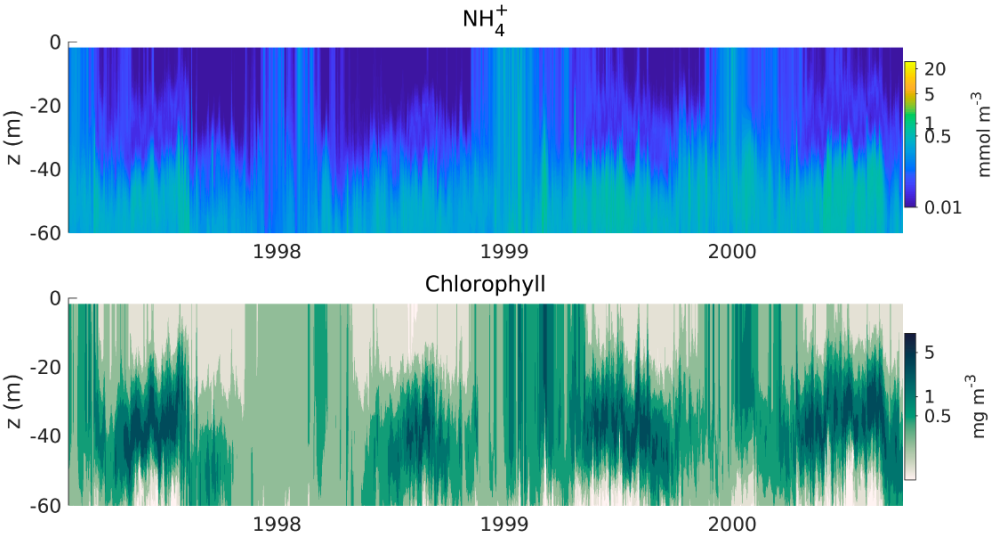

Figure S23: (upper panel) Hovmöller of ammonium concentration at San Pedro Oceanic Time-series (SPOT) located mid-distance between Los Angeles coast and Catalina Island. (lower panel) idem as (b) for chlorophyll *a* concentration. The Hovmöllers show 1) ammonium concentration off Los Angeles coast are not affected by anthropogenic loads. 2) Deep chlorophyll *a* maximum is trapped below at subsurface for 70% of the time and reach concentration of about 2 mmol Chl m^{-3}. Depth of the subsurface chlorophyll *a* maximum shows a seasonal cycle where it varies between 20 and 40m.

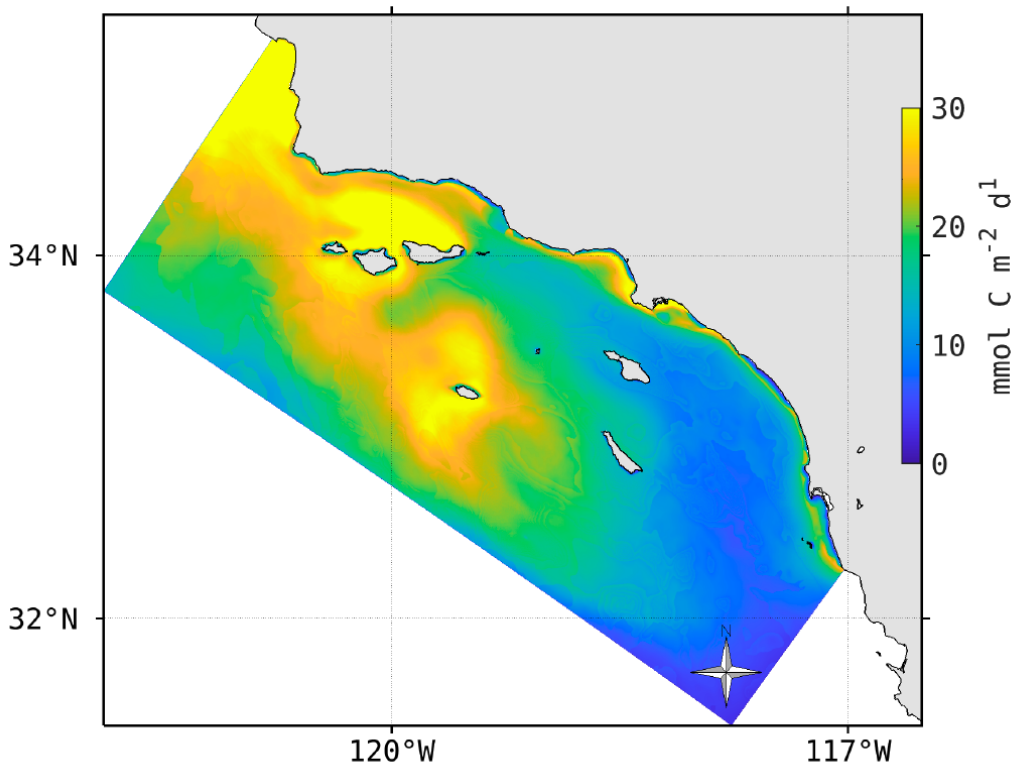

Figure S24: Summer time 1997-2000 average carbon export at 40 m in the SCB. The map shows hot-spots of intense carbon export in Santa Barbara and Los Angeles coasts.